



---

**Forschungszentrum Karlsruhe**  
in der Helmholtz-Gemeinschaft

---

**Wissenschaftliche Berichte**  
FZKA 7065

# **Creep of the Austenitic Steel AISI 316 L(N)**

## **Experiments and Models**

**M. Rieth, A. Falkenstein, P. Graf, S. Heger,  
U. Jäntsch, M. Klimiankou,  
E. Materna-Morris, H. Zimmermann**

**Institut für Materialforschung  
Programm Kernfusion**

**November 2004**

**Forschungszentrum Karlsruhe**

in der Helmholtz-Gemeinschaft

Wissenschaftliche Berichte

FZKA 7065

**Creep of the austenitic steel  
AISI 316 L(N)**

**– Experiments and Models –**

M. Rieth, A. Falkenstein, P. Graf, S. Heger, U. Jäntsch,  
M. Klimiankou, E. Materna-Morris, H. Zimmermann

Institut für Materialforschung

Programm Kernfusion

Forschungszentrum Karlsruhe GmbH, Karlsruhe

2004

**Impressum der Print-Ausgabe:**

**Als Manuskript gedruckt  
Für diesen Bericht behalten wir uns alle Rechte vor**

**Forschungszentrum Karlsruhe GmbH  
Postfach 3640, 76021 Karlsruhe**

**Mitglied der Hermann von Helmholtz-Gemeinschaft  
Deutscher Forschungszentren (HGF)**

**ISSN 0947-8620**

**urn:nbn:de:0005-070657**



## **ABSTRACT**

This report provides a general review on deformation mechanisms relevant for metallic materials. Different mechanisms are described by rate equations which are derived and discussed in detail. For the example of an austenitic 17Cr12Ni2Mo steel (AISI 316 L(N) or DIN 1.4909) these equations are applied to experimental creep data from own investigations at IMF-I (especially long-term creep tests with creep times of up to 10 years) and from NRIIM, Japan. Step-by-step a steady-state creep model is set up that is able to predict creep behaviour in a wide temperature and stress range. Due to the small number of adjustable parameters it may also be easily adapted to other materials. Since austenitic stainless steels are well known for their problematic aging behaviour at elevated temperatures, microstructure and precipitation formation as well as their impact on creep are outlined above all.

# **Kriechverhalten des austenitischen Stahls AISI 316 L(N)**

## **– Experimente und Modelle –**

### **ZUSAMMENFASSUNG**

Der vorliegende Bericht beinhaltet eine allgemeine Übersicht über Verformungsmechanismen, die bei metallischen Werkstoffen auftreten können. Dabei werden Gleichungen für die unterschiedlichen Mechanismen hergeleitet und ausführlich diskutiert. Am Beispiel eines austenitischen 17Cr12Ni2Mo-Stahls (AISI 316 L(N) oder DIN 1.4909) findet dann die Anwendung dieser Gleichungen auf experimentelle Kriechdaten aus eigenen Untersuchungen im IMF-I (insbesondere Langzeitkriechuntersuchungen mit Versuchszeiten von bis zu 10 Jahren) und von NRIM, Japan statt. Dadurch wird schrittweise ein Modell für das stationäre Kriechen aufgestellt, das das Kriechverhalten in einem weiten Temperatur- und Spannungsbereich vorhersagen kann. Auf Grund der wenigen anzupassenden Parameter kann es auch leicht auf andere Werkstoffe angewandt werden. Da austenitische rostfreie Edelstähle für ihr problematisches Alterungsverhalten bei höheren Temperaturen bekannt sind, wird vor allem auch die Mikrostruktur, die Bildung von Ausscheidungen und deren Einfluss auf das Kriechen dargestellt.

---

# CONTENTS

<b>1</b>	<b>Introduction</b> .....	<b>1</b>
<b>2</b>	<b>Experimental</b> .....	<b>2</b>
2.1	Material .....	2
2.2	Equipment, Specimens, Test Procedure, and Evaluation .....	3
2.3	Creep Test Results .....	4
2.4	Microstructure .....	6
<b>3</b>	<b>Deformation Mechanisms</b> .....	<b>13</b>
3.1	Overview .....	13
3.2	Diffusional Flow (Diffusion Creep).....	17
3.2.1	Nabarro-Herring Creep .....	17
3.2.2	Coble Creep.....	19
3.2.3	Alternative Descriptions .....	19
3.3	Power-law Creep (Dislocation Creep).....	21
3.3.1	Power-law Creep by Climb (plus Glide).....	21
3.3.2	Power-law Breakdown .....	26
3.4	Mechanical Twinning .....	27
3.5	Dislocation Glide (Low Temperature Plasticity).....	28
3.5.1	Plasticity Limited by Discrete Obstacles .....	29
3.5.2	Plasticity Limited by Lattice Friction.....	31
3.6	Elastic Collapse .....	32
3.7	Summary.....	33
<b>4</b>	<b>Steady-State Creep Model</b> .....	<b>35</b>
4.1	Diffusion Creep .....	35
4.2	Plasticity (Dislocation Glide).....	36
4.3	Power Law Creep (Dislocation Climb).....	37
4.4	Transition from Creep by Climb to Creep by Glide.....	38
4.5	Assessment and Discussion of the Stationary Creep Model.....	39

---

<b>5</b>	<b>Conclusion .....</b>	<b>43</b>
<b>6</b>	<b>Literature .....</b>	<b>46</b>
<b>7</b>	<b>Appendix/Tables .....</b>	<b>48</b>
7.1	Constants and Parameters .....	48
7.2	Experimental Data .....	50
7.3	Metallographic Examinations .....	57
7.3.1	Test No. ZSV1921: 750 °C, 2650 h .....	57
7.3.2	Test No. ZSV1913: 750 °C, 15692 h .....	61
7.3.3	AISI 316 L(N) KSW heat (similar to present CRM heat): 750 °C, 1404 h .....	66
7.3.4	AISI 316 L(N) KSW heat (similar to present CRM heat): 750 °C, 13824 h .....	72

# 1 Introduction

Among many other applications the austenitic 17/12/2–CrNiMo steel 316 L(N) (DIN 1.4909) is used or envisaged for both conventional and nuclear power plant construction as well as in the International Nuclear Fusion Project. Worldwide a huge number of experimental investigations have already been carried out to determine the material properties (including creep behavior) of this steel type in the conventional stress and temperature range. Our previous creep studies, for example, focused on three batches in the temperature range of 500-750 °C for periods of up to 85000 h [1-6].

In the design relevant low-stress range at 550 °C and 600 °C, however, creep data allowing statements to be made about the stress dependence of the minimum creep rate or about the technically relevant creep strain limits are almost unavailable. This is not only due to reasons of time, but to technical reasons, too. In this stress-temperature range, the expected creep or strain rates are so small that they can hardly be measured by conventional creep tests. Therefore, a special long-term creep testing program at 550 °C and 600 °C, respectively, was started in 1991 [7]. After an experimental period of about 10 years the creep tests have been aborted and evaluated.

Now, this low-stress creep data not only allow for a much better long-term prediction of the reliability of 316 L(N) applications but also enable deformation modeling for a broader stress range.

The present report focuses mainly on the set-up of a steady-state creep model for the 316 L(N) steel. Therefore, after an overview of experimental procedures and material properties, a short review on deformation mechanisms and their description by rate equations is given. In the final section these equations are applied to the experimental creep data and the resulting model is critically discussed in detail.

## 2 Experimental

### 2.1 Material

A part of the AISI 316 steel family – also known as V4A-Series or as trademark NIROSTA – is shown in Fig.1.

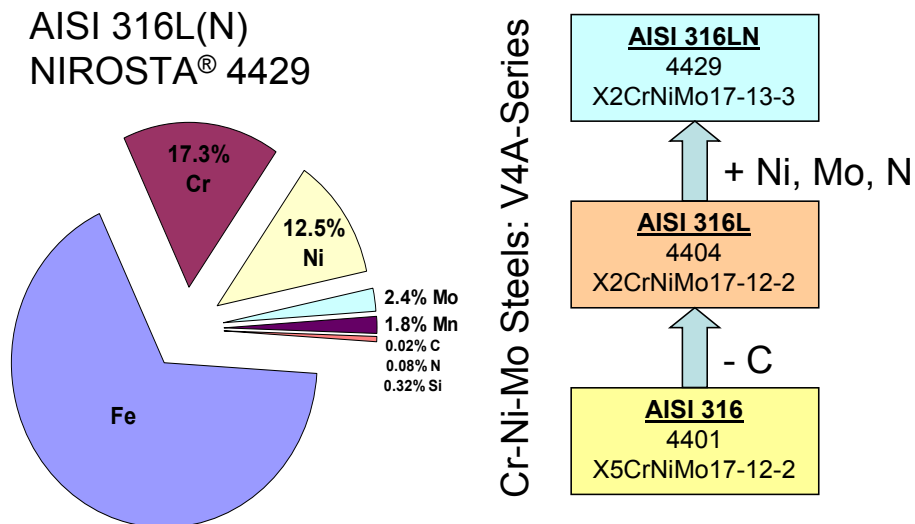


Fig. 1: The AISI 316 austenitic steel family.

Most data used in the current report result from experiments performed with the heat no. 11477 from Creusot-Marell (CRM). This heat had been delivered as 40 mm hot rolled plate with a final heat treatment at 1100 °C followed by water quenching. Quality insurance reported this batch as nearly free of  $\delta$ -ferrite (< 1 %).

In addition to that, some single data points have been taken from NRIM data sheets [6, 8-11] for comparable alloys (for chemical composition see Table 1). These had been produced as 50 mm, as 60 mm bars, as tubes (wall thickness 8.8 mm) and as 24 mm plates. Their final heat treatment was 1050°C, 1080 °C, 1130 °C, and 1100 °C, also water quenched.

Table 1: Chemical composition of different AISI 316 L(N) steels in wt. per cent.

Alloy	C	Si	Mn	P	S	Cr	Ni	Mo	Cu	N	Al	B
CRM 11477	0.02	0.32	1.80	0.02	0.006	17.34	12.50	2.40	0.12	0.08	0.018	0.0014
SUS 316-B ADA	0.06	0.46	1.49	0.03	0.026	17.43	12.48	2.49	0.15	0.019	0.025	0.0008
SUS 316-H TB AAL	0.07	0.61	1.65	0.03	0.007	16.60	13.6	2.33	0.26	0.025	0.017	0.0011

## 2.2 Equipment, Specimens, Test Procedure, and Evaluation

All creep specimens were produced out of the centre of the 40 mm plate (CRM 11477) transverse to rolling direction. For the specimens screw heads of 5 mm and 8 mm in diameter with 30 mm, and 200 mm gauge length were selected. The increased length of 200 mm ensures that the measurement of the creep behaviour is much more accurate than for standard specimens ( $\varnothing 8 \times 50$  mm, see Fig. 2). The test temperature was controlled by means of three PtRh-Pt thermocouples and kept constant at  $\pm 2$  K by means of three PID control units. For creep measurement, the specimens were equipped with a double-coil extensometer and the creep behaviour was registered continuously. The resolution was about 0.001 mm (1:1250). Loading took place in normal atmosphere (air) via lever arms (1:15) using weights. A picture of the creep facilities is given in Fig. 2.

Creep Test Facilities



Creep Specimens



### Low Stress Regime

creep rates of  $10^{-9}$  to  $10^{-7}$ /h, that is:

gauge length 30 mm  $\rightarrow$  0.3-30  $\mu$ m/year  
gauge length 200 mm  $\rightarrow$  2-200  $\mu$ m/year

Fig. 2: Creep test facilities and specimens. To improve resolution and sensitivity of creep tests, an increased specimen length has been used for long-term tests.

The continuously registered strain curves have been digitalized (see Fig. 3, blue dots). Then the creep rate has been obtained by numerical differentiation (Fig.3, red dots).

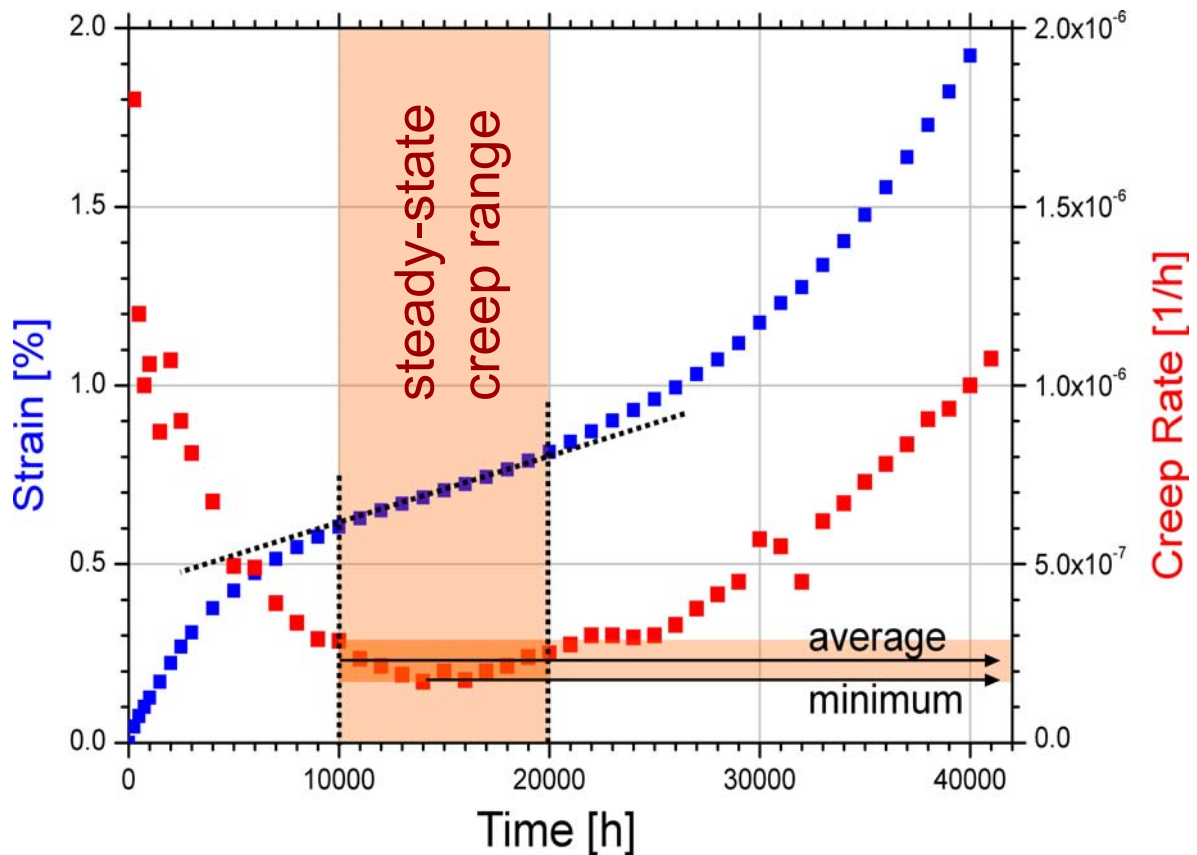


Fig. 3: Determination of characteristic creep data from the registered strain curve.

Due to fluctuations it is sometimes rather difficult to determine the range of steady-state creep. However, in all cases we defined the steady-state creep rate as minimum value while onset and end of the steady-state creep range has been defined by a scatter band of  $\pm 20\%$  of the minimum value.

### 2.3 Creep Test Results

A number of different tests have been performed with standard specimens ( $\varnothing 5 \times 30$  mm) in the usual stress range at temperatures between 550 and 750 °C. To examine long-term creep seven experiments were performed at 550°C in the stress range of 100-250 MPa and another six tests were run at 600°C in the range of 60-170 MPa. Of course, a certain scattering occurs at creep rates of  $\dot{\epsilon} \leq 10^{-7} \text{ h}^{-1}$  which corresponds to a strain rate of  $\leq 0.1 \text{ mm} / 5000 \text{ h}$  even for a gauge length of  $L_0 = 200 \text{ mm}$ . This scattering may be due either to measurement technology or to the material used.

However, the minimum creep rate was reached for the higher stresses. For lower stresses, sometimes the value could only be estimated. The results for the steady-state creep rates are shown in Fig. 4.

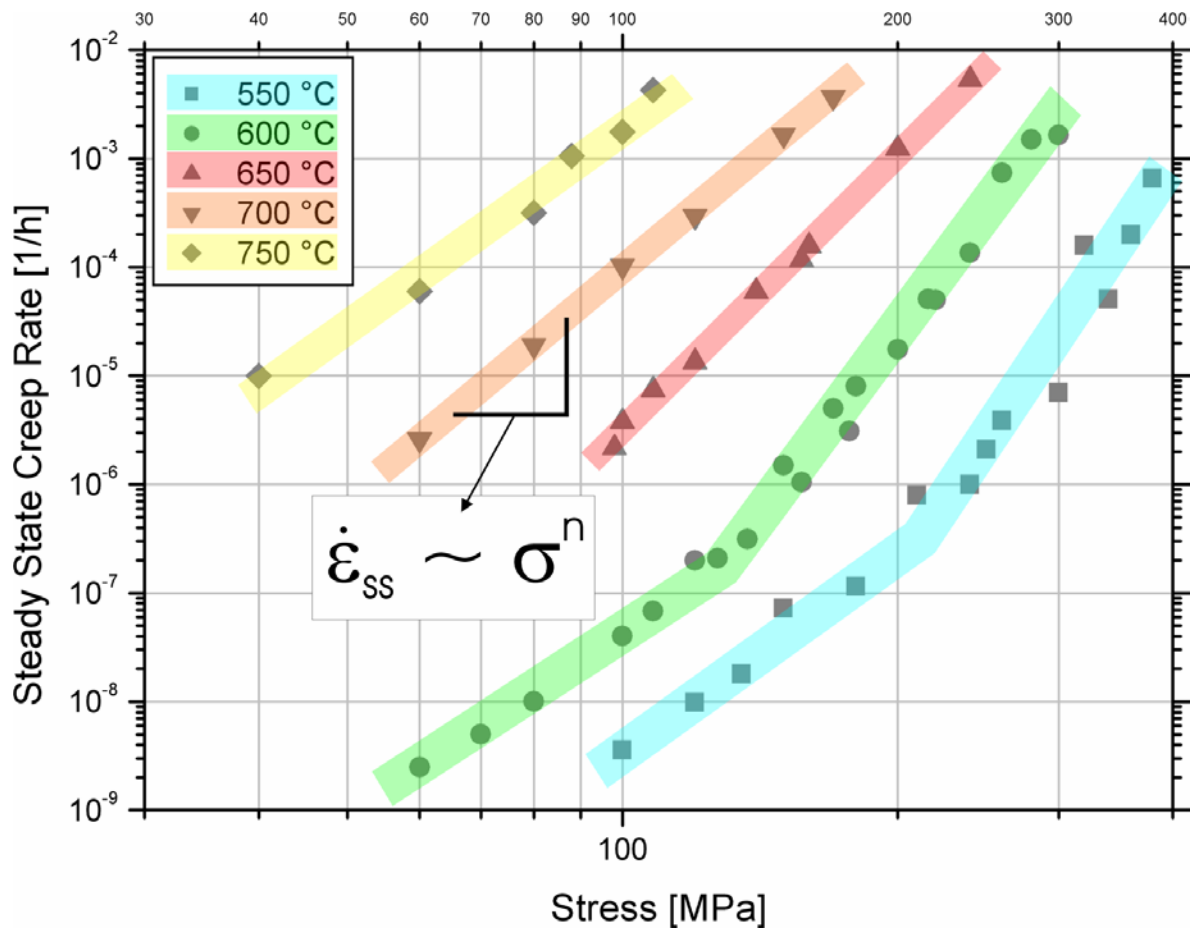


Fig. 4: Steady-state creep rates depending on stress for different temperatures interpreted in terms of power-law creep.

It can be noticed that the dependence of the steady state creep rate at 550 and 600 °C on the stress is changed considerably in the low-stress range as compared to the high-stress ranges. This means that the creep rates are much higher than the values that would have been extrapolated from the usual stress range.

At first glance, a plausible explanation could be the fact that all experiments performed at 550 °C and 600 °C with  $\sigma > 210$  MPa are found to be in stress ranges with initial plastic strains of more than 5 % at the start of the experiments, which are due to the low yield stress at these temperatures. This means that the creep behavior at stresses of less than 210 MPa actually refers to the specified solution-treated state, whereas the material is found to be in the solution-treated deformed state at stresses of more than 210 MPa (up to 25 % at 380 MPa).

It was already demonstrated by several experiments with the Mo-free steel X6CrNi 1811 (corresponding to AISI 304) that this plastic deformation at the start of the tests acts like a preceding cold deformation [12]. Cold deformation of specimens by 12 % prior to the test or deformation by 12 % at the test temperature resulted in creep and strength values which were similar to those obtained for solution-treated specimens with initial strains of more than 10% at the start of the experiments. Therefore, it might be assumed that the observed change of the steady-state creep rate at lower stresses could result from this experimentally build-in cold work. However, in Section 3 another explanation will be favored.

## 2.4 Microstructure

Quite another but also reasonable description could be the change of the microstructure with time since austenitic stainless steels are well known for their thermal instability at higher temperatures.

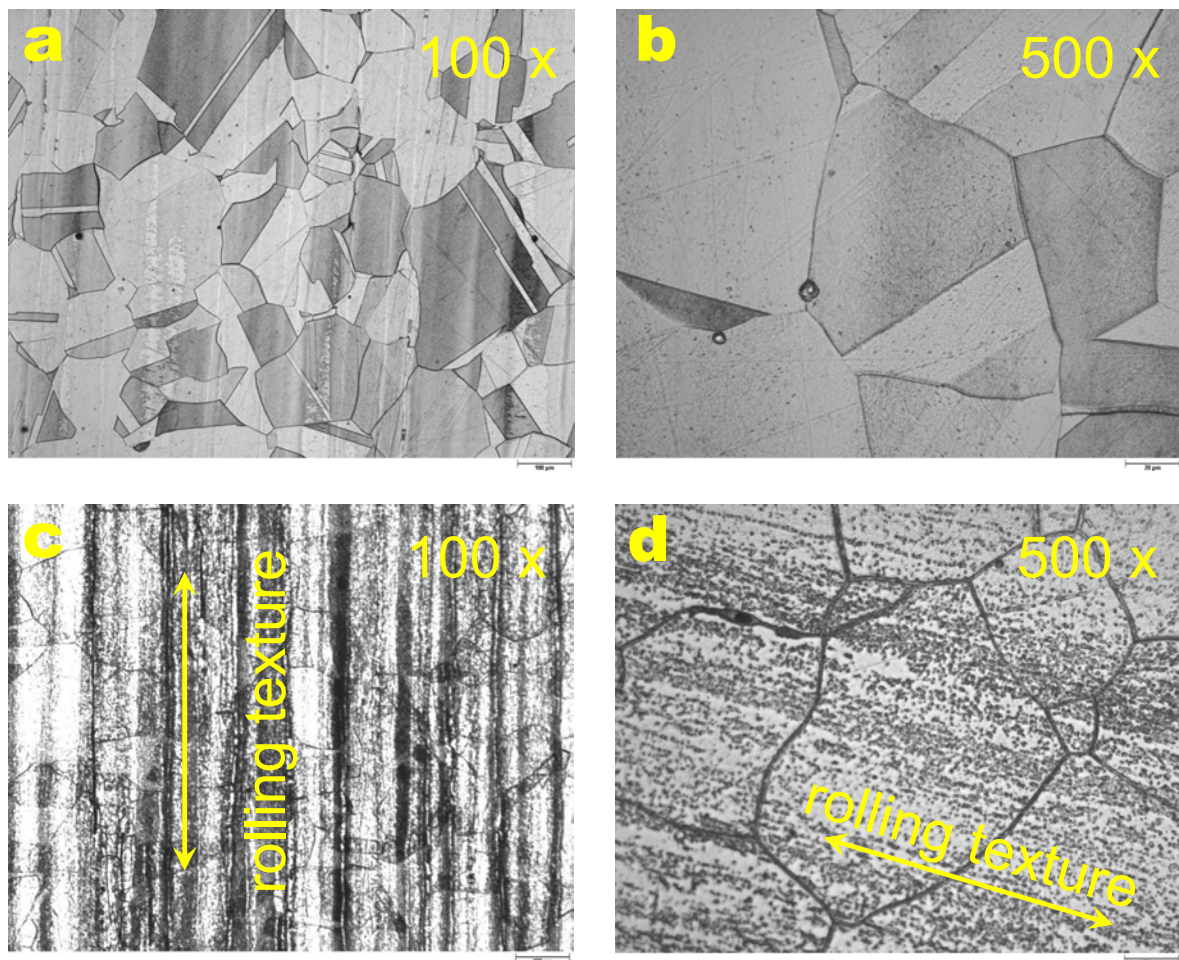


Fig. 5: Microstructure of the material as delivered (a, b). This is the usual structure of austenitic stainless steel with some twins and a slight texture along the rolling direction. The microstructure changes considerably after aging of 85000 h at 600 °C (c, d).

Figure 5 a, b shows the microstructure of the 316 L(N) steel in the condition as delivered. In general there is nothing unusual. Typical twin formations are recognizable as well as a slight texture along the rolling direction combined with a few rather small inclusions. Other investigations have also shown small parts of delta ferrite.

After aging at 600 °C for 85000 h the microstructure has changed considerably (Fig. 5 c, d). Precipitations have formed mainly at grain boundaries and along the rolling texture.

A similar formation can be observed in SEM observations after 2650 h at 750 °C (Fig. 6).

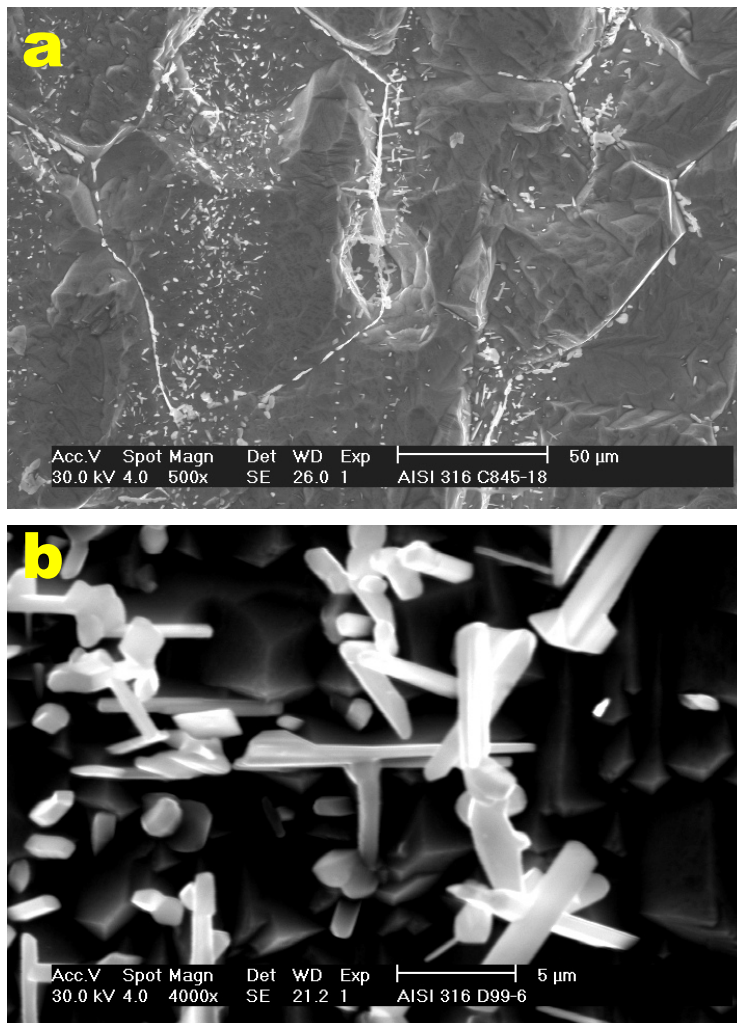


Fig. 6: a) SEM image of precipitations within and at grain boundaries after 2650 h at 750 °C. b) Magnification of inner grain precipitations after 15700 h at 750 °C.

Sequence and type of precipitations in AISI 316 austenitic stainless steels are well known and investigated (see, for example, [13, 14] and references therein, see also Sec. 7):

$M_{23}C_6$  carbides are the first phases that form during aging where M represents Cr, Fe, Mo, and Ni. Initially these carbides consist of a higher amount of Fe that usually is replaced by Cr and/or Mo during aging. A typical composition for AISI 316 steels is  $(Cr_{16}Fe_5Mo_2)C_6$ . For the present material the carbon content is 200 ppm at room temperature while at 600 °C the carbon solubility in equilibrium with the  $M_{23}C_6$  carbides is about 4 ppm. That is, at 600 °C almost all of the carbon

is removed from the matrix by precipitating as  $M_{23}C_6$  carbides. The most favorable precipitation sites are grain boundaries followed by twins and dislocations where cold deformation enhances precipitation within grains. The presence of nitrogen inhibits or delays formation of  $M_{23}C_6$  carbides. Therefore, at 600 °C with the present material  $M_{23}C_6$  precipitations at

grain boundaries start after only a few hundred hours and the formation of carbides within grains takes even 1000 hours and more.

Due to the small amount of carbon only a minor part of the precipitations shown in Figs. 5 and 6 can be explained by  $M_{23}C_6$  carbides. Besides carbide precipitation, during long-term aging (especially at higher temperatures) AISI 316 steels are prone to formation of intermetallic phases. Below 800 °C usually  $M_{23}C_6$  precipitation is followed by precipitation of Laves phase.

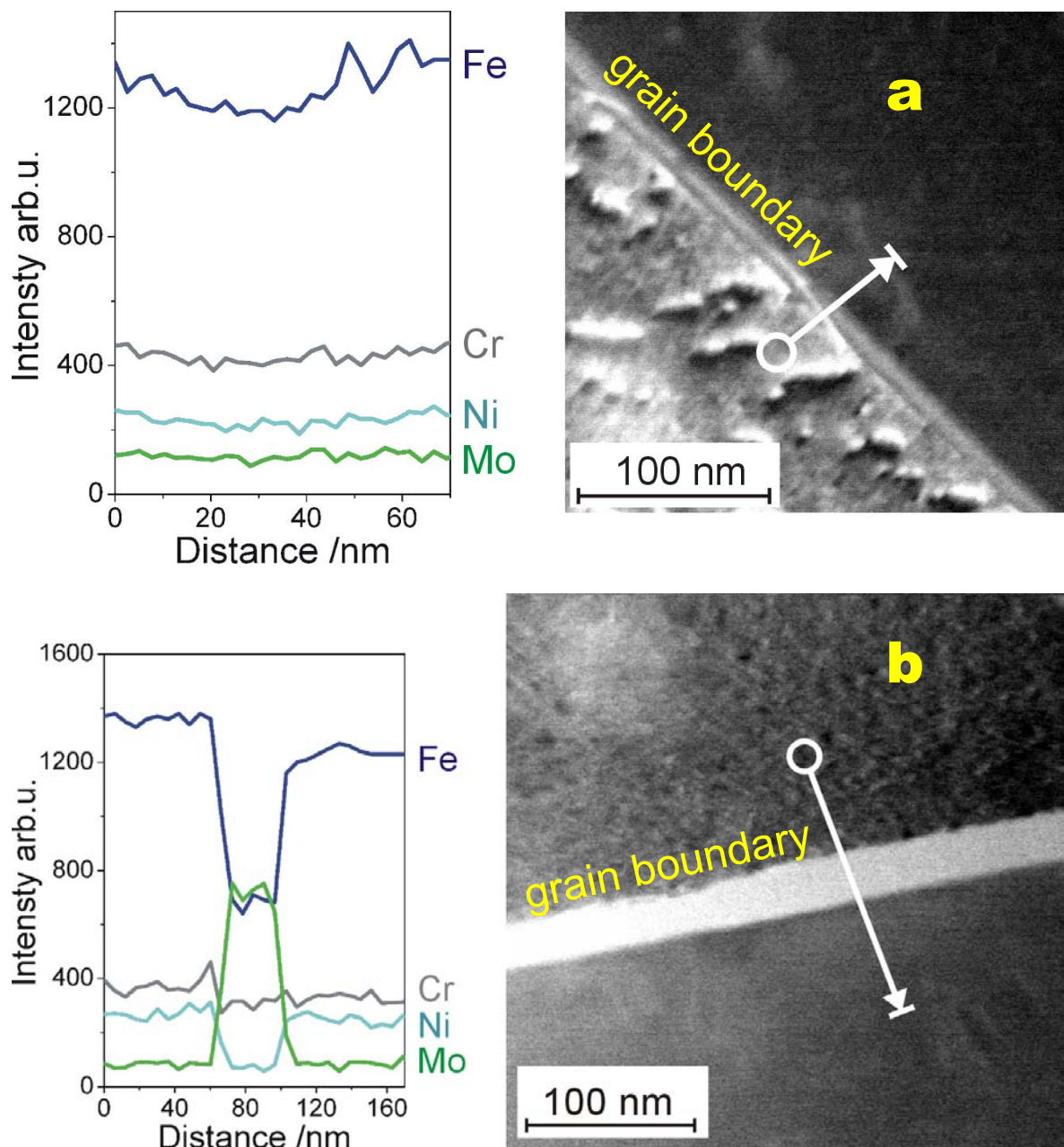
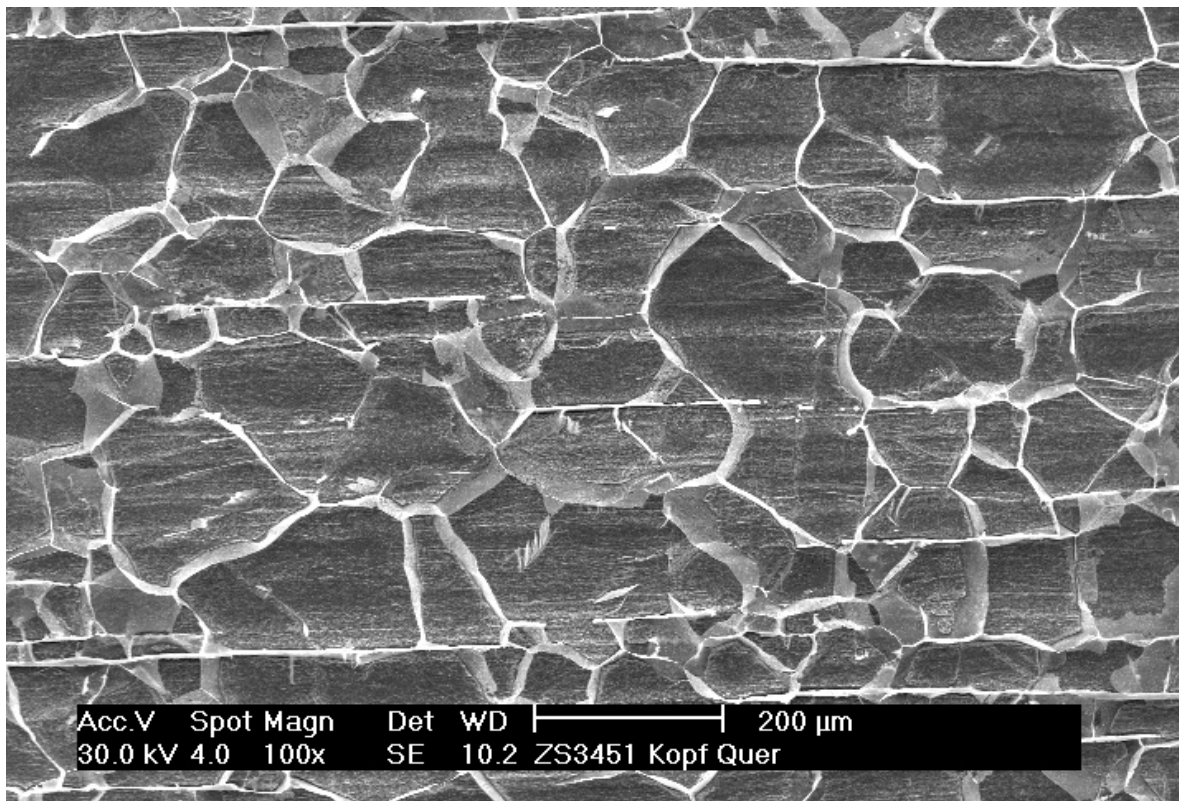


Fig. 7: TEM image of grain/twin boundaries before (a) and after aging at 600 °C for 85000 h (b). The results of the line scans on the left side show the relative change of Fe, Cr, Ni, and Mo concentration. The scanning paths are indicated in the TEM images.

In the case of the AISI 316 L(N) austenitic steel Laves phase consisting of  $\text{Fe}_2\text{Mo}$  starts to form after aging at 600 °C for about 10000 h first at grain boundaries and finally within grains. An example is given in Fig. 7 where the intensity drop of the Fe signal and the rise of the Mo signal lead to a Fe/Mo ratio of about 1:1 after analyzing the TEM signals.

The last phase to appear is the sigma phase. It has a very slow kinetics when forming from austenite and, therefore, takes aging of about 100000 h at 600 °C. But formation from ferrite is about 100 times faster. This is another reason why  $\delta$ -ferrite is undesirable in austenitic steels. However, the composition of sigma phase in AISI 316 L(N) steels can be approximated by  $(\text{Fe}, \text{Ni})_3(\text{Cr}, \text{Mo})_2$  or in wt%: 55Fe-29Cr-11Mo-5Ni. Sigma phase precipitates mainly on grain boundaries (especially on triple junctions) and on intragranular inclusions.



**Fig. 8:** SEM image of remaining grain boundaries (mainly sigma phase precipitation during aging at 600 °C for 85000 h) after etching.

Since sigma phase precipitations are enriched in Cr and Mo they are more resistant against acids and can be seen quite clearly after etching. An example is given in Fig. 8 where the former grain boundaries are still visible after surface etching due to the high amount of sigma phase formation. Even walls of sigma phase are sticking out of the surface for a few micrometers.

The large amount of sigma phase precipitation after 85000 hours at 600 °C finally leads to dendritic formations at and in some cases even within grains (Fig. 9). Further examples are given in Sect. 7.

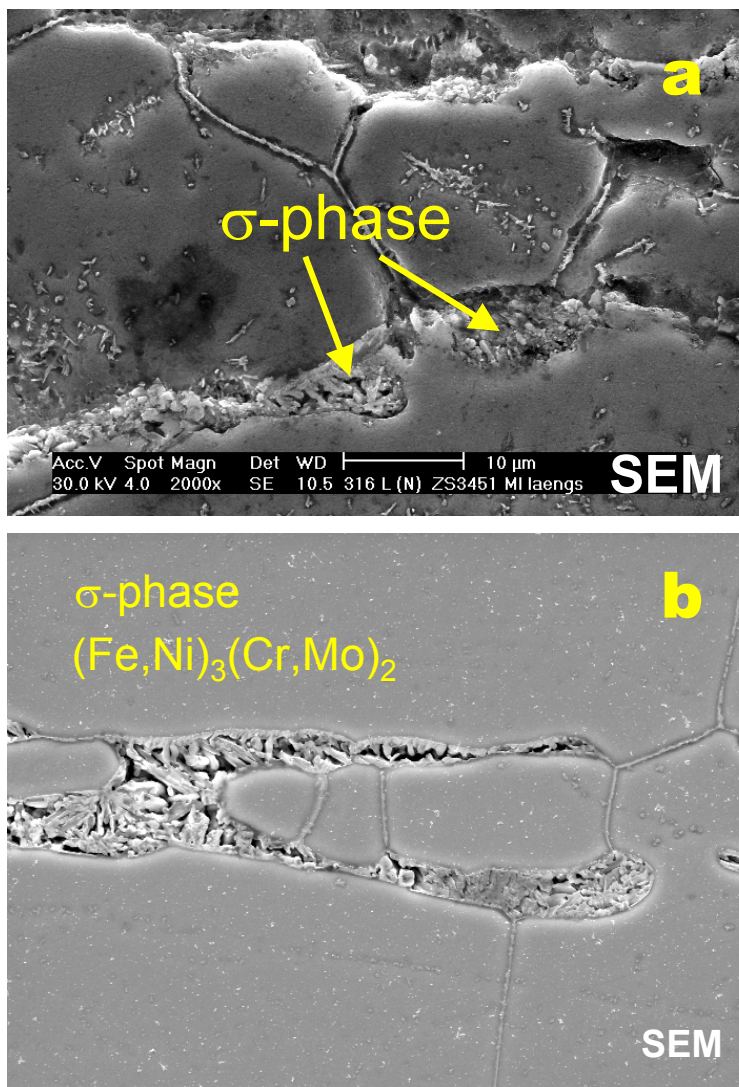


**Fig. 9:** Dendritic formations of sigma phase precipitations in AISI 316 L(N) austenitic stainless steel after aging at 600 °C for 85000 hours.

A consequence of the formation of intermetallic phases is the depletion of the adjacent matrix in chromium and molybdenum. This in turn increases the solubility of carbon in the matrix which leads to at least partial dissolution of the prior formed carbides. That is, after long-term aging carbides like  $M_{23}C_6$  are nearly vanished.

For an evaluation of the influence of the time-dependent microstructural composition on the creep behavior a precipitation diagram is necessary. At NIMS, Japan extensive aging experiments have been performed followed by TEM examinations to generate a time-temperature-precipitation diagram for a 18Cr-12Ni-Mo steel that is comparable to the AISI 316 L(N) [15].

In Fig. 10 this precipitation map is shown together with the results of the 316 L(N) sigma phase observations. As can be seen, the results for both materials are in good agreement.

Now the question is: Can the dependency change of the steady state creep rate on the stress in the low-stress range (see Fig. 4) be correlated with the aging (precipitation) behavior?

For this purpose the creep tests have been divided into low and high stress range. For the tests at 550 °C and 600 °C medium stress ranges (i.e., the range where the change in creep

behavior occurs) have been additionally considered. Then all particular times of the minimum creep rates have been determined and illustrated for each temperature as bars in the time-temperature-precipitation diagram (see Fig. 11).

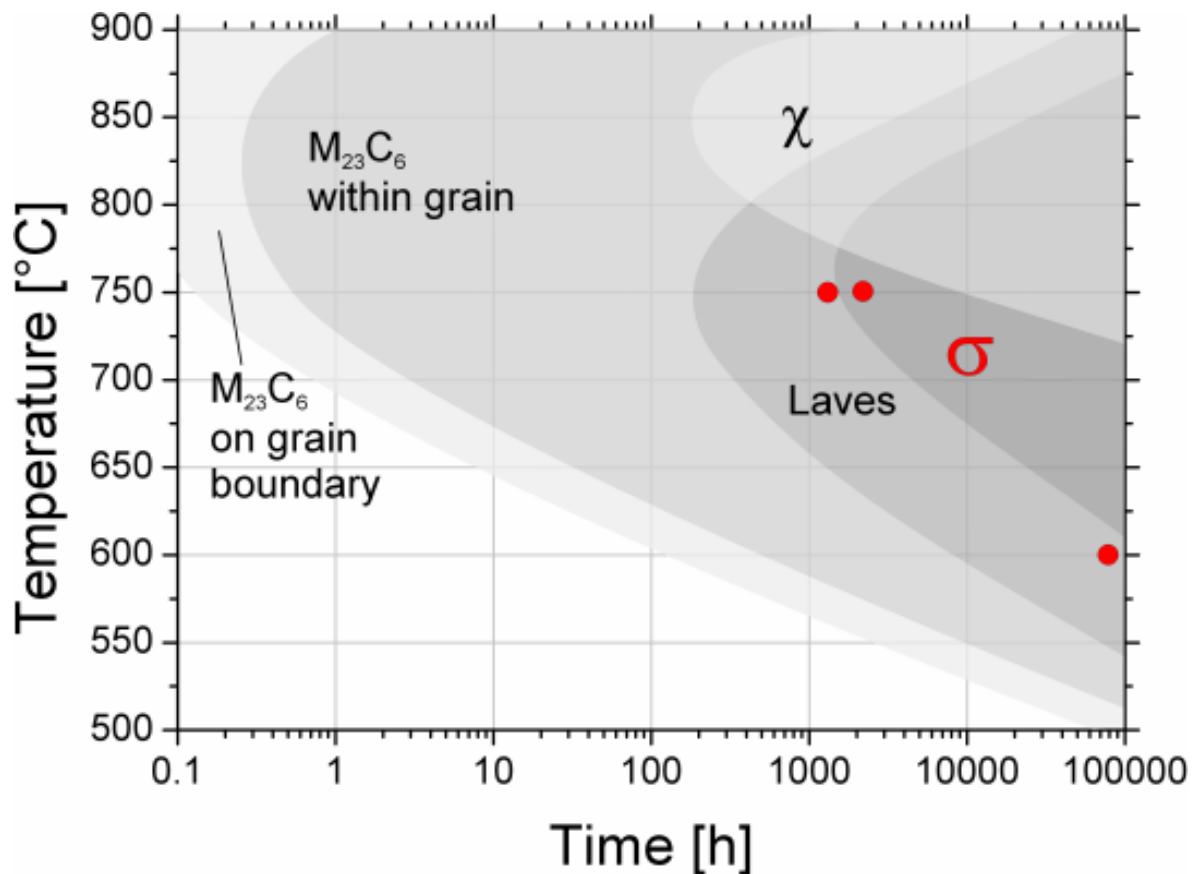


Fig. 10: Time-temperature-precipitation diagram by NIMS [15] for an austenitic stainless steel comparable to the AISI 316 L(N). The results of the AISI 316 L(N) sigma phase detection are shown as red dots to demonstrate the agreement.

At a glance, there is no correlation at all. Looking at the high stress range, for example, shows only that, depending on temperature, there are none, some or even more carbide precipitations. But these do not reflect in the creep behavior. In the most interesting medium stress range there are either carbides (at 550 °C) or Laves phase precipitations (at 600 °C). The same can be observed in the low stress range at 650-750 °C. That is, neither  $M_{23}C_6$  nor Laves phase precipitations can be the reason for a different creep rate behavior. As we have seen in Figs. 8 and 9, only the severe sigma phase formation could have had a significant influence on the creep properties. To check whether this is the case here, we have to correlate the steady-state periods with the times of sigma phase formation.

This has been illustrated in Fig. 11. From each curve in Fig.4 the two upper and the lower most experiment has been used to determine the periods of constant strain rate (steady-state). These periods are drawn over the time-temperature precipitation map as bars with lined and

squared ends (one has to keep in mind that the steady-state times are significantly lower than the overall creep rupture time or experimental times). Further, for the case of 550 °C and 600 °C the steady-state times have been determined from the experiment directly at and around the kink of the stress-creep rate curves (see Fig. 4). Those times have been plotted with circle ended line in Fig. 11. As can be clearly seen in, at times when sigma phase precipitation starts the creep tests are already far away from minimum creep rates – even in the lowest stress range.

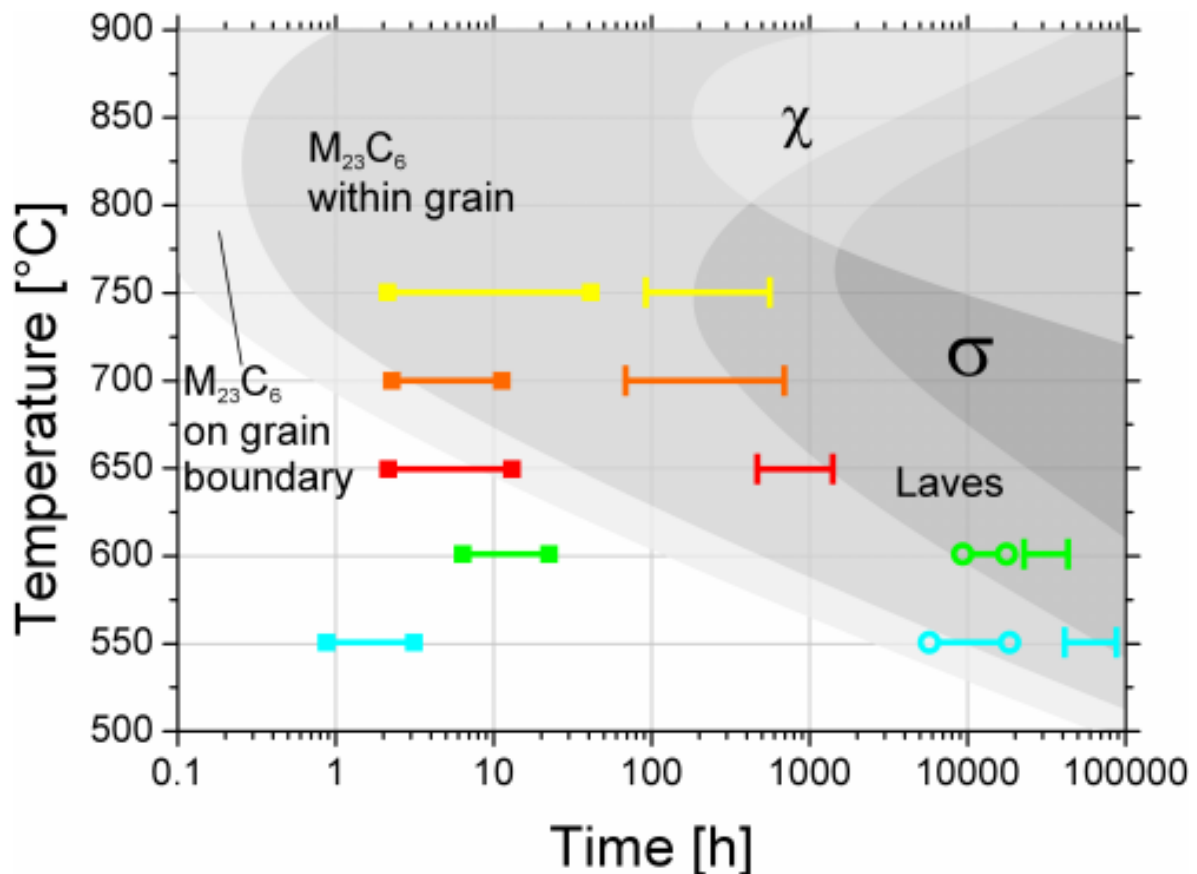


Fig. 11: A correlation attempt of the minimum creep rate times with precipitation areas. The observed minimum creep times are displayed as bars corresponding to the low (line ended), medium (circle ended), and high (square ended) stress range.

In summary, during steady-state creep of all tests (550-750 °C) in the medium and low stress range only carbides and Laves phase precipitate at the grain boundaries and within the grains. But only the creep tests at 550 °C and 600 °C show a change of the steady-state creep rate. Therefore, the change of microstructure with time can not be the reason for the observed creep behavior shown in Fig.4.

In fact, as will be demonstrated in the following sections, the steady-state creep rate depends strongly on the underlying deformation mechanisms which in turn depend on the applied stress.

## 3 Deformation Mechanisms

### 3.1 Overview

Crystalline solids deform plastically by a number of different and sometimes competing mechanisms. Although it is often convenient to describe a polycrystalline solid by a well defined yield strength, below which it doesn't flow and above which flow is rapid, this is only true at zero temperature. But plastic flow is a kinetic process and in general, the strength of solids depends on both strain and strain rate, as well as on temperature. It is determined by all the atomic processes that occur on the atomic scale like, for example, the glide motion of dislocation lines, the combined climb and glide of dislocations, the diffusive flow of individual atoms, the relative displacement of grains by grain boundary sliding including diffusion and defect motion in the boundaries, mechanical twinning by the motion of twinning dislocations, and so on [16].

But it is more convenient to describe the plasticity of polycrystalline solids in terms of the mechanisms to which the atomistic processes contribute. Often the deformation mechanisms are divided into five groups [16]:

- **Diffusional Flow (Diffusion Creep)** – based on either (a) lattice diffusion (*Nabarro-Herring* creep) or (b) grain boundary diffusion (*Coble* creep).
- **Power-law Creep (Dislocation Creep)** – diffusion controlled climb-plus-glide processes: (a) based on lattice diffusion controlled dislocation climb (high temperature creep), (b) based on core diffusion controlled dislocation climb (low temperature creep), (c) transition from climb-plus-glide to glide alone (power-law breakdown).
- **Mechanical Twinning** – low temperature plasticity by the motion of twinning dislocations.
- **Dislocation Glide** – low temperature plasticity based on dislocation glide, limited by (a) discrete obstacles or (b) by lattice resistance.
- **Elastic Collapse** – flow for stresses above the ideal shear strength.

Some mechanisms which are not important for the present material (e.g. *Harper-Dorn* creep or creep based on recrystallization) have been left out.

Plastic flow of fully dense solids is caused by the shear stress  $\sigma_s$  (deviatoric part of the stress field). In terms of the principal stresses  $\sigma_1$ ,  $\sigma_2$  and  $\sigma_3$  :

$$\sigma_s = \sqrt{\frac{1}{6} [(\sigma_1 - \sigma_2)^2 + (\sigma_2 - \sigma_3)^2 + (\sigma_3 - \sigma_1)^2]} . \quad (1)$$

It exerts forces on defects (dislocations, vacancies, etc.) in the solid and causes them to move. The defects are the carriers of deformation and, therefore, the shear strain rate  $\dot{\gamma}$  depends on density and velocity of these deformation carriers. In terms of the principal strain rates  $\dot{\epsilon}_1$ ,  $\dot{\epsilon}_2$  and  $\dot{\epsilon}_3$  it is given by:

$$\dot{\gamma} = \sqrt{\frac{3}{2} [(\dot{\epsilon}_1 - \dot{\epsilon}_2)^2 + (\dot{\epsilon}_2 - \dot{\epsilon}_3)^2 + (\dot{\epsilon}_3 - \dot{\epsilon}_1)^2]} \quad (2)$$

For simple tension,  $\sigma_s$  and  $\dot{\gamma}$  are related to the tensile stress  $\sigma_1$  and strain rate  $\dot{\epsilon}_1$  by:

$$\sigma_s = \frac{1}{\sqrt{3}} \sigma_1 \quad , \quad \dot{\gamma} = \sqrt{3} \dot{\epsilon}_1 . \quad (3)$$

Macroscopic variables of plastic deformation are stress  $\sigma_s$ , temperature  $T$ , strain rate  $\dot{\gamma}$ , strain  $\gamma$  and time  $t$ . During creep or creep rupture tests the stress and temperature are prescribed. Typically forms of strain and strain rate are shown in Fig. 12. At low temperatures of about  $0.1 T_M$  (melting point  $T_M$ ) the material undergoes work hardening until the flow strength equals the applied stress. During this process its structure changes: the dislocation density increases, therefore, further dislocation motion is blocked, the strain rate decreases to zero, and the strain tends asymptotically to a fixed value. During tensile tests the strain rate and temperature are prescribed. At low temperatures the stress rises as the dislocation density rises (Fig. 12). That is, for a given set of state variables  $S_i$  (dislocation density, dislocation arrangement, cell size, grain size, precipitate size, precipitate distribution, and so on) the strength is determined by  $\dot{\gamma}$  and  $T$ , or the strain rate is determined by  $\sigma_s$  and  $T$ .

At higher temperatures (about  $0.5 T_M$ ) polycrystalline materials creep (see Fig. 12). After a transient during which the state variables change, a steady state may be reached. During the steady state the solid continues to deform with no further (significant) change in  $S_i$ . Here the state variables  $S_i$  depend on stress, temperature, and strain rate and a relationship between these three macroscopic variables may be given.

At very high temperatures, or very low stresses, or very low strain rates the state variables may oscillate instead of tending to steady values. But often it is possible to define a quasi steady state anyway in which stress, temperature and strain rate are related.

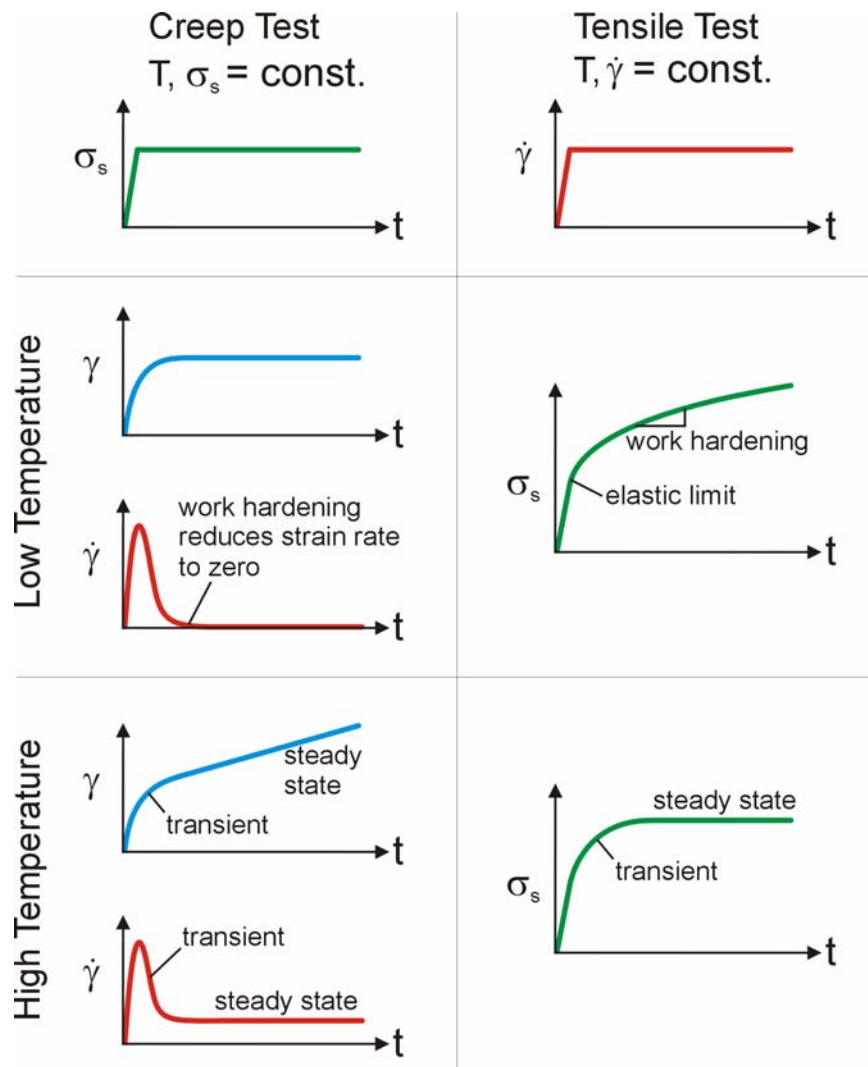


Fig. 12: Typical curves of strain, strain rate, and stress obtained by creep and tensile tests on metals or alloys at low and high temperatures.

As has been shown, either stress or strain rate can be used as independent variable. For the current work we will choose the strain rate  $\dot{\gamma}$  as independent variable since most experimental results are received from creep and creep rupture tests. In this case each deformation process can be described by a rate equation which relates  $\dot{\gamma}$  to the stress  $\sigma_s$ , temperature  $T$ , and to the structure of the material at that instant:

$$\dot{\gamma} = f(\sigma_s, T, S_i, P_j) . \quad (4)$$

As already mentioned, the set of  $i$  quantities  $S_i$  are the *state variables* which describe the current microstructural state of the solid. The set of  $j$  quantities  $P_j$  are *material properties* like lattice parameter, atomic volume, bond energies, moduli, diffusion constants, and so on. Most often these can be considered as constant.

But the state variables  $S_i$  generally change during the deformation processes (except in steady state). So a second set of equations is needed to describe their rate of change:

$$\frac{dS_i}{dt} = g_i(\sigma_s, T, S_i, P_j) . \quad (5)$$

The coupled set of equations (4) and (5) are the *constitutive law* for a deformation mechanism. They can be solved with respect to time to give the strain after any loading history. But while there are satisfactory models for the rate equation (4), there is still lack of understanding the structural evolution with strain or time. Therefore a sufficient description of the equation set (5) is not possible at present.

However, to proceed further, simplifying assumptions about the structure have to be made. Here are two possible alternatives. A very simple assumption is that of *constant structure*:

$$S_i = S_i^0 . \quad (6)$$

Then the rate equation for  $\dot{\gamma}$  completely describes plasticity. The second assumption is that of *steady state*:

$$\frac{dS_i}{dt} = 0 . \quad (7)$$

In this case the internal variables no longer appear explicitly in the rate equations. They are determined by the external variables of stress and temperature. Either simplification reduces the constitutive law to a single equation:

$$\dot{\gamma} = f(\sigma_s, T) , \quad (8)$$

since, for a given material the properties  $P_j$  are constant and the state variables are either constant or determined by  $\sigma_s$  and  $T$ .

In the following sections rate equations in the form of Eq. (8) are assembled for each of the deformation mechanisms (i.e., we consider only steady state creep).

## 3.2 Diffusional Flow (Diffusion Creep)

### 3.2.1 Nabarro-Herring Creep

*Nabarro* and *Herring* developed a model that describes viscous creep by stress-induced diffusion of vacancies [17, 18]. This mechanism applies to polycrystalline metals at high temperatures where all dislocations are assumed to be pinned and grain boundaries are considered as distinguished sources or sinks for vacancies.

By a stress  $\sigma$  normal to a boundary, vacancy formation is promoted, because the work necessary to form a vacancy is reduced by the amount  $\sigma\Omega$ , where  $\Omega$  is the volume of the vacancy ( $\Omega \approx b^3$ ) and  $b$  is the magnitude of Burgers' vector).

The equilibrium probability of finding a vacancy near a grain boundary (e.g. surface A and B in Fig. 13) is given by [19]:

$$\left[ \frac{N_V}{N_S} \right]_{\sigma} = \exp\left(-\frac{F_f}{kT}\right) \exp\left(\frac{\sigma\Omega}{kT}\right). \quad (9)$$

Here  $N_V$  is the number of vacancies for  $N_S$  lattice sites and  $F_f$  is the free energy for vacancy formation. If a grain is loaded by normal stresses  $\sigma$  (see Fig. 13), then the vicinity of faces A and B show vacancy concentrations  $\sim \exp(\sigma\Omega/kT)$  while the immediate

surroundings of faces C and D have concentrations  $\sim \exp(-\sigma\Omega/kT)$ . Therefore a concentration gradient is established which causes a vacancy flow from A and B to C and D [19] as indicated in Fig. 13.

Simultaneously the vacancy flow is accompanied by a matching flow of atoms in the opposite direction (see Fig. 13). The mechanisms for these combined flows are well known (see for example [20]): The possibilities for diffusive atomic movements are by *direct interchange* of

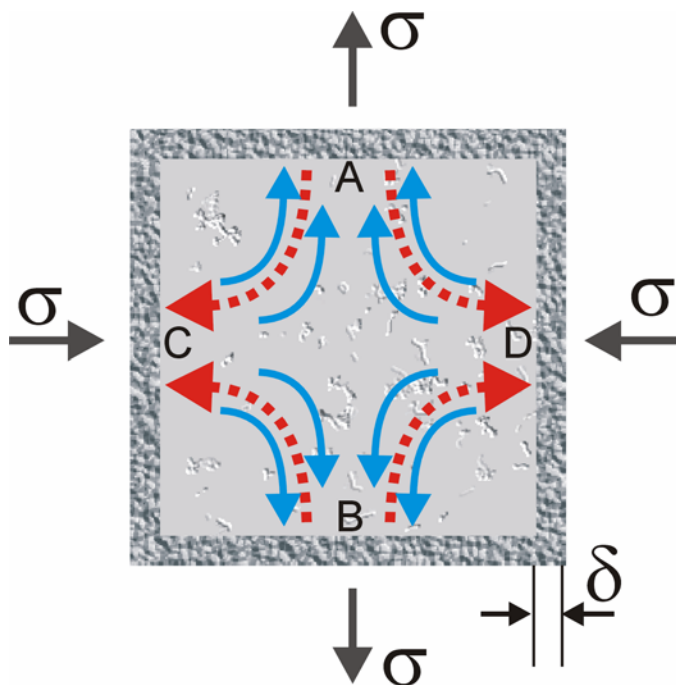


**Fig. 13:** Vacancy flow (red) and opposed atom flow (blue) in a grain under tensile and compressive stress (schematic drawing).

pairs of adjacent atoms, by *ring mechanisms*, by movement as *interstitial atoms*, or by *crowdion formation*. Additionally, in alloys the atomic flow can be considerably enhanced by the *Kirkendall effect*.

Together this leads to grain elongation or creep in the longitudinal direction and transversal contraction. Under the assumption that vacancy generation and annihilation are very rapid the concentration difference between neighboring grain faces (like A and C in Fig. 13) becomes

$$\Delta C = \frac{\alpha}{\Omega} \left[ \exp\left(\frac{\sigma \Omega}{kT}\right) - \exp\left(-\frac{\sigma \Omega}{kT}\right) \right] \exp\left(-\frac{F_f}{kT}\right), \quad (10)$$

where  $\alpha$  is a constant just less than unity, since the vacancy concentration at the boundaries differs slightly from the equilibrium value [19]. Obviously  $\sigma$  is not constant along the grain faces, and therefore the diffusion paths are shorter near the grain corners. Due to stress relaxation one can assume that  $\sigma = \beta \sigma_s$  at distances  $d/4$  from the boundaries ( $d$  is the grain size,  $\sigma_s$  is the macroscopic shear stress. and  $\beta$  is nearly unit). The length of a diffusion path through this point is  $l = \pi/2 (d/4)$  and the atomic flux across one atom area is then given by:

$$J = \frac{v}{b} D_v \frac{\Delta C}{l} = \frac{v}{b} D_v \frac{8\Delta C}{\pi d}, \quad (11)$$

where  $D_v$  is the diffusivity of vacancies. Further, the shear strain for each transferred atom is  $\gamma = 2b/d$  and with Eq. (10) the steady-state creep rate becomes:

$$\dot{\gamma}_s = \frac{32\alpha}{\pi d^2} D_s \sinh\left(\frac{\beta \sigma_s \Omega}{kT}\right). \quad (12)$$

Since the argument of the hyperbolic sine in Eq. (12) is small for low stresses the steady-state creep rate can be approximated by [19]:

$$\dot{\gamma}_s = \frac{32\alpha\beta D_s \sigma_s \Omega}{\pi d^2 kT}, \quad (13)$$

where  $D_s$  is the self-diffusion coefficient. This rate equation is widely known as *Nabarro-Herring creep*. The equation (13) agrees well with experimental results at very high temperatures, like for example on Ag [21], on Au [22], on Cu [23] or on  $\delta$ -Fe [24]. Other analyses of this diffusional flow at high temperatures have been shown by [25-27]. The resulting relations are similar to Eq. (13) but with different constants.

### 3.2.2 Coble Creep

Self-diffusion in poly crystals comprises two mechanisms: lattice and grain boundary diffusion. While lattice diffusion dominates at very high temperatures, grain boundary diffusion takes over mainly at lower temperatures (see for example [28, 20]). *Coble* described the diffusional flow at lower temperatures and stresses with the following rate equation (*Coble creep* [29]):

$$\dot{\gamma}_s = \frac{42\pi \delta \sigma_s \Omega}{d^3 kT} D_B . \quad (14)$$

Here  $D_B$  is the boundary diffusion coefficient and  $\delta$  the effective thickness of the grain boundary.

### 3.2.3 Alternative Descriptions

In most models for diffusion creep both mechanisms (Eqs. (13) and (14)) are combined in one rate equation (see, for example, [16]):

$$\dot{\gamma}_s = \frac{42\sigma_s \Omega}{d^2 kT} D_{eff} , \quad (15)$$

with

$$D_{eff} = D_L \left( 1 + \frac{\pi\delta}{d} \frac{D_B}{D_L} \right) . \quad (16)$$

Here  $D_L$  is the lattice diffusion coefficient.

At high temperatures a poly crystal may glide along its grain boundaries. Since faces of neighboring grain boundaries are usually randomly distributed, there are stress peaks at the grain edges. To get strains larger than about  $10^{-6}$  cm along a boundary the stress peaks have to be reduced by atomic flux, i.e. by diffusion. For this *Raj* and *Ashby* developed a reasonable model (see [30] or [31]): The arrangement of grain boundaries is simplified by a two-dimensional hexagonal network (Fig. 14) and the profile of the displacement face (e.g. for mode 1) is developed in a Fourier series. The first component of this series is described by its wave length  $\lambda$  and amplitude  $d/2$ . Grain displacement by a shear stress  $\sigma_s$  is then accompanied by normal stresses  $\sigma_n$  as shown in Fig. 15, where the normal stresses are given by:

$$\sigma_n = -4 \frac{\sigma_s \lambda}{\pi d} \sin\left(\frac{2\pi y}{\lambda}\right) \quad (17)$$

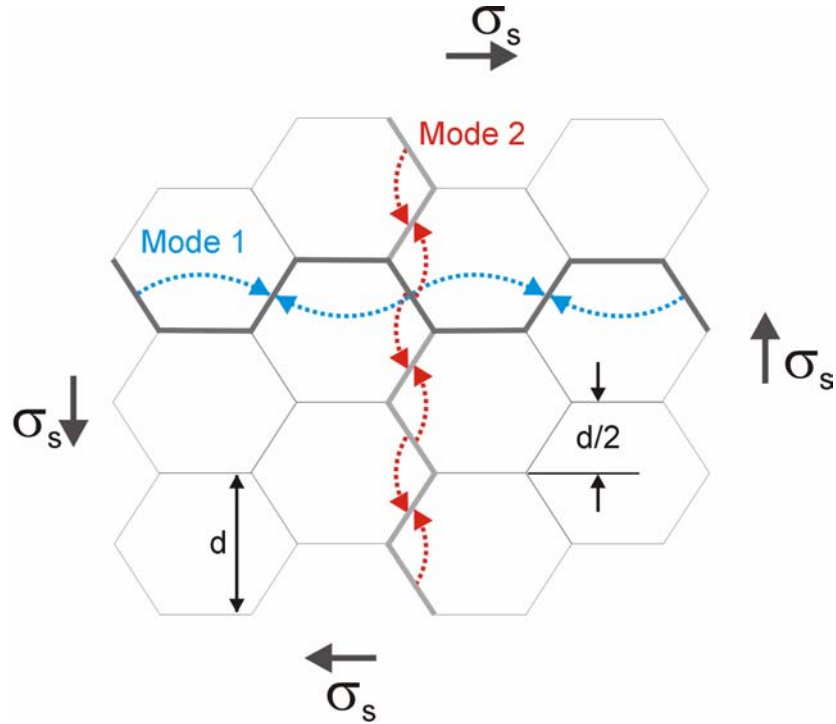


Fig. 14: Ideal poly crystal with a hexagonal network of grain boundaries which enables gliding on two orthogonal modes (blue and red). The vacancy flux is indicated with dotted arrows.

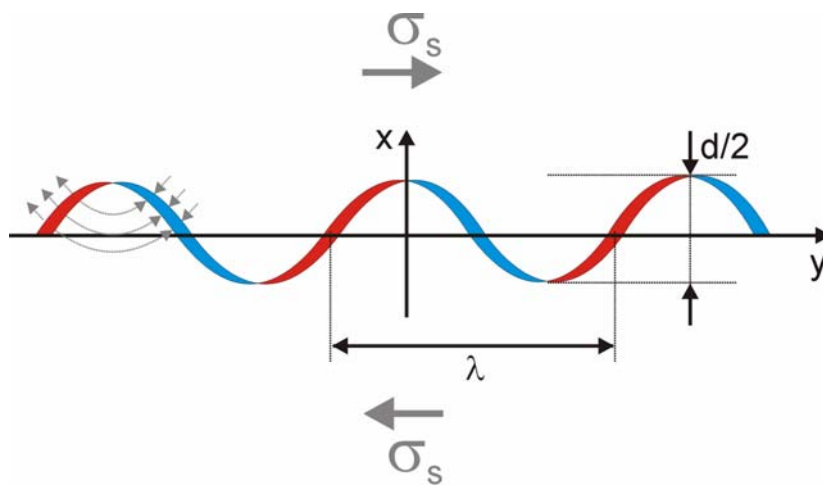


Fig. 15: Grain boundary gliding leads to cavities which are compensated by according flows of vacancies from expansion (red) to compression (blue) zones (indicated by arrows).

These normal stresses produce an additional chemical potential for the vacancy generation  $\Delta\mu = \sigma_n \Omega$  which forces the vacancies to flow from the expansion to the compression zones at the boundary (see Fig. 15).

This process defines the strain rate at the grain boundary [30, 31]:

$$\dot{\gamma}_s = \frac{64\sigma_s \Omega \lambda}{\pi d^3 kT} D_L \left( 1 + \frac{\pi \delta}{\lambda} \frac{D_B}{D_L} \right) . \quad (18)$$

It is a similar result like that from Nabarro, Herring, and Coble (Eqs. (15) and (16)). But here the lattice diffusion creep rate depends on  $\lambda/d^3$  instead of  $1/d^2$  while the grain boundary creep rate depends on  $\delta/d^3$  in both descriptions. That is, in Eq. (18) lattice diffusion is described not only by grain size but by the grain shape (with a shape factor  $d/\lambda$ ).

### 3.3 Power-law Creep (Dislocation Creep)

At high temperatures materials show rate dependent plasticity, or *creep*. Above  $0.3 T_M$  for pure metals and about  $0.4 T_M$  for alloys this dependence on strain rate becomes rather strong. It may be expressed by an equation of the form:

$$\dot{\gamma}_s \sim \left( \frac{\sigma_s}{\mu} \right)^n , \quad (19)$$

where  $\mu$  is the shear modulus and where  $n$  has a value between 3 and 10 in the high temperature regime. Therefore this deformation mechanism is called *power-law creep*.

#### 3.3.1 Power-law Creep by Climb (plus Glide)

At high temperatures dislocations acquire two degrees of freedom: they can climb as well as glide. If a gliding dislocation is blocked by discrete obstacles, a little climb may release it, and, therefore, enable it to glide to the next obstacles where the whole process is repeated. The glide step is responsible for almost all of the strain, while the average dislocation velocity is determined by the climb step. Mechanisms which are based on such a climb-plus-glide sequence are referred to as *climb-controlled creep* [32-34].

There is an important difference between **power-law creep** and the deformation mechanisms of the following sections like, for example, **dislocation glide** (low temperature plasticity, see Section 4.5): the rate-controlling process is the *diffusive motion of single ions or va-*

*cancies* to or from the climbing dislocations, rather than the *activated glide of the dislocation* itself. That is, the dominant process takes place at an atomic level.

A steady-state dislocation theory based on the climb of edge dislocations has been proposed by *Weertman* [35]. In his proposal it was assumed that work hardening occurs when dislocations are arrested and piled up against existing barriers such as grain boundaries or precipitates. The stress field at the tip of the piled-up dislocations induces multiple slip and the formation of *Lomer-Cottrell* sessile dislocations anywhere along the original piled-up dislocations. At this point dislocations beyond the *Lomer-Cottrell* barrier may easily escape by climb. But climb behind the *Lomer-Cottrell* barrier would lead to the generation of new dislocation loops and to a steady-state creep rate. This model can be applied very well to fcc and bcc metals.

In a further proposal *Weertman* [36] suggested that edge dislocations of opposite sign gliding on parallel slip planes would interact and pile up whenever a critical distance between slip planes is not exceeded. Like in the first model, dislocations may escape from the piled-up arrays by climb.

Dislocation pile-ups lead to work hardening while climb is a recovery process. Therefore, a steady-state condition is reached when the hardening and recovery rates are equal. The creep rate will then be controlled by the rate at which dislocations can climb. On the other hand, the climb mechanism requires that vacancies be created or destroyed at dislocations with sufficient ease and that in the vicinity of the dislocations an equilibrium concentration of vacancies be maintained at a level sufficient to satisfy the climb rate.

At the tip of a pile-up of dislocations a non-vanishing hydrostatic stress may exist which exerts a force on a dislocation in a direction normal to the slip plane and favors up or down climb. Vacancies are absorbed where the stress is compressive and they are created where the stress is tensile (compare previous section and Figs. 13-15). This results in a change in the vacancy concentration near a dislocation line. Therefore, a vacancy flux is established between segments of dislocations which act as sources and segments acting as sinks.

The vacancy concentration  $C_e$  in equilibrium with the lead dislocation in a pile-up is given by:

$$C_e = C_0 \exp\left(\frac{\pm 2L\sigma_s^2 b^2}{\mu kT}\right), \quad (20)$$

where  $2L$  is the length of the dislocation pile-up and  $C_0$  is the equilibrium concentration of vacancies in a dislocation free crystal. The vacancy concentration at a distance  $r$  from each pile-up is assumed to be equal to  $C_0$ . Thus the rate of climb  $\dot{X}$  is approximated by [19]:

$$\dot{X} = \frac{2C_0 D_v \sigma_s^2 L b^4}{\mu kT}, \quad (21)$$

where  $D_v$  is the coefficient for vacancy diffusion and with  $2Lb^2\sigma_s^2/\mu kT < 1$ . This relation has been obtained under the assumption that vacancies are easily destroyed or created and that an equilibrium concentration exists between pile-ups in the vicinity of dislocations. The diffusion problem for the flux of vacancies, however, may be different for specific climbing processes. Further, if vacancies are only created or destroyed at jogs, the energy of jog formation has to be taken into account in the case that they are formed by thermal fluctuations. On the other hand, if these are formed mechanically by intersection, then the rate of climb may still depend primarily on self-diffusion. This is certainly the case if it is accepted that vacancies will diffuse rapidly along a dislocation line toward or away from a jog.

For the second model by *Weertman* the rate of dislocation climb is given also by Eq. (21). The steady-state creep model in this case becomes:

$$\dot{\gamma}_s = NAb \frac{\dot{X}}{2r}, \quad (22)$$

where  $N$  is the density of dislocations participating in the climb process or – for this model – the density of sources,  $A$  is the area swept out by a loop in the pile-up, and  $2r$  is the separation between pile-ups. The stress necessary to force two groups of dislocation loops to pass each other on parallel slip planes has to be greater than  $\mu b/4\pi\sigma_s$ . Thus an estimate of  $r$  may be used with:

$$r = \frac{\mu b}{4\pi\sigma_s}. \quad (23)$$

Further, the probability  $p$  of blocking the dislocation loops generated from one source by loops emanating from three other loops is given by:

$$p = \frac{2NL^2 \mu b}{3\sigma_s}. \quad (24)$$

Now the creep rate can be obtained from Eqs. (21)-(24) by setting  $p=1$ ,  $A=4\pi L^2$ , and by the assumption that self-diffusion occurs by vacancy migration. The creep rate at low stresses becomes [19]:

$$\dot{\gamma}_s = \frac{c\pi^2\sigma_s^{4.5}D_s}{\sqrt{bN\mu^7}kT}, \quad (25)$$

where  $c$  is a numerical constant of about  $\frac{1}{4}$  and  $D_s$  is the coefficient for self-diffusion.

Equation (25) has been proofed experimentally for pure metals at low stresses to a greater extent than any other theoretical creep relation [19]. Although exceptions exist to the exponent of 4.5 on the stress, this value is remarkably close to observed values. There is general agreement that high temperature creep is diffusion-controlled and that it depends on  $D_s$ . It was shown for many metals tested at various temperatures [37, 38] that a plot of  $\ln[\dot{\gamma}/D_s]$  against  $\ln[\sigma_s/\mu]$  reduces the experimental results into a single band, further substantiating Eq. (25).

On the other hand, there are some points and observations which don't fit to this theory. It is questionable whether pile-ups can result from the interaction between edge dislocations of opposite sign gliding on parallel slip planes. Calculations have shown that the interaction between such dislocations does not impede their motion. They can cross over each other and form dipoles which in turn are mobile (see, for example, [39]). Further, in this theory the number of dislocations in a pile-up is given by  $2\sigma_s L/\mu b$  which predicts extensive pile-ups at high stresses but not necessarily at low stress levels.

Another deduction of power-law creep based on climb-plus-glide is given in [16] which is briefly outlined in the following:

Above about  $0.6 T_M$  climb is generally *lattice-diffusion* controlled. The velocity  $v_c$  at which an edge dislocation climbs under a local normal stress  $\sigma_n$  acting parallel to its Burgers' vector can be approximated by [40]:

$$v_c \approx \frac{D_L \sigma_n \Omega}{bkT}, \quad (26)$$

where  $D_L$  is the lattice diffusion coefficient and  $\Omega$  the atomic volume. The basic climb-controlled creep equation may then be obtained under the assumption that  $\sigma_n$  is proportional to the applied stress  $\sigma_s$  and that the average velocity of the dislocation is proportional to the

rate at which it climbs. With Eq. (26), the *Orowan* theory [41], and an estimate of the density of mobile dislocations [42] the creep equation becomes:

$$\dot{\gamma} = c_1 \frac{D_L \mu b}{kT} \left( \frac{\sigma_s}{\mu} \right)^3, \quad (27)$$

with the approximation  $\Omega \approx b^3$ . All constants are incorporated in  $c_1$  which is of order unity.

Some materials – but they are exceptions – obey this equation with a power of 3 and a constant  $c_1$  of about 1 [43]. It appears that the local normal stress is not necessarily proportional to  $\sigma_s$  implying that dislocations may be moving in a cooperative manner which concentrates stress. Or the density of mobile dislocations varies in more complicated manner than assumed by [42]. Over a limited range of stress – up to about  $10^{-3} \mu$  – experiments are well described by a modification of Eq. (27) [44]:

$$\dot{\gamma} = c_2 \frac{D_L \mu b}{kT} \left( \frac{\sigma_s}{\mu} \right)^n, \quad (28)$$

where the exponent  $n$  varies between 3 and about 10. However, present theoretical models for this behavior are unsatisfactory. None can convincingly explain the observed values of  $n$ . And further, the very large values of the dimensionless constant  $c_2$  strongly suggest that some important physical quantity is still missing from the equation (see, for example, [45, 43]). However, it provides a good description of experimental data and as generalization of Eq. (27) it has some basis as a physical model.

But Eq. (28) cannot describe the increase of the exponent  $n$  and the drop of the activation energy for creep at lower temperatures which are experimental facts. To incorporate these observations one has to assume that the transport of matter via *dislocation core diffusion* contributes significantly to the overall diffusive transport of matter. And under certain conditions this mechanism should become dominant [46]. A possibility to include the contribution of core diffusion is the definition of an effective diffusion coefficient (see [47] and [46]):

$$D_{eff} = D_L f_L + D_C f_C, \quad (29)$$

where  $D_C$  is the core diffusion coefficient, and  $f_C$  and  $f_L$  are the fractions of atom sites associated with each type of diffusion. The value of  $f_L$  is nearly unity while the value of  $f_C$  is determined by the dislocation density  $\rho$ :

$$f_C = a_c \rho, \quad (30)$$

where  $a_c$  is the cross-section area of the dislocation core in which fast diffusion is taking place. Measurements of the quantity  $a_c D_C$  can be found in [48]: the diffusion enhancement depends on the dislocation orientation (it is probably 10 times larger for edge than for screw dislocations) and on the degree of dissociation (and therefore on the arrangement of the dislocations). Even the activation energy is not constant. But in general,  $D_C$  is about approximately equal to the grain boundary diffusion constant  $D_B$ , if  $a_c$  is taken to be  $2\delta^2$  ( $\delta$  is the effective grain boundary thickness). A common experimental observation for the dislocation density is (see, for example, [42] or [59] for the case of tungsten in the creep regime):

$$\rho \approx \frac{10}{b^2} \left( \frac{\sigma_s}{\mu} \right)^2, \quad (31)$$

Then the rate equation for power-law creep with an effective diffusion coefficient becomes:

$$\dot{\gamma}_s = c_2 \frac{\mu b}{kT} \left( \frac{\sigma_s}{\mu} \right)^n D_L \left[ 1 + \frac{10 a_c}{b^2} \left( \frac{\sigma_s}{\mu} \right)^2 \frac{D_C}{D_L} \right], \quad (32)$$

Equation (32) is a combination of two rate equations. At high temperatures and low stresses lattice diffusion is dominant ( $\dot{\gamma}_s \sim \sigma_s^n$ ) while at higher stresses (or low temperatures) core diffusion is the dominant process ( $\dot{\gamma}_s \sim \sigma_s^{n+2}$ ).

### 3.3.2 Power-law Breakdown

At high stresses above about  $10^{-3} \mu$  the simple power-law breaks down. The measured strain rates are significantly greater than predicted by Eq. (32). This process is evidently a transition from climb-controlled to glide-controlled flow, that is, it is a transition from diffusion-controlled to thermally activated mechanisms. There have been numerous attempts to describe it empirically and most descriptions lead to the generalized form ([60, 61, 19]):

$$\dot{\gamma} \sim [\sinh(c' \sigma_s)]^n \exp \left[ -\frac{Q_{cr}}{RT} \right], \quad (33)$$

which reduces to a simple power-law at low stresses ( $c' \sigma_s < 0.8$ ) and which becomes an exponential at high stresses ( $c' \sigma_s > 1.2$ ).

Measurements of the activation energy  $Q_{cr}$  in the power-law breakdown regime often give values which exceed that of self-diffusion. This might indicate that the recovery process dif-

fers from that of climb-controlled creep. Some of the difference, however, may simply result from the temperature dependence of the shear modulus which has a greater effect when the stress dependence is in the exponential region. Then a better fit to experiment may be found by [16]:

$$\dot{\gamma} = A \left[ \sinh \left( \frac{a' \sigma_s}{\mu} \right) \right]^n \exp \left[ - \frac{Q_{cr}}{RT} \right], \quad (34)$$

The equation may be rewritten for an exact correspondence with the power-law equation (32). Then the rate-equation for both *power-law creep* and *power-law breakdown* reads as follows [16]:

$$\dot{\gamma}_s = A' \frac{\mu b}{kT} \left[ \sinh \left( a' \frac{\sigma_s}{\mu} \right) \right]^n D_L \left[ 1 + \frac{10 a_c}{b^2} \left( \frac{\sigma_s}{\mu} \right)^2 \frac{D_C}{D_L} \right]. \quad (35)$$

### 3.4 Mechanical Twinning

Twinning is an important deformation mechanism at low temperatures in hcp and bcc metals (and some ceramics). In fcc metals (like the austenitic steel AISI 316 considered in this work) it is less important and occurs only at *very low* temperatures. The tendency of fcc metals to twin increases with decreasing stacking fault energy being greatest for silver and completely absent in aluminium. Therefore, and because existing descriptions are rather uncertain, it is just mentioned briefly in the following.

Twinning is a variety of dislocation glide involving the motion of partial – instead of complete – dislocations. The kinetics of the process, however, often indicates that nucleation – and not propagation – determines the rate flow. Anyway, it may still be possible to describe the strain rate by a rate equation for twinning by [16]:

$$\dot{\gamma} = \dot{\gamma}_t \exp \left[ - \frac{\Delta F_N}{kT} \left( 1 - \frac{\sigma_s}{\sigma_t} \right) \right]. \quad (36)$$

Here  $\Delta F_N$  is the activation free energy to nucleate a twin without the help of external stress,  $\dot{\gamma}_t$  is a constant which includes the density of available nucleation sites and the strain produced for a successful nucleation, and  $\sigma_t$  is the stress required to nucleate twinning in the

absence of thermal activation. Further the temperature dependence of  $\Delta F_N$  must be included to explain the observation that the twinning stress may decrease with decreasing temperature (see [49]).

### 3.5 Dislocation Glide (Low Temperature Plasticity)

Below the ideal shear strength flow by the conservative or glide motion of dislocations is possible, provided a sufficient number of independent slip systems is available. This motion is almost always *obstacle-limited*, i.e., it is limited by the interaction of potentially mobile dislocations with other dislocations, with solute or precipitates, with grain boundaries, or with the periodic friction of the lattice. These interactions determine the rate of flow and – at a given rate – the yield strength. **Dislocation glide** is a *kinetic process* while **dislocation climb** (plus glide) is a *diffusion-controlled process*, as outlined in Section 4.3. This kinetic process was first described by *Orowan* [41]: Mobile dislocations with a density  $\rho_m$  move through a field of obstacles with an average velocity  $\bar{v}$ ; the velocity is almost entirely determined by their waiting time at the obstacles; the strain rate they produce due to their movement is then given by:

$$\dot{\gamma} = \rho_m b \bar{v} , \quad (37)$$

where  $b$  is the magnitude of the Burgers' vector of a dislocation. At steady state the density of mobile dislocations  $\rho_m$  is a function of stress and temperature only. The simplest function – consistent with both theory and experiment – is given by [42]:

$$\rho_m = \alpha \left( \frac{\sigma_s}{\mu b} \right)^2 , \quad (38)$$

where  $\alpha$  is a constant of order unity. The velocity  $\bar{v}$  depends on the force  $F$  acting on the dislocation by:

$$F = \sigma_s b , \quad (39)$$

and on its *mobility*  $M$ :

$$\bar{v} = M F . \quad (40)$$

Now the problem is to calculate  $M$ , and therefore  $\bar{v}$ . In the most interesting range of stress  $M$  is determined by the rate at which dislocation segments are thermally activated through or round obstacles. The next difficulty encounters by the fact that the velocity is always an ex-

ponential function of stress, but the details of the exponent depend on the shape and nature of the obstacles. So at first sight there are as many rate equations as there are types of obstacles. But on closer examinations obstacles can be divided in two broad classes: discrete obstacles and extended, diffuse barriers to dislocation motion.

Examples of the first type are strong dispersoids or precipitates which can be *bypassed* individually by a moving dislocation. Other examples of discrete obstacles are forest dislocations or weak precipitates which may be *cut* by dislocation movements. Obstacles of the second class are concentrated solutions or the lattice itself which leads to *lattice-friction*.

### 3.5.1 Plasticity Limited by Discrete Obstacles

The velocity of dislocations in a polycrystal is frequently determined by the strength and density of the discrete obstacles it contains. If the free energy of activation for cutting or bypassing an obstacle is  $\Delta G(\sigma_s)$ , the mean velocity is given by the kinetic equation (see [50-52, 16]):

$$\bar{v} = \beta b \nu \exp\left[-\frac{\Delta G(\sigma_s)}{kT}\right], \quad (41)$$

where  $\beta$  is a dimensionless constant and  $\nu$  is a frequency.

The quantity  $\Delta G(\sigma_s)$  depends on the distribution of obstacles and on the pattern of internal stress which characterizes one of them. A regular array of box-shaped obstacles – each one viewed as a circular patch of constant, adverse, internal stress – leads to the simple result [16]:

$$\Delta G(\sigma_s) = \Delta F \left(1 - \frac{\sigma_s}{\hat{\tau}}\right), \quad (42)$$

where  $\Delta F$  is total free energy – the activation energy – required to overcome the obstacle without aid from external stresses. The material property  $\hat{\tau}$  is the stress which reduces  $\Delta G$  to zero, forcing the dislocation through the obstacle without help from thermal energy. It can be thought of as the flow strength of the solid at 0 K.

But obstacles are seldom box-shaped and regularly spaced. Therefore, to describe other obstacle shapes as well as random distribution, the equation may be rewritten in the following way [51]:

$$\Delta G(\sigma_s) = \Delta F \left[ 1 - \left( \frac{\sigma_s}{\hat{\tau}} \right)^p \right]^q . \quad (43)$$

The values of  $p$ ,  $q$ , and  $\Delta F$  are bounded, i.e., all models lead to values of [16]:

$$\begin{aligned} 0 &\leq p \leq 1 \\ 1 &\leq q \leq 2 \end{aligned} . \quad (44)$$

The importance of  $p$  and  $q$  depends on the magnitude of  $\Delta F$ . When  $\Delta F$  is large, their influence is small and their choice is unimportant. Therefore, for discrete obstacles  $p = q = 1$  is a good choice. But when  $\Delta F$  is small, the choice becomes more critical. In this case (e.g. for diffuse obstacles)  $p$  and  $q$  have to be fitted to the experimental data (see also Section 4.5.2).

The strain rate sensitivity of the strength is determined by  $\Delta F$  (it characterizes the strength of a single obstacle). It is helpful to categorize obstacles by their strength as shown in Table 2; examples for typical values of  $\Delta F$  are  $2 \mu b^3$  for large or strong precipitates, and  $0.5 \mu b^3$  for pure metals in the work-hardened state.

The quantity  $\hat{\tau}$  is the shear strength in the absence of thermal energy. It reflects not only the strength but also the density and arrangement of the obstacles. For widely spaced, discrete obstacles  $\hat{\tau}$  is proportional to  $\mu b/l$ , where  $l$  is the obstacle spacing. The actual value of  $\hat{\tau}$  depends on obstacle strength and distribution (see Table 2). For pure metals strengthened by work-hardening it can be simply assumed that  $\hat{\tau} = \mu b/l$ .

At this point a combination of all the above listed equations leads to the *rate equation for discrete obstacle controlled plasticity*:

$$\dot{\gamma}_s = \alpha \beta v \left( \frac{\sigma_s}{\mu} \right)^2 \exp \left[ - \frac{\Delta F}{kT} \left( 1 - \frac{\sigma_s}{\hat{\tau}} \right) \right] . \quad (45)$$

When  $\Delta F$  is large (as is normally the case), the stress dependence of the exponential is so large compared to the pre-exponential  $\dot{\gamma}_0$  that it may be set constant for a reasonable fit to experimental data:

$$\dot{\gamma}_0 = \alpha \beta v \left( \frac{\sigma_s}{\mu} \right)^2 \approx 10^6 \frac{1}{s} . \quad (46)$$

**Table 2: Characteristics of obstacles, where  $\Delta F$  is the activation energy for a dislocation to overcome an obstacle,  $\hat{\tau}$  is the shear strength at 0 K, and  $l$  is the obstacle spacing [16].**

Obstacle Strength	$\Delta F$	$\hat{\tau}$	Examples
Strong	$2 \mu b^3$	$> \frac{\mu b}{l}$	dispersions; large or strong precipitates
Medium	$0.2 - 1.0 \mu b^3$	$\approx \frac{\mu b}{l}$	forest dislocations; radiation damage; small or weak precipitates
Weak	$< 0.2 \mu b^3$	$\ll \frac{\mu b}{l}$	lattice resistance; solution hardening

### 3.5.2 Plasticity Limited by Lattice Friction

The velocity of dislocations in most polycrystalline solids is limited by an additional sort of barrier – the interaction with the atomic structure itself. This *Peierls force* or *lattice resistance* reflects the fact that the energy of the dislocation fluctuates with position. The amplitude and wavelength of the fluctuations are determined by the strength and separation of the interatomic bonds. The crystal lattice presents an array of long, straight barriers to the motion of the dislocation. It advances by throwing forward kink pairs (with help from the applied stress and thermal energy) which subsequently spread apart (see [53, 51, 39]).

It is usually the nucleation rate of kink pairs which limits the dislocation velocity. The free energy of activation for this event depends on the detailed way in which the dislocation energy fluctuates with distance and on the applied stress as well as on temperature. Like those for discrete obstacles, the activation energies for all reasonable shapes of lattice resistance form a family which can be described as before (Eq. (43)). Together with a choice of  $p$  and  $q$  adapted to experiments (see [16] or [54]) the final *rate equation for plasticity limited by lattice resistance* reads:

$$\dot{\gamma}_s = \dot{\gamma}_p \left( \frac{\sigma_s}{\mu} \right)^2 \exp \left[ - \frac{\Delta F_p}{kT} \left( 1 - \left( \frac{\sigma_s}{\hat{\tau}_p} \right)^{3/4} \right)^{4/3} \right], \quad (47)$$

where  $\Delta F_p$  is the free energy of an isolated pair of kinks and  $\hat{\tau}_p$  is (approximately) the flow stress at 0 K. The  $\sigma_s^2$  term in the pre-exponential has to be retained in this case, because  $\Delta F_p$  is relatively small. For bcc metals and ceramics  $\dot{\gamma}_p$  may be set to  $10^{11}/s$  [16].

### 3.6 Elastic Collapse

The *ideal shear strength* defines a stress level above which deformation of a perfect crystal – or of one in which all defects are pinned – ceases to be elastic and becomes catastrophic. Then the crystal structure becomes mechanically unstable. The instability condition – and hence the ideal shear strength at 0 K – can be calculated from the crystal structure and an inter-atomic force law by simple statics, provided the inter-atomic potential is known for the material of interest (see, for example, [55, 56]).

But above 0 K the problem becomes a kinetic one: The frequencies at which dislocation loops nucleate and expand in an initially defect-free crystal have to be calculated. Since the focus in the present work lies on creep behavior, a simple description of the elastic collapse seems to be sufficient:

$$\begin{aligned} \dot{\gamma}_s &= \infty & \text{for } \sigma_s &\geq \alpha\mu \\ \dot{\gamma}_s &= 0 & \text{for } \sigma_s &< \alpha\mu \end{aligned} \quad (48)$$

Most often it is assumed that the temperature dependence of the ideal shear strength is the same as for the shear modulus  $\mu$ . For fcc metals the constant  $\alpha$  takes values of about 0.06, for bcc metals it is about 0.1 [16].

However, for a creep model this stress range is not of interest and will be neglected in the further considerations.

### 3.7 Summary

The present section provides an overview of the main deformation mechanisms and their description that will be used in the following Section for modeling the creep behavior of the 316L(N) steel.

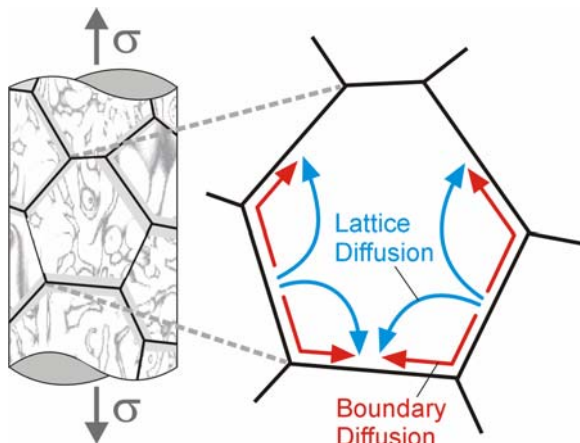


**Fig. 16:** Diffusion creep is dominated by two processes. At high temperatures lattice diffusion controls the rate (*Nabarro-Herring creep*). Grain boundary diffusion (*Coble creep*) takes over at lower temperatures.

With usual creep tests diffusion creep becomes detectable only for temperatures well above  $0.6 T_m$ . At the same time, the applied tensile stresses have to be smaller than the yield limit. In this range, boundary diffusion controls the strain rate which is also called *Coble creep*. At even higher temperatures (about  $0.8 T_m$  for austenitic stainless steels), lattice diffusion (*Nabarro-Herring creep*) takes over (see Fig. 16).

For the combined description of these two diffusion mechanisms we use equations (15) and (16).

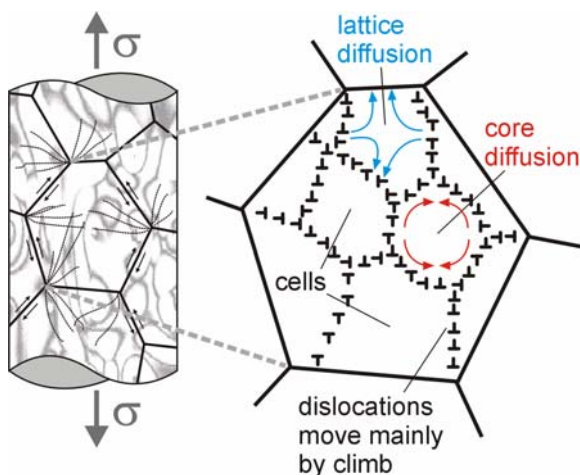


**Fig. 17:** Power-law creep is mainly based on diffusion controlled dislocation climb processes. Diffusion may occur along dislocation cells or through the lattice.

For tensile stresses above the yield limit dislocations start to glide and pile up at obstacles. They may be released by climb motions. Dislocation climbing is a rather slow process which is mainly controlled by diffusion. Therefore, climb-controlled power-law creep has to be described by lattice diffusion and core diffusion (see Fig. 17)

Both mechanisms are included in the rate equation (32). At high temperatures and low stresses lattice diffusion is dominant ( $\dot{\gamma}_s \sim \sigma_s^n$ ) while at higher stresses (or low temperatures) core diffusion is the domi-

nant process ( $\dot{\gamma}_s \sim \sigma_s^{n+2}$ ).

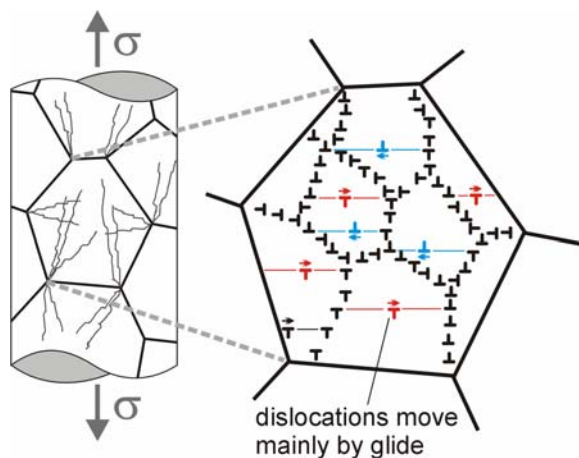


**Fig. 18:** For stresses about higher than  $10^{-3} \mu$  the power-law breaks down. A transition from climb-controlled to glide-controlled flow takes place.

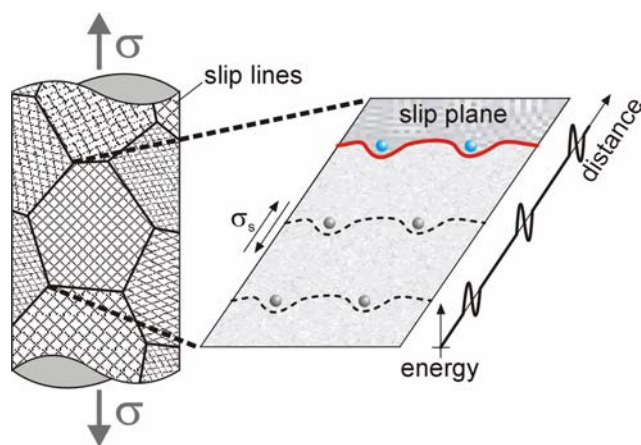


**Fig. 19:** Below the ideal shear strength flow by the conservative or glide motion of dislocations is possible, provided a sufficient number of independent slip systems is available. This motion is almost always obstacle-limited.

At stresses higher than about 0.1 % of the shear modulus a transition takes place. With increasing stress the glide-controlled flow dominates over the diffusion-controlled dislocation climb (see Fig. 18).

The generalized form of empirical descriptions for this transition range is given by Eq. (33).

At even higher stresses – but below the ideal shear strength – pure conservative motion of dislocations dominates (plasticity). This kinetic process (dislocation glide) is most often obstacle-limited (see Fig. 19) and may be described best by the *Orowan* formalism [41]. Depending on the type of obstacles this leads to different rate equations for the deformation description. In the present case a restriction to discrete obstacles is sufficient. The according description is given by Eq. (45).

A combination of all deformation descriptions combined with experimental results allow for compiling illustrative so-called deformation maps [57, 16]. These diagrams summarize deformation processes depending on stress and temperature.

The present work, however, is restricted to deformation rates which are typical for creep studies.

## 4 Steady-State Creep Model

### 4.1 Diffusion Creep

For the description of diffusion creep we use Eqs. (15) and (16), that is

$$\dot{\gamma}_{sC} = 42 \Omega \frac{1}{d^2} \frac{\sigma_s}{kT} \left( D_L + \frac{\pi\delta}{d} D_B \right), \quad (49)$$

where  $D_L$  and  $D_B$  are lattice and boundary diffusion coefficients, respectively, with

$$D_L = D_{0L} e^{-\frac{Q_L}{RT}} \quad \text{and} \quad D_B = D_{0B} e^{-\frac{Q_B}{RT}}. \quad (50)$$

In this model most constants are well known, like the atomic volume  $\Omega$ , grain size  $d$ , and grain boundary thickness  $\delta$  (see Appendix 6.1). Values for the lattice diffusion coefficient  $D_{0L}$  and activation energy  $Q_L$  are taken from [16]. Since boundary diffusion data are not readily

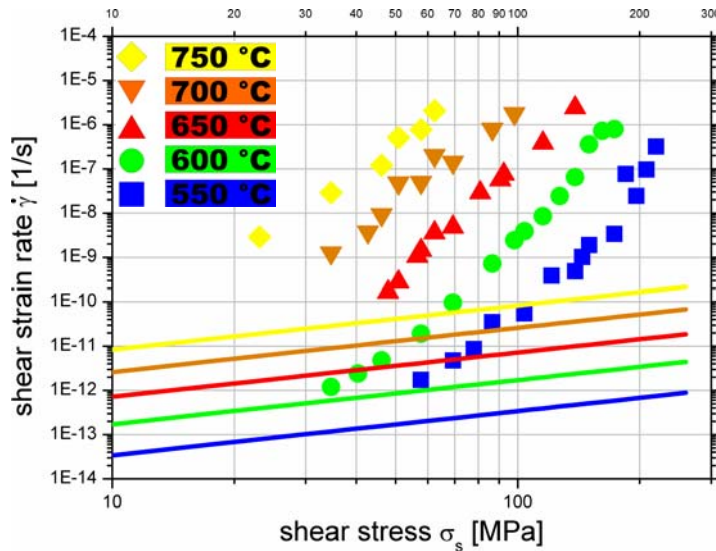


**Fig. 20:** Contribution of boundary diffusion creep to the strain rate according to the model given by Eq. (49). (Symbols represent experimental results).

available for the present material the according values have to be adjusted to the experiments and reasonable assumptions. In our case the boundary diffusion activation energy  $Q_B$  has been chosen to be 200 kJ/mol which is about 20 % higher than the value reported for 316 steels [16]. With this, the assumption that the contributions of lattice and boundary diffusion are equal at about 0.6  $T_M$  leads to a value for  $D_{0B}$  of  $6 \cdot 10^{-6} \text{ m}^2/\text{s}$ .

As can be seen in Fig. 20, only the long-term creep tests performed at 600 °C are near the range dominated by boundary diffusion creep. According to our model, all other tests have not been influenced by diffusion creep.

Figure 21 shows both boundary and lattice diffusion as predicted by the model given by Eq.

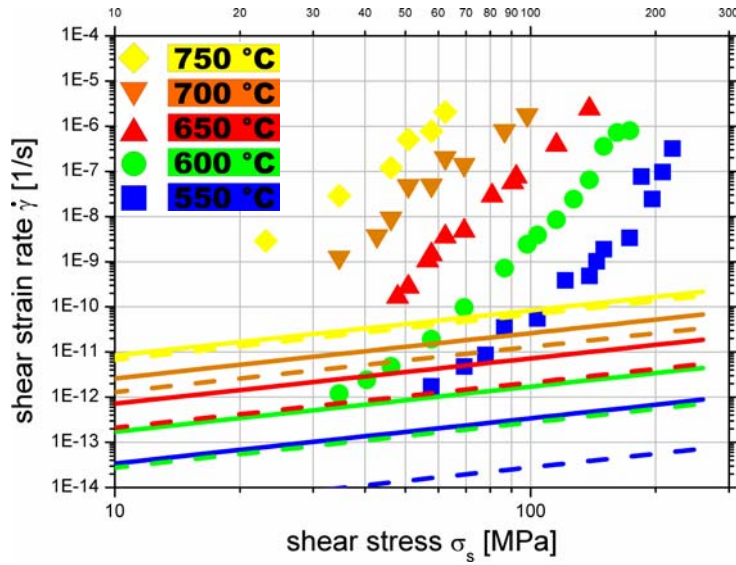


Fig. 21: Contribution of boundary diffusion creep (continuous lines) and lattice diffusion creep (dashed lines) to the strain rate according to the model given by Eq. (49). (Symbols represent experimental results).

(49). It can be clearly seen that lattice diffusion certainly plays no role for the given temperature range. Its contribution to the strain rate becomes only relevant at much higher temperatures ( $> 0.6 T_M$ ) where it dominates over the contribution of grain boundary creep.

## 4.2 Plasticity (Dislocation Glide)

Low temperature plasticity is a high stress deformation mechanism. Therefore it plays only a minor role for creep. However, to cover the whole stress range in our model we use the simplified description for plasticity (Eqs. (45) and (46)) which reads then

$$\dot{\gamma}_{sp} = \dot{\gamma}_0 \exp\left[-\frac{\Delta F}{kT}\left(1 - \frac{\sigma_s}{\hat{\tau}}\right)\right] \quad \text{or} \quad \dot{\gamma}_{sp} = \dot{\gamma}_0 \exp\left[-\frac{Q_p}{RT}\left(1 - \frac{\sigma_s}{\hat{\tau}}\right)\right]. \quad (51)$$

For the present material  $\hat{\tau}$  can be approximated as

$$\hat{\tau} \approx \frac{\mu b}{l}, \quad (52)$$

where  $b$  is the magnitude of Burgers' vector,  $l$  is the obstacle spacing, and  $\mu$  is the temperature dependent shear modulus given by

$$\mu = \mu(T) = \mu_0 \left(1 - 0.85 \frac{T - 300K}{T_M}\right). \quad (53)$$

Due to the large amount of precipitates the obstacle spacing takes a relatively small value of about 40 nm. The activation energy  $\Delta F$  has been estimated to be about  $0.75 \mu_0 b^3$  which correspond to  $Q_P = 460$  kJ/mol (all constants are given in Appendix 6.1).

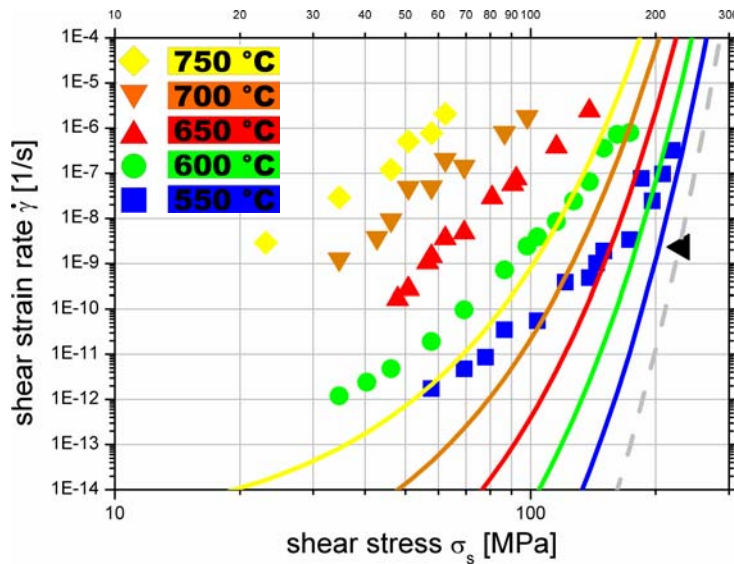


Fig. 22: Contribution of low temperature plasticity to the strain rate according to the model given by Eq. (51). The black triangle represents an additional creep test result at 500 °C. The grey dashed line corresponds also to 500 °C. (Symbols represent experimental results, lines are from model).

As has already been mentioned and as can be clearly seen from Fig. 22, the strain rates of creep tests are usually too small to approach the regime of plasticity. According to the model only the test results for 550 °C are close to this region.

For verification there is added an additional value of a creep test at 500 °C to the diagram in Fig. 22 which was deformed only plastically and which fits nicely to the model.

### 4.3 Power Law Creep (Dislocation Climb)

As has already been outlined in connection with Eq. (28) the current description of dislocation creep includes some degrees of freedom. Therefore the model has to be fitted to the experimental data. For this we use the experimental results from just three test temperatures in the following model setup. Then the resulting model can be verified with help of the data from the other two test temperatures.

Equation (32) describes the whole power-law creep including dislocation climb, activated by lattice and core diffusion. But as has been demonstrated with the diffusion creep model (Section 4.1, Fig. 21) lattice diffusion can be completely neglected within the present temperature range.

Therefore the expression for power-law creep reduces to

$$\dot{\gamma}_{sPL} = c_3 \frac{\mu b}{kT} \left( \frac{\sigma_s}{\mu} \right)^{n+2} D_C, \quad (54)$$

where  $D_C$  is the core diffusion coefficient with

$$D_C = D_{0C} e^{-\frac{Q_C}{RT}}. \quad (55)$$

$D_C$  is of the same order of magnitude as the grain boundary diffusion constant  $D_B$  and has therefore been chosen to be  $10^{-5} \text{ m}^2/\text{s}$ . Again, the shear modulus  $\mu$  depends on temperature as given in Eq. (53).

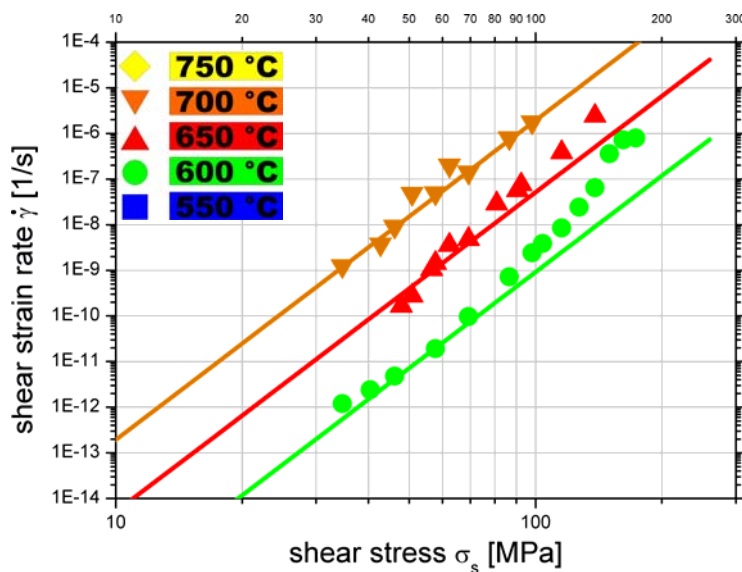


Fig. 23: Contribution of power-law creep to the strain rate according to the model given by Eqs. (54) and (55). For the adjustment of the three free parameters only results gained at 600 °C, 650 °C, and 700 °C are considered. (Symbols represent experimental results, lines are from model).

This leaves three remaining parameters – the exponent  $n$ , the activation energy  $Q_C$ , and the constant  $c_3$  – which have to be fitted to the experimental data. In log-log-representation the slope is defined by  $n$ , the vertically distance by  $Q_C$ , and the offset by  $c_3$ .

The according result is shown in Fig. 23. Here the parameters have been chosen as follows:  $Q_C = 520 \text{ kJ/mol}$ ,  $n = 5$ , and  $c_3 = 2 \cdot 10^{20}$ .

#### 4.4 Transition from Creep by Climb to Creep by Glide

At stresses above about  $10^{-3} \mu$  the power-law breaks down. That is, starting from this point (for the present material the onset is at 86 MPa) the model has to describe a transition from creep by climb (power-law) to creep by glide (plasticity).

Adapting Eq. (35) to the present model leads to

$$\dot{\gamma}_{sPLBD} = c_3 \left[ \sinh \left( \alpha' \frac{\sigma_s}{\mu} \right) \right]^{n+2} D_C \quad (56)$$

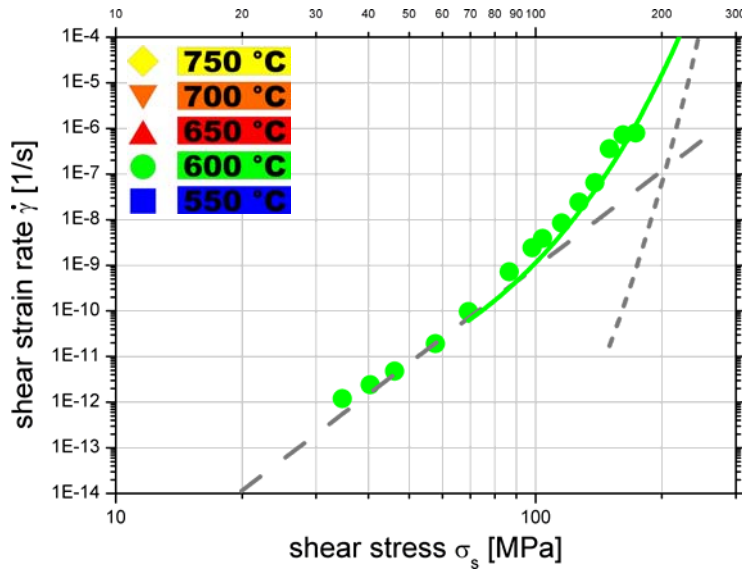


Fig. 24: Transition from power-law creep (long dashed gray line) to plasticity (short dashed gray line) according to the model given by Eq. (56). For the adjustment of the free parameter  $\alpha'$  only results gained at 600 °C are considered. (Symbols represent experimental results, lines are from model).

which leaves only one free parameter ( $\alpha'$ ) to fit to experiment. For this we have only used data from the 600 °C creep tests to verify the result later on with the other data. Figure 24 shows the transition curve according to  $\alpha' = 800$ .

#### 4.5 Assessment and Discussion of the Stationary Creep Model

To obtain the complete model all contributions have to be summed up accordingly:

$$\dot{\gamma}_s = \dot{\gamma}_{sC} + \dot{\gamma}_{sP} + \begin{cases} \dot{\gamma}_{sPL} & \text{for } \sigma_s \leq 86 \text{ MPa} \\ \dot{\gamma}_{sPLBD} & \text{for } \sigma_s > 86 \text{ MPa} \end{cases} \quad (57)$$

where the single contributions are given by the Eqs. (49), (51), (54), and (56). A comparison between the model and the experimental data is given in Fig. 25.

As can be seen, the transition from power-law creep to plasticity (which has been fitted to the 600 °C results) fits also nicely to the results gained at 550 °C and 650 °C. At higher temperatures the experiments have been performed at stresses below the transition range.

The power-law creep range which has been fitted to the 600 °C, 650 °C, and 700 °C experimental results, applies also for the 750 °C test results. But the experiments at 550 °C, however, are well above the predictions from the model.

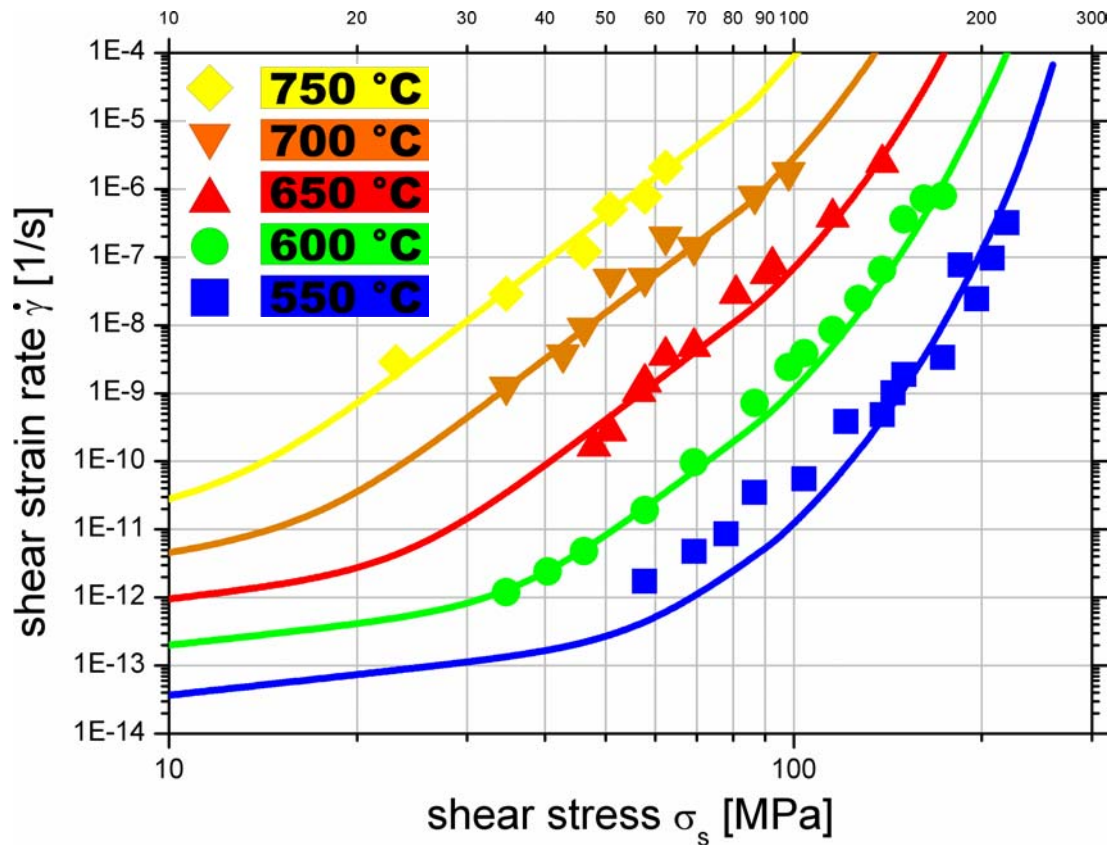


Fig. 25: The stationary creep model (lines) as defined by Eq. (57) compared to the experimental results (symbols).

As already mentioned, only the creep tests performed at 600 °C reach down to the range of diffusion creep. Therefore, it is not possible to verify the model for the other temperatures. But at least for 600 °C the model predictions fit perfectly to the experiments.

With the exception of the low-stress long-term creep test results at 550 °C there is a good agreement between experimental data and model prediction. Now the question is why the model doesn't resemble the low-stress 550 °C values, or vice versa. From a physically point of view it is rather unlikely that an additional deformation mechanism should occur only at lower temperatures. And since this stress range is dominated exclusively by diffusion based processes, it is even more questionable, that the strain rate should increase with lower temperatures compared to the applied power-law.

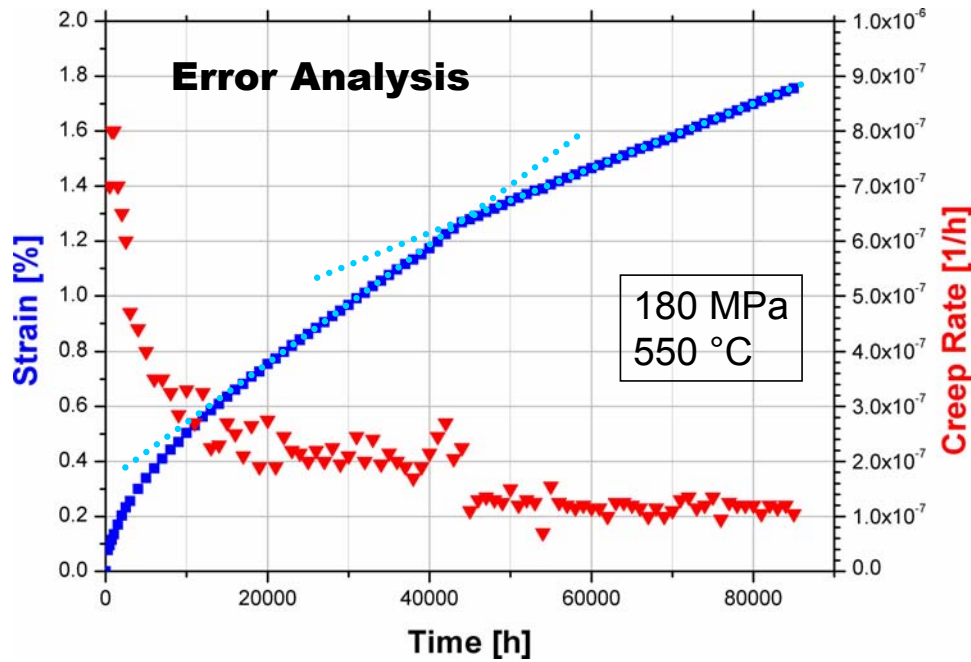


Fig. 26: After 44000 hours the creep rate suddenly drops from one stationary level down to another. If the test had been aborted at 40000 hours, everybody would have accepted the higher stationary creep rate as absolute minimum. Now even a further drop can be imagined.

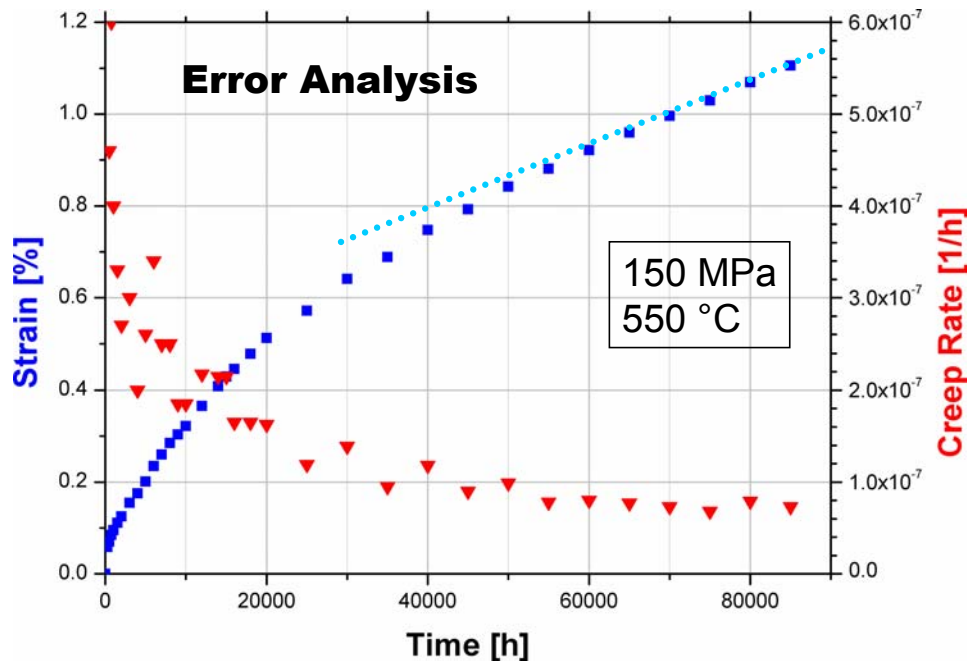


Fig. 27: The test was aborted after about 85000 hours because it was thought that stationary creep had already been reached. But now it can not be excluded that there could have been a drop in strain rate during a further continuation of this creep test similar to the observation in Fig. 26.

These considerations have necessitated a closer look on the experimental data (low stress results at 550 °C) and their evaluation. It revealed the situation depicted exemplarily in Fig. 26 and 27. In the case of 550 °C and 180 MPa (Fig. 26) there has been a sudden drop after

44000 hours from one stationary creep range to another. This creep test was aborted after 85000 hours with a specified minimum creep rate of about  $1.2 \cdot 10^{-7}$  1/h. But if this test had already been aborted after 40000 hours, nobody would have doubted the resulting value of  $2 \cdot 10^{-7}$  1/h. And now it has to be expected that there might have been further drops in strain rate, if the test had been continued.

The other example in Fig. 27 (150 MPa, 550 °C) shows no such drop in the strain rate curve. But obviously the given value for the minimum creep rate is now rather doubtful. It is easy to imagine that a continuation of the creep test could have led to much lower values.

The other creep tests at 550 °C in the low-stress range are similar to those of Fig. 26 and 27. That is, actually the according data had to be corrected towards lower values. Since quantitative statements are not possible, the only thing known is that the real values are lower than the already published results. This is indicated in Fig. 28 and gives even more reason to acknowledge the stationary creep model.

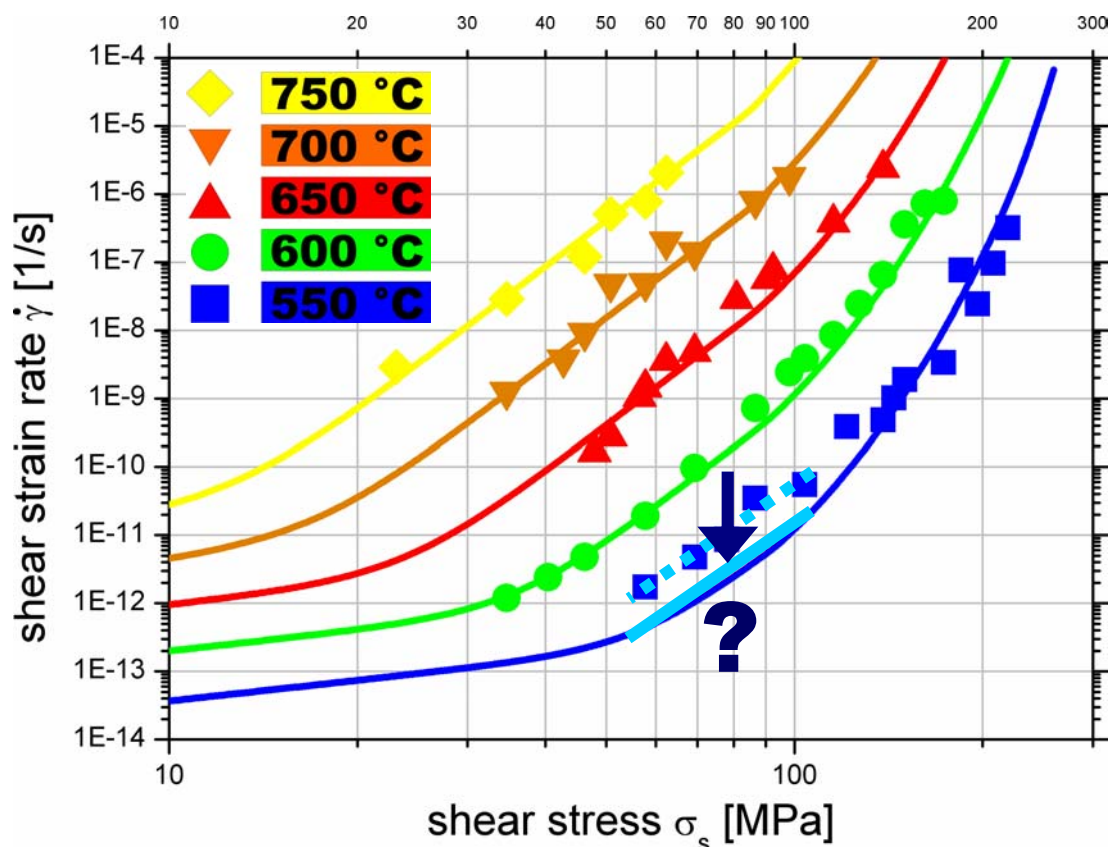


Fig. 28: The 550 °C low-stress data have to be corrected towards lower values since the according creep tests were aborted too early.

## 5 Conclusion

The present investigations have been mainly based on results from creep experiments performed at IMF-I, FZK with the austenitic stainless steel AISI 316 L(N) (heat no. 11477 from Creusot-Marell). Especially long-term creep tests have shown that there is a considerable change in the steady-state creep behavior at low stresses: the creep rates are much higher than the values that would have been expected by an extrapolation from the usual (higher) stress range. For component design this is a bad situation, because the real life-time would be significantly shorter compared to estimates based on the usually available creep data. Since AISI 316 type steel is a very common material for all kinds of applications – also for ITER components – it would be highly helpful, if it's seemingly odd steady-state creep behavior could be described by a far reaching model. The setup of such a model was the motivation of the current paper.

At first glance, there are three possible reasons for the kink in the creep rate vs. stress curve:

- (I) At very low stresses the initial strain is within the elastic range while at higher stresses specimens are deformed plastically at the start of the creep tests. This plastic deformation could act like cold working the material and, therefore, lead to higher creep strength.
- (II) Austenitic stainless steels are known for their thermal instability, that is, they are prone to aging. Hence, more or less severe formation of precipitations could change the microstructure significantly and cause higher creep rates, dependent on creep time which in turn is correlated to the applied stresses.
- (III) Creep rates depend on different stress-dependent deformation processes. If the stress dependency of these processes differs considerably – let's assume  $\sigma$  in one case and  $\sigma^7$  in another –, an according change of the steady-state creep rate would be obvious.

Reason (I) can be ruled out, because the decrease in initial strain takes place continuously with decreasing stresses. Cold work and accompanied hardening certainly plays a role in creep behavior, but this is not an explanation for the current dramatic change in creep rate at low stresses. Also precipitation formation can not be the reason for the observed creep behavior, since there is no correlation between the different precipitation types, the times of formation and the periods of steady-state creep. Of course, precipitations may also influence creep properties, but again, not in such a distinctive way as observed.

For a reasonable explanation this leaves only the interaction of different deformation mechanisms which have been reviewed in detail: diffusional flow, power-law creep, mechanical twinning, dislocation glide, and the elastic collapse.

It has been demonstrated that for a description of the steady-state creep behavior only grain boundary diffusion, power-law creep, and the transition from dislocation climb to dislocation glide are relevant, where the latter is just a limit that is barely reached with constant load creep tests. This leads to a model consisting of three main deformation mechanisms and two transitions:

- At very low stresses only grain boundary diffusion contributes to the strain rate which is proportional to the stress ( $\sim \sigma$ ). This regime can only be reached by performing extremely long-term tests. In the present case diffusion creep occurred allusively after 10 years at 600 °C.
- Then there is a relatively sharp transition to creep triggered by dislocation climb. In the present case dislocation climb depends on core diffusion and leads to creep rates proportional to the 7<sup>th</sup> power of stress ( $\sim \sigma^7$ ) – thus the name *Power-law Creep*.
- Starting from medium stresses there is a continuous transition from creep by dislocation climb to plasticity which depends solely on dislocation glide. The plasticity regime is usually not reached with creep tests. Here the strain rate depends exponentially on stress ( $\sim e^\sigma$ ).

To adapt the model to creep experiments with the AISI 316 L(N) steel it needs only a few parameters:

- grain boundary diffusion coefficient and activation energy to describe diffusion creep,
- a generic constant, the core diffusion coefficient and activation energy, and the power exponent to describe power-law creep,
- and just a generic constant for the description of the transition from power-law creep to plasticity.

For completeness of the model, plasticity may be described by four additional parameters.

To determine all parameters from experimental data, it needs creep tests at three different temperatures in the usual stress range and at least some long-term experiments which reach down into the diffusion creep regime. In the present case the latter was not quite fulfilled. Therefore, diffusion creep might be described somewhat too conservative. However, all data (with the exception of the 550 °C long-term experiments) fit nicely to the model predictions.

But it has been shown that these experiments were aborted too soon, that is, it was not possible to extract reliable minimum creep rates.

In summary, the presented steady-state creep model for the austenitic stainless steel AISI 316 L(N) is based on well known deformation mechanisms and can predict creep rates in the whole temperature range relevant for application design. Due to the small number of parameters it should be no problem to apply the rate equations to other materials.

## 6 Literature

1. T. Nakazawa, *Mat. Sci. Eng.* **A 148**, 253-260 (1988).
2. M. D. Mathew, International Conference on High Nitrogen Steels, HNS 88, Lille, France, 18-20 May, 1988.
3. M. Schirra, *Nucl. Eng. Design* **147**, 63-78 (1993)
4. M. Schirra, *Nucl. Eng. Design* **188**, 381-384 (1999).
5. M. Schirra, KfK-Reports 4767, 4861, and 6699, Forschungszentrum Karlsruhe, Germany, September 1990, August 1991, and February 2002.
6. NRIM-Creep Data Sheet No. 42-1996, National Research Institute for Metals, Tokyo, Japan.
7. M. Schirra, Annual Meeting on Nuclear Technology, Aachen, Germany, 13.-15. May 1997.
8. NRIM-Creep Data Sheet No. 14A-1982, National Research Institute for Metals, Tokyo, Japan.
9. NRIM-Creep Data Sheet No. 15A-1982, National Research Institute for Metals, Tokyo, Japan.
10. NRIM-Creep Data Sheet No. 45-1997, National Research Institute for Metals, Tokyo, Japan.
11. NRIM-Creep Data Sheet No. 6B-2000, National Research Institute for Metals, Tokyo, Japan.
12. M. Schirra, KfK-Report 4273, Forschungszentrum Karlsruhe, Germany, February 1988.
13. A. F. Padilha and P. R. Rios, *ISIJ International* **42**, 325-337 (2002).
14. P. R. Rios and A. F. Padilha, *Encyclopedia of Materials: Science and Technology*, K. H. Buschow et al. (Eds.), 7836-7841, Elsevier, Amsterdam, 2001.
15. NRIM-Metallographic Atlas of Long-term Crept Materials No. M-2, National Research Institute for Metals, Tokyo, Japan, 2003.
16. H. J. Frost, and M. F. Ashby, *Deformation-mechanism Maps*, Pergamon Press, Oxford, 1982.
17. F. R. N. Nabarro, in: *Report on Conference on Strength of Solids*, Phys. Soc. of London, 75, 1948.
18. C. Herring, *J. Appl. Phys.* **21**, 437 (1950).
19. F. Garofalo, *Fundamentals of Creep and Creep-Rupture in Metals*, MacMillan, New York, 1965.
20. B. Chalmers, *Physical Metallurgy*, John Wiley, New York, 1959.
21. A. P. Greenough, *Phil. Mag.* **43**, 1075 (1953).
22. B. H. Alexander, M. H. Dawson, and H. P. Kling, *J. Appl. Phys.* **22**, 439 (1951).
23. A. L. Pranatis, and G. M. Pound, *Trans. AIME* **203**, 664 (1955).
24. A. T. Price, H. A. Hall, and A. P. Greenough, *Acta Met.* **12**, 49 (1964).
25. E. Orowan, *J. West Scot. Iron and Steel Inst.* **54**, 45 (1946-47).
26. W. Kauzman, *Trans. AIME* **143**, 57 (1941).

27. A. H. Cottrell, and M. A. Laswon, Proc. Roy. Soc. **A 19**, 104 (1949).
28. P. G. Shewmon, in: *Physical Metallurgy*, ed. by R. W. Cahn, North-Holland Publishing Company, Amsterdam, 1965.
29. R. L. Coble, J. Appl. Phys. **34**, 1679, (1963).
30. R. Raj, and M. F. Ashby, Trans. AIME **2**, 1113 (1971).
31. P. Haasen, *Physikalische Metallkunde*, Springer-Verlag, Berlin, 1974.
32. J. Weertman, J. Mech. Phys. Solids **4**, 230 (1956).
33. J. Weertman, Trans. AIME **218**, 207 (1960).
34. J. Weertman, Trans. AIME **227**, 1475 (1963).
35. J. Weertman, J. Appl. Phys. **26**, 1213 (1955).
36. J. Weertman, J. Appl. Phys. **28**, 196 and 1185 (1957).
37. O. D. Sherby, Acta Met. **10**, 135 (1962).
38. D. McLean, Metallurgical Reviews **7**, 481 (1962).
39. D. Hull, *Introduction to Dislocations*, 2<sup>nd</sup> Edition, Pergamon Press, Oxford, 1975.
40. J. P. Hirth, and J. Lothe, *Theory of Dislocations*, McGraw Hill, 1968.
41. E. Orowan, Proc. Phys. Soc. **52**, 8 (1940).
42. A. S. Argon, Scripta Met. **4**, 1001 (1970).
43. A. M. Brown, and M. F. Ashby, Scripta Met. **14**, 1297 (1980).
44. A. K. Mukherjee, J. E. Bird, and J. E. Dorn, Trans. ASM **62**, 155 (1969).
45. R. L. Stocker, and M. F. Ashby, Scripta Met. **7**, 115 (1973).
46. S. L. Robinson, and O. D. Sherby, Acta Met. **17**, 109 (1969).
47. E. W. Hart, Acta Met. **5**, 597 (1957).
48. R. W. Balluffi, Phys. Stat. Sol. **42**, 11 (1970).
49. G. F. Bolling, and R. H. Richman, Acta Met. **13**, 709 and 723 (1965).
50. A. G. Evans, and R. D. Rawlings, Phys. Stat. Sol. **34**, 9 (1969).
51. U. F. Kocks, A. S. Argon, and M. F. Ashby, Prog. Mat. Sci. **19** (1975).
52. B. de Meester, C. Yin, M. Doner, and H. Conrad, in: *Rate Processes in Plastic Deformations*, ed. by J. M. C. Li and A. K. Mukherjee, A.S.M., 1973.
53. P. Guyot, and J. E. Dorn, Can. J. Phys. **45**, 983 (1967).
54. P. L. Raffo, J. Less-Common Metals **17**, 133 (1969).
55. W. R. Tyson, Phil. Mag. **14**, 925 (1966).
56. A. Kelly, *Strong Solids*, Oxford University Press, 1966.
57. M. F. Ashby, Acta Met. **20**, 887 (1972).
58. L. D. Blackburn, *The Generation of Isochronous Stress-Strain Curves*, ASME Winter Annual Meeting, New York, 1972.
59. R. R. Vandervoort, Met. Trans. **1**, 857 (1970).
60. C. M. Sellars and W. J. McG. Tegart, Mem. Sci. Rev. Met **63**, 731 (1966).
61. W. A. Wong and J. J. Jonas, Trans. AIME **242**, 2271 (1968).

## 7 Appendix/Tables

### 7.1 Constants and Parameters

The basic material constants for the present AISI 316 L(N) stainless steel as well as some physical constants are given in Table 3. All parameters used for the creep model are listed in Tables 4-6.

Table 3: Physical and material constants for the AISI 316 L(N) stainless steel.

Constant	Value	Ref.
Boltzmann's constant, $k$	$1.381 \times 10^{-23} \text{ J/K}$	
Gas constant, $R$	$8.314 \text{ J/(mol K)}$	
Melting temperature, $T_M$	$1810 \text{ K}$	[16]
Grain size, $d$	$\approx 100 \mu\text{m}$	measured
Thickness of grain boundary, $\delta$	$\approx 20 \times 10^{-9} \text{ m}$	measured
Atomic volume, $\Omega$	$1.21 \times 10^{-29} \text{ m}^3$	[16]
Lattice constant, $L_0$	$2.87 \times 10^{-10} \text{ m}$	[16]
Burger's vector (magnitude), $b$	$2.58 \times 10^{-10} \text{ m}$	[16]
Shear modulus at 300 K, $\mu_0$	$81000 \text{ MN/m}^2$	[58]
Temperature dependence of shear modulus, $\frac{T_M}{\mu_0} \frac{d\mu}{dT}$	-0.85	[58]

Table 4: Diffusion creep parameters used for the AISI 316 L(N) stainless steel.

Parameter	Value
Lattice diffusion coefficient, $D_{0L}$	$37.5 \times 10^{-6} \text{ m}^2/\text{s}$
Latt. diff. activation energy, $Q_L$	$280 \text{ kJ/mol}$
Boundary diffusion coefficient, $D_{0B}$	$6 \times 10^{-6} \text{ m}^2/\text{s}$
Bound. diff. activation energy, $Q_B$	$200 \text{ kJ/mol}$

Table 5: Plasticity parameters used for the AISI 316 L(N) stainless steel.

Parameter	Value
Activation energy, $Q_P$	460 kJ/mol
Activation energy, $\Delta F$	$1.04 \times 10^{-18} \text{ J}$
Obstacle spacing, $l$	40 nm
Pre-exponential, $\dot{\gamma}_0$	$10^6 \text{ 1/s}$

Table 6: Power-law and power-law break-down parameters used for the AISI 316 L(N) stainless steel.

Parameter	Value
Pre constant, $c_3$	$2 \times 10^{20}$
Core diffusion coefficient, $D_{0C}$	$10 \times 10^{-6} \text{ m}^2/\text{s}$
Core diff. activation energy, $Q_C$	520 kJ/mol
Creep exponent, $n$	5
Constant, $\alpha'$	800

## 7.2 Experimental Data

Table 7: Creep test results for the AISI 316 L(N) stainless steel. Specimen dimensions have been M5 x 30 mm.  $Z_u$ : reduction of area,  $A_u$ : total elongation,  $\varepsilon_0$ : initial strain,  $t_m$ : time to rupture.

Test No.	$T$ °C	$\sigma$ MPa	$t_m$ h	$\varepsilon_0$ %	$A_u$ %	$Z_u$ %	$\dot{\varepsilon}_{\min}$ $10^{-6}/h$
2986	500	400	5308	16.2	30.3	35.5	4.8
2982	550	380	24	25.7	45.3	70.8	660
2981		360	146	21.3	36.0	53.9	20
3023		340	560	16.0	26.0	35.8	51
3028		320	410	13.0	33.7	35.5	159
2984		300	2610	12.7	18.3	29.4	3.2
3029		260	5785	8.7	19.7	26.3	3.9
3105		240	15668	7.5	18.0	22.6	1
2974	600	300	61	11.0	33.7	38.6	1749
2976		280	83	10.0	41.3	38.9	1525
2979		260	164	8.8	40.3	38.9	733
3026		240	584	7.0	44.0	39.2	150
2977		220	1738	5.3	47.3	45.0	48
3038		200	5481	3.7	52.7	51.0	19
3041		180	11605	3.5	48.0	61.4	9.3
3184		150	50324	1.2	42.3	50.6	1.2
2980	650	240	23	8.3	45.7	53.6	5333
2978		200	116	6.0	69.7	61.4	1240
ZSV1911		160	1089	1.83	85.3	70.7	157
ZSV1944		140	2700	0.87	88.3	71.0	60
ZSV1941		120	7629	0.33	49.7	63.9	13.5
3046		100	16124	0.23	34.0	42.2	3.8
ZSV1943	700	170	59	2.07	52.3	63.8	3680
ZSV1917		150	125	1.80	62.0	75.0	1653
ZSV1925		120	626	0.50	77.3	78.8	293
ZSV1919		100	1383	0.15	76.3	80.7	102
ZSV1960		80	4208	0.13	62.7	59.1	19
ZSV2085		60	aborted	0.03			2.6
ZSV1939	750	100	152	0.13	97.7	80.6	1760
ZSV1940		80	440	0.23	79.7	82.8	318
ZSV1921		60	2650	0.04	77.0	64.0	60
ZSV1913		40	15692	0.03	29.6	32.9	10

Table 8: Low-stress long-term creep test results for the AISI 316 L(N) stainless steel. Specimen dimensions have been M8 x 200 mm.

Test No.	$T$ °C	$\sigma$ MPa	aborted after h	$\varepsilon_0$ %	$\dot{\varepsilon}_{\min}$ $10^{-6}/h$
3495	550	250	6100	7.5	2.1
3458		210	60000	4.83	0.8
3433		180	85000	2.85	0.115
3434		150	85000	1.18	0.073
3514		135	70006	0.34	0.018
3442		120	85000	0.16	0.0099
3443		100	85000	0.09	0.0036
3478	600	170	7500	3.03	5.0
3437		120	41015	0.32	0.2
3438		100	85000	0.07	0.04
3445		80	85000	0.06	0.01
3450		70	85000	0.055	0.005
3451		60	85000	0.04	0.0025

Table 9: Creep test results from NRIM (see Ref. 11) of the 18Cr-12Ni-Mo steel AAL. Only data from the medium stress range is considered since this material somewhat is different from the AISI 316 L(N) as well as the used test equipment.  $Z_u$ : reduction of area,  $A_u$ : total elongation,  $\varepsilon_0$ : initial strain,  $t_m$ : time to rupture.

NRIM ref. code	$T$ °C	$\sigma$ MPa	$t_m$ h	$\varepsilon_0$ %	$A_u$ %	$Z_u$ %	$\dot{\varepsilon}_{\min}$ $10^{-6}/h$
AAL	600	216	2444.5	2.35	62	76	50.9
		177	11007.5	1.04	49	80	3.10
		157	19646.2	0.38	61	78	1.05
		137	42079.8	0.13	61	75	0.312
		127	61463.9	0.12	51	67	0.208
		108	152758	0.08	26	39	0.068
AAL	650	157	811.4	0.78	54	83	171
		108	10477.6	0.13	46	40	7.45
		98	25771.7	0.05	34	48	2.18
		88	47073.3	0.06	22	41	0.576
		83	64516.7	0.07	29	39	0.346
AAL	700	108	624.4	0.1	66	82	416
		88	2357.0	0.08	70	72	99.8
		74	11817.9	0.05	35	51	7.74
AAL	750	108	62.4	0.15	90	86	4280
		88	234.0	0.07	72	84	1060
		53	7413.3	0.05	53	52	17.1

**Table 10: Low-stress long-term creep test results for the AISI 316 L(N) stainless steel at 550 °C (Time-Strain values). Specimen dimensions have been M8 x 200 mm.**

	$\varepsilon_0 =$ 7.50 %	$\varepsilon_0 =$ 4.83 %	$\varepsilon_0 =$ 2.85 %	$\varepsilon_0 =$ 1.18 %	$\varepsilon_0 =$ 0.34 %	$\varepsilon_0 =$ 0.16 %	$\varepsilon_0 =$ 0.09 %
	$\sigma =$ 250 MPa	$\sigma =$ 210 MPa	$\sigma =$ 180 MPa	$\sigma =$ 150 MPa	$\sigma =$ 135 MPa	$\sigma =$ 120 MPa	$\sigma =$ 100 MPa
<b>Creep Time [h]</b>	<b>Strain [mm]</b>						
250	0.75	0.185	0.155	0.117	0.011	0.02	0.021
500	0.95	0.270	0.19	0.140	0.0135	0.029	0.026
750	1.12	0.34	0.23	0.170	0.0195	0.035	0.03
1.000	1.30	0.39	0.27	0.190	0.021	0.04	0.0345
1.500	1.55	0.48	0.34	0.223	0.0255	0.046	0.04
2.000	1.80	0.57	0.405	0.250	0.0296	0.053	0.048
2.500	2.00	0.64	0.465	-	0.0331	0.059	0.051
3.000	2.20	0.71	0.512	0.310	0.037	0.063	0.054
3.500	2.41	-	-	-	0.04	-	-
4.000	2.64	0.875	0.60	0.350	0.0456	0.067	0.057
4.500	2.90	-	-	-	0.0466	-	-
5.000	3.19	0.97	0.68	0.402	0.0486	0.07	0.059
5.500	3.505	-	-	-	0.0506	-	-
6.000	3.885	1.12	0.75	0.470	0.054	0.074	0.06
7.000	aborted	1.265	0.82	0.520	0.0608	0.076	0.064
8.000		1.42	0.885	0.570	0.0656	0.078	0.066
9.000		1.58	0.942	0.607	0.0734	0.082	0.068
10.000		1.755	1.008	0.644	0.0806	0.086	0.071
11.000		1.92	1.062	-	0.0868	0.091	0.0744
12.000		2.075	1.127	0.731	0.092	0.0944	0.0756
13.000		2.25	1.172	-	0.1004	0.0964	0.076
14.000		2.435	1.218	0.817	0.1046	0.1016	0.078
15.000		2.617	1.272	0.860	0.1126	0.105	0.0796
16.000		2.813	1.322	0.893	0.118	0.108	0.0812
17.000		3.012	1.364	-	0.1214	0.1116	0.0824
18.000		3.174	1.417	0.959	0.1286	0.115	0.083
19.000		3.34	1.455	-	0.1368	0.121	-
20.000		3.51	1.51	1.024	0.1446	0.1244	0.0854
21.000		3.69	1.548	-	0.1514	0.126	-
22.000		3.885	1.597	-	0.1596	0.127	0.0866
23.000		4.09	1.641	-	0.1670	0.13	-
24.000		4.297	1.684	-	0.1752	0.1344	0.0876
25.000		4.492	1.724	1.143	0.1832	0.138	0.089
26.000		4.694	1.768	-	0.1914	0.14	0.09
27.000		4.884	1.808	-	0.1966	0.1448	-
28.000		5.07	1.853	-	0.20	0.1472	0.0916
29.000		5.277	1.892	-	0.2014	0.1522	-
30.000		5.426	1.934	1.282	0.204	0.1548	0.0934

31.000		5.675	1.983	-	0.2048	0.16	-
32.000		5.90	2.023	-	0.2066	0.164	0.096
33.000		6.13	2.071	-	0.208	0.1674	-
34.000		6.37	2.11	-	0.2132	0.1708	0.098
35.000		6.613	2.153	1.377	0.2174	0.174	0.10
36.000		6.852	2.193	-	0.2214	0.1786	0.1014
37.000		7.11	2.231	-	0.224	0.182	-
38.000		7.365	2.265	-	0.226	0.1848	0.1026
39.000		7.655	2.303	-	0.2306	0.1874	-
40.000		7.95	2.346	1.495	0.2346	0.1906	0.1042
41.000		8.123	2.395	-	0.239	0.1936	-
42.000		8.275	2.449	-	0.24	0.196	0.106
43.000		8.43	2.49	-	0.2434	0.1996	-
44.000		8.598	2.535	-	0.2476	0.2012	0.1074
45.000		8.759	2.557	1.585	0.2512	0.202	0.1084
46.000		8.947	2.583	-	0.2564	0.2032	0.1088
47.000		9.128	2.61	-	0.2604	0.2048	-
48.000		9.331	2.636	-	0.2646	0.2072	0.11
49.000		9.537	2.661	-	0.2704	0.2096	-
50.000		9.755	2.691	1.684	0.2744	0.2114	0.1114
51.000		9.977	2.715	-	0.2784	0.213	-
52.000		10.212	2.741	-	0.2824	0.215	0.1128
53.000		10.467	2.766	-	0.2866	0.2168	-
54.000		10.721	2.78	-	0.2896	0.2182	0.115
55.000		10.975	2.811	1.762	0.2914	0.2206	0.116
56.000		11.25	2.836	-	0.2928	0.222	0.1165
57.000		11.525	2.86	-	0.2972	0.2242	-
58.000		11.817	2.883	-	0.3018	0.226	0.1178
59.000		12.127	2.907	-	0.3066	0.2276	-
60.000		12.47	2.93	1.842	0.3120	0.2312	0.1206
61.000			2.953	-	0.3158	0.2336	-
62.000		after	2.973	-	0.3200	0.2356	0.1224
63.000		60000 h	2.998	-	0.3232	9.237	-
64.000		aborted	3.023	-	0.3270	0.2392	0.1236
65.000			3.047	1.919	0.3304	0.2412	0.1238
66.000			3.07	-	0.3340	0.2432	0.1242
67.000			3.09	-	0.3366	0.2448	-
68.000			3.113	-	0.3406	0.246	0.1254
69.000			3.133	-	0.3444	0.2474	-
70.000			3.155	1.992	0.3476	0.2500	0.1282

71.000			3.181	-	after	0.2516	-
72.000			3.208	-	70000 h	0.2536	0.1286
73.000			3.231	-		0.2548	-
74.000			3.255	-		0.2574	0.1292
75.000			3.282	2.060		0.2592	0.1302
76.000			3.301	-		0.2614	0.1306
77.000			3.326	-		0.2640	-
78.000			3.350	-		0.2664	0.1322
79.000			3.374	-		0.2696	-
80.000			3.398	2.139		0.2720	0.1354
81000			3.419	-		0.2736	
82000			3.443	-		0.2756	0.1364
83000			3.466	-		0.2774	-
84000			3.490	-		0.2800	0.1380
85000			3.511	2.212		0.2816	0.1388
			after 85000 h aborted	after 85000 h aborted		after 85000 h aborted	after 85000 h aborted

Table 11: Low-stress long-term creep test results for the AISI 316 L(N) stainless steel at 600 °C (Time-Strain values). Specimen dimensions have been M8 x 200 mm.

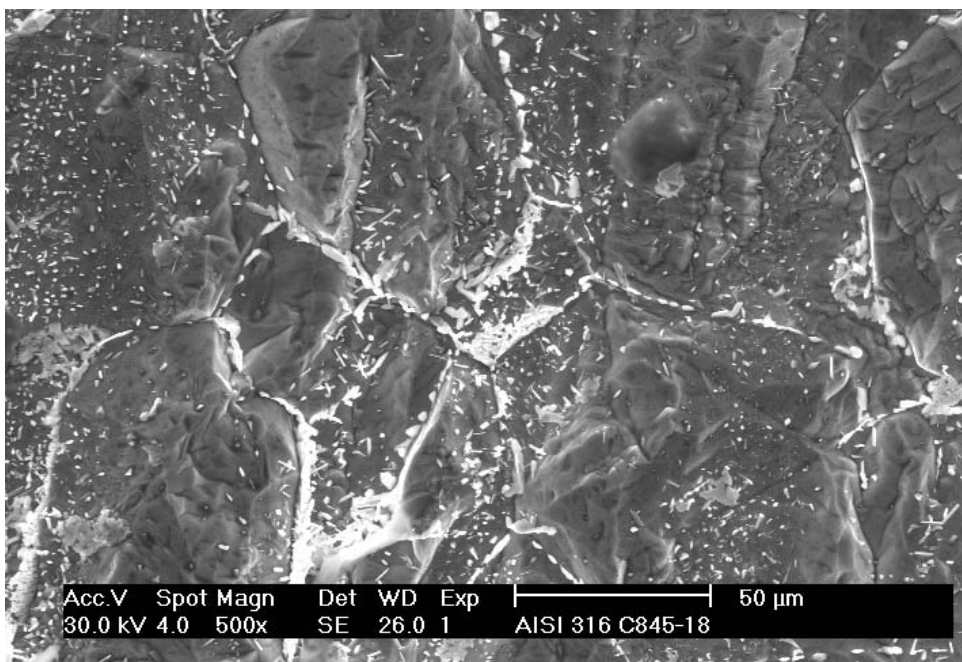
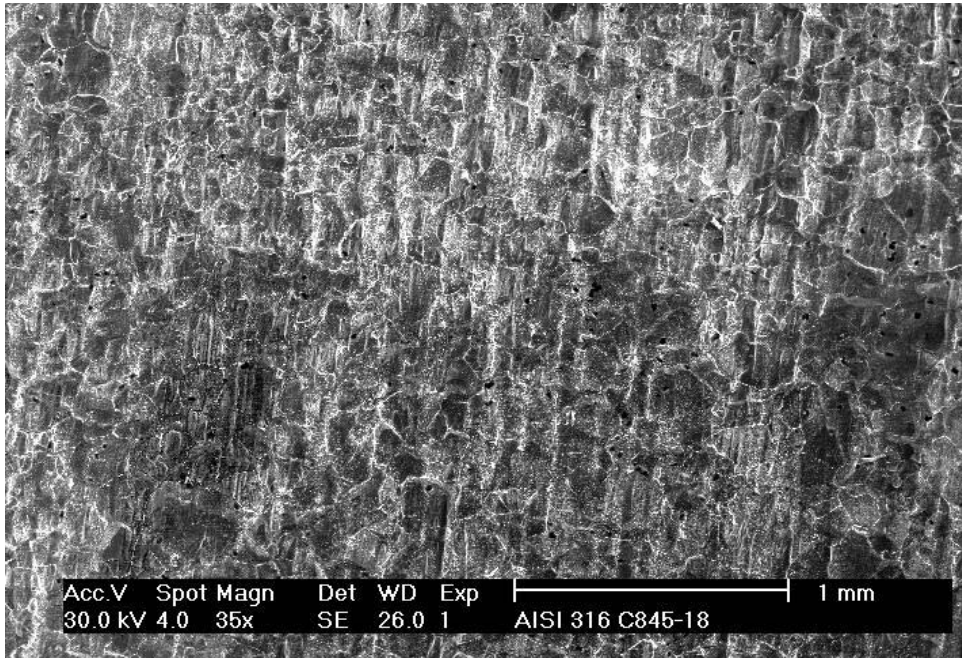
	$\varepsilon_0 =$ 3.03 %	$\varepsilon_0 =$ 0.32 %	$\varepsilon_0 =$ 0.07 %	$\varepsilon_0 =$ 0.06 %	$\varepsilon_0 =$ 0.055 %	$\varepsilon_0 =$ 0.04 %
	$\sigma =$ 170 MPa	$\sigma =$ 120 MPa	$\sigma =$ 100 MPa	$\sigma =$ 80 MPa	$\sigma =$ 70 MPa	$\sigma =$ 60 MPa
Creep Time [h]	Strain [mm]	Strain [mm]	Strain [mm]	Strain [mm]	Strain [mm]	Strain [mm]
250	0.68	0.09	0.06	0.036	0.024	0.028
500	1.115	0.15	0.087	0.053	0.036	0.044
750	1.51	0.20	0.108	0.065	0.043	0.049
1.000	1.88	0.253	0.128	0.077	0.046	0.055
1.500	2.63	0.34	0.16	0.088	0.051	0.06
2.000	3.38	0.447	0.183	0.098	0.056	0.063
2.500	4.045	0.537	0.205	0.108	0.057	0.066
3.000	4.54	0.618	0.223	0.117	0.058	0.068
3.500	5.125	-	-	-	-	-
4.000	5.632	0.753	0.252	0.138	0.064	0.07
4.500	6.145	-	-	-	-	-
5.000	6.68	0.852	0.282	0.145	0.066	0.071
5.500	7.235	-	-	-	-	-
6.000	7.86	0.95	0.302	0.148	0.069	0.073

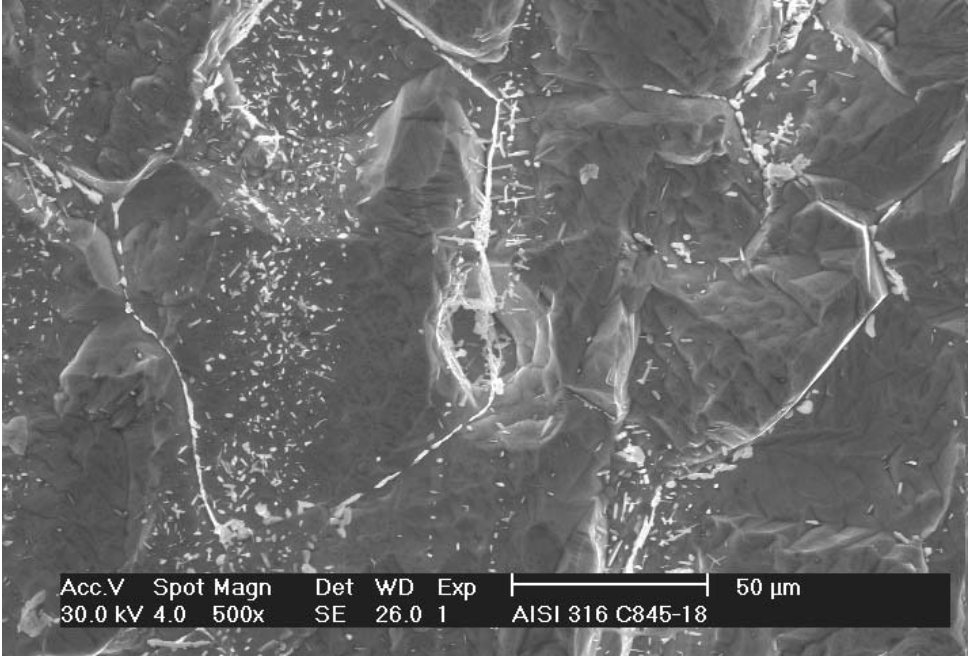
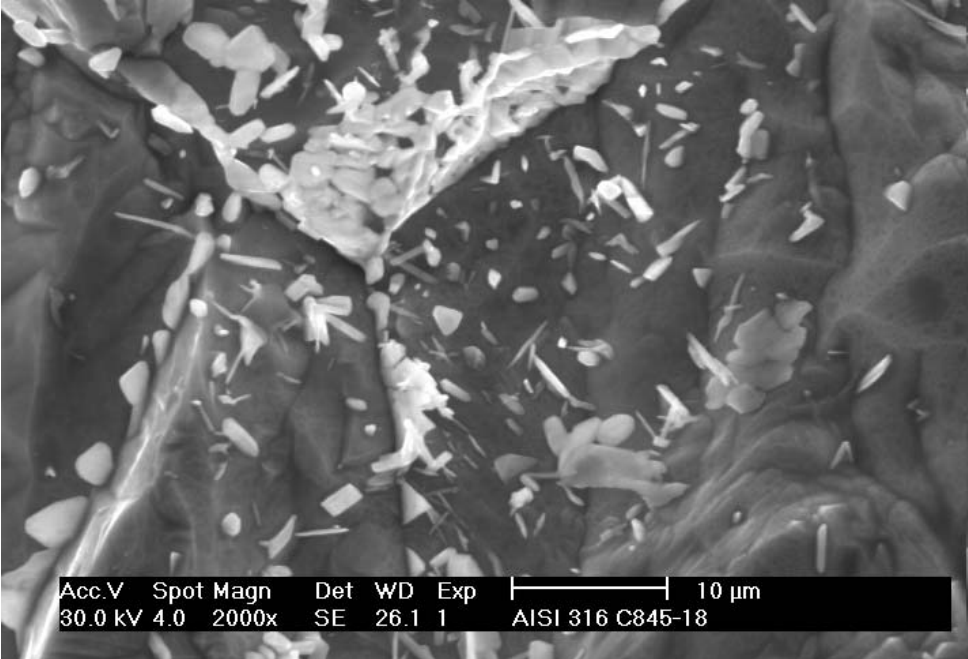
7.000	9.298	1.028	0.35	0.152	0.072	0.074
8.000	aborted after 7500 h	1.095	0.38	0.155	0.074	0.076
9.000		1.153	0.4	0.16	0.075	0.0775
10.000		1.21	0.416	0.164	0.0768	0.08
11.000		1.257	0.43	0.167	0.0778	0.083
12.000		1.3	0.443	0.172	0.0788	0.0852
13.000		1.338	0.457	0.173		
14.000		1.372	0.481	0.1746	0.0808	0.086
15.000		1.412	0.518	0.176	0.082	0.087
16.000		1.447	0.53	0.1775	0.0828	0.088
17.000		1.487	0.544	0.18	-	-
18.000		1.53	0.553	0.182	0.0848	0.0898
19.000		1.578	0.568	0.1856	-	-
20.000		1.628	0.576	0.1872	0.0866	0.091
21.000			1.683	0.584	0.1888	-
22.000	1.743		0.593	0.1896	0.0886	0.0928
23.000	1.803		0.604	0.1914	-	-
24.000	1.862		0.612	-	0.0906	0.0946
25.000	1.922		0.623	0.1956	0.0916	0.0952
26.000	1.988		0.633	0.1984	0.0926	0.0954
27.000	2.063		0.642	0.2008	-	-
28.000	2.146		0.652	0.2026	0.0948	0.0964
29.000	2.236		0.662	0.2066	-	-
30.000	2.35		0.67	0.2084	0.097	0.0984
31.000		2.46	0.068	0.2124	-	-
32.000		2.55	0.688	0.2154	0.0992	0.10
33.000		2.674	0.694	0.2176	-	-
34.000		2.808	0.706	0.2196	0.1014	0.1014
35.000		2.954	0.712	0.2206	0.1026	0.1018
36.000		3.11	0.72	0.2234	0.1042	0.103
37.000		3.277	0.732	0.2276	-	-
38.000		3.458	0.743	0.23	0.1074	0.104
39.000		3.645	0.755	0.2336	-	-
40.000		3.845	0.767	0.2366	0.1106	0.1048
41.000		4.06	0.78	0.24	-	-
42.000			0.792	0.243	0.1138	0.106
43.000			0.802	0.2454	-	-
44.000			0.81	0.2474	0.117	0.107
45.000		aborted after 41015 h	0.818	0.2486	0.1186	0.1076
46.000			0.828	0.2498	0.1202	0.1084
47.000			0.838	0.2518	-	-
48.000			0.849	0.254	0.1232	0.109
49.000			0.863	0.2566	-	-
50.000			0.874	0.259	0.1262	0.1108

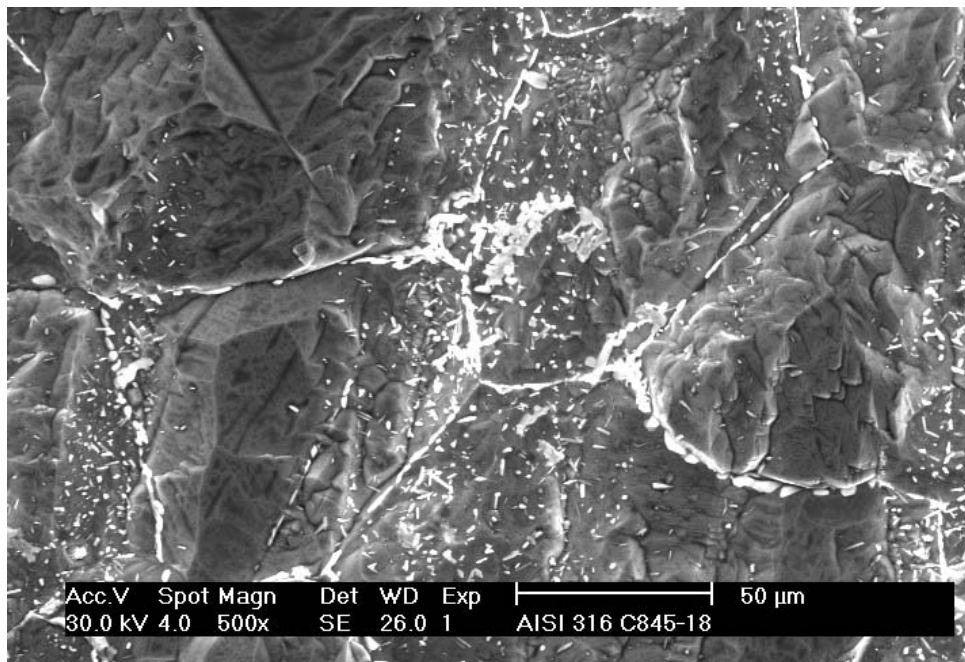
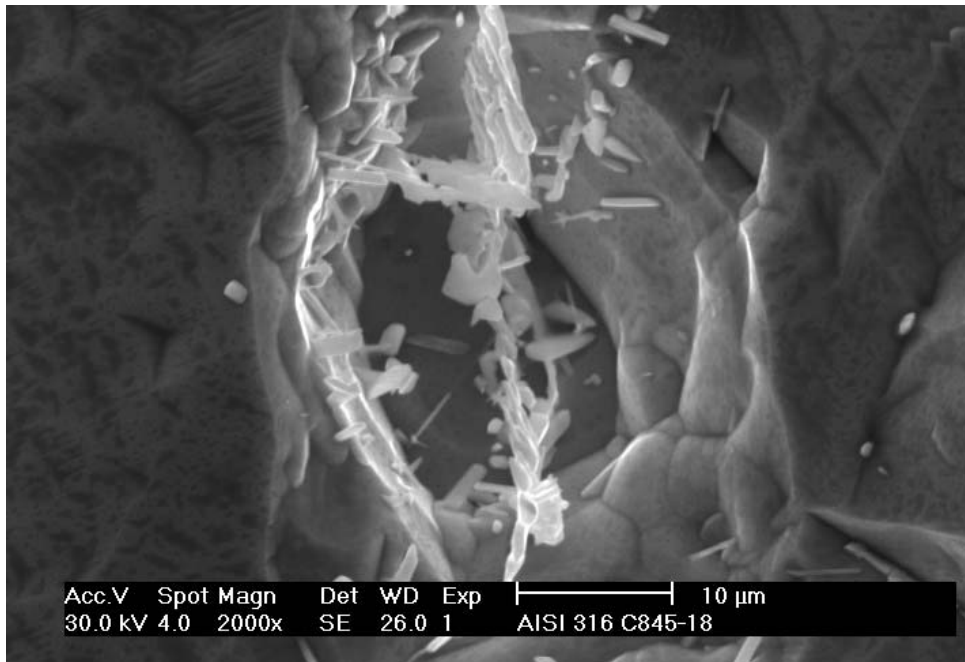
51.000			0.886	0.26	-	-
52.000			0.897	0.262	0.1292	0.1128
53.000			0.91	0.265	-	-
54.000			0.92	0.2668	0.1332	0.1148
55.000			0.932	0.2684	0.1356	0.1164
56.000			0.943	0.2704	0.1372	0.1172
57.000			0.954	0.2724	-	-
58.000			0.97	0.2736	0.145	0.1188
59.000			0.983	0.2746	-	-
60.000			0.994	0.277	0.148	0.1204
61.000			1.006	0.28	-	-
62.000			1.016	0.2826	0.1512	0.1228
63.000			1.028	0.2844	-	-
64.000			1.041	0.2874	0.1566	0.1254
65.000			1.054	0.29	0.1596	0.1258
66.000			1.066	0.2912	0.1632	0.1266
67.000			1.082	0.2936	-	-
68.000			1.096	0.2972	0.1674	0.1284
69.000			1.109	0.2996	-	-
70.000			1.123	0.3034	0.1712	0.1306
71.000			1.138	0.3060	-	-
72.000			1.151	0.3080	0.1754	0.1324
73.000			1.163	0.3108	-	-
74.000			1.177	0.3134	0.1814	0.1346
75.000			1.191	0.3166	0.1848	0.1352
76.000			1.205	0.3180	0.1872	0.1360
77.000			1.218	0.3208	-	-
78.000			1.232	0.3246	0.1922	0.1376
79.000			1.245	0.3276	-	-
80.000			1.257	0.3306	0.1934	0.1392
81000			1.273	0.3326	-	-
82000			1.290	0.3348	0.1976	0.1404
83000			1.304	0.3386	-	-
84000			1.318	0.3404	0.2046	0.1418
85000			1.333	0.3428	0.2066	0.1432
			aborted after 85000 h	aborted after 85000 h	aborted after 85000 h	aborted after 85000 h

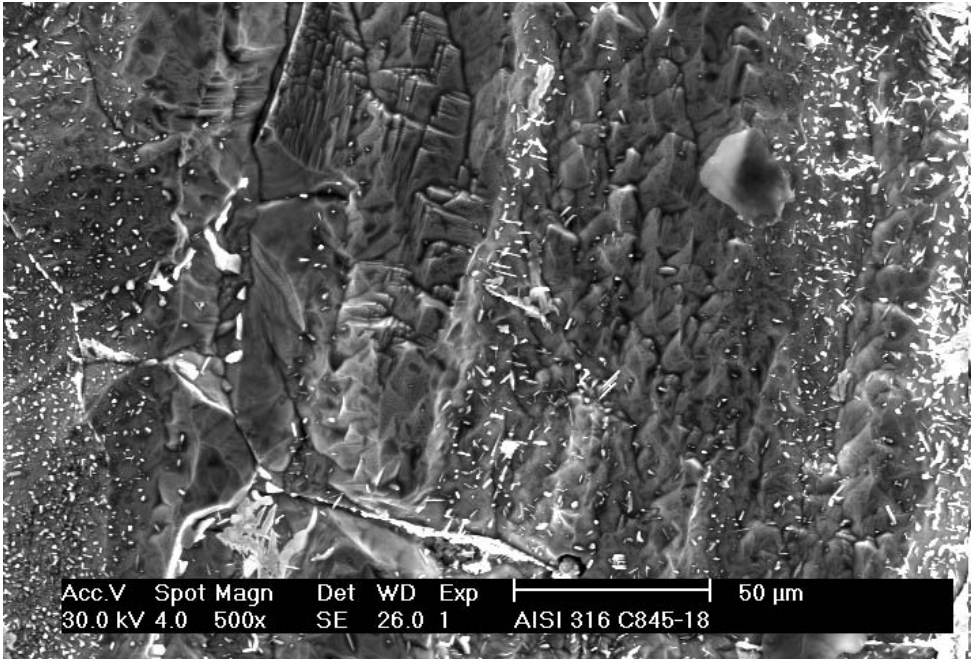
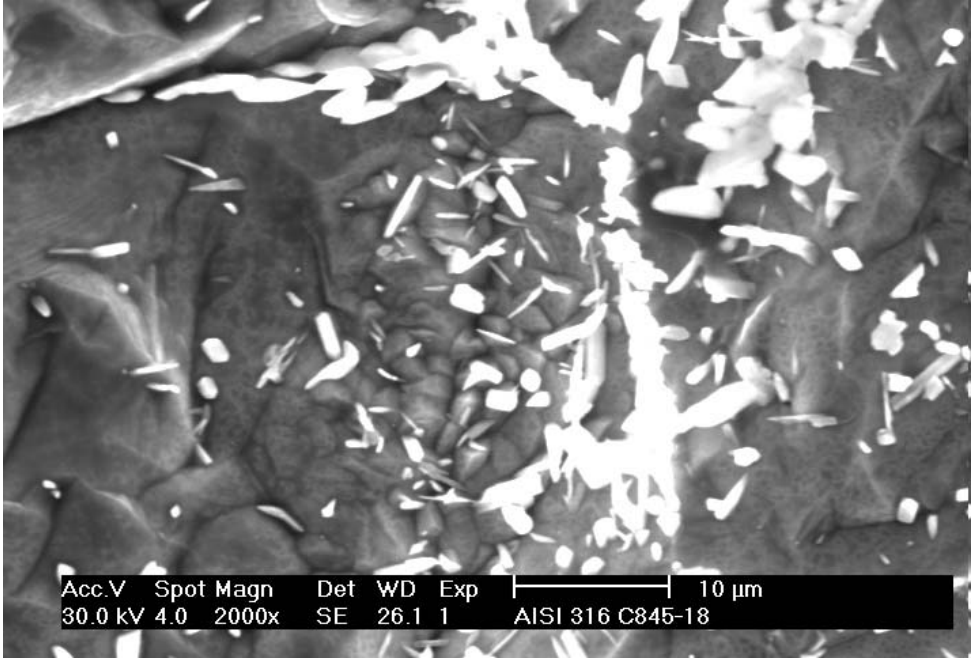
## 7.3 Metallographic Examinations

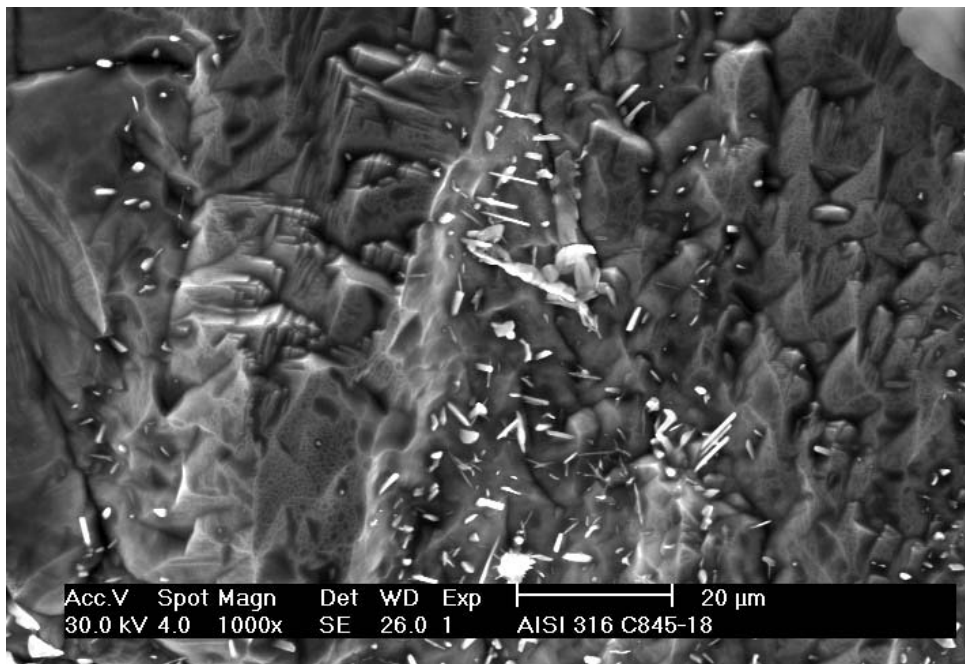
### 7.3.1 Test No. ZSV1921: 750 °C, 2650 h



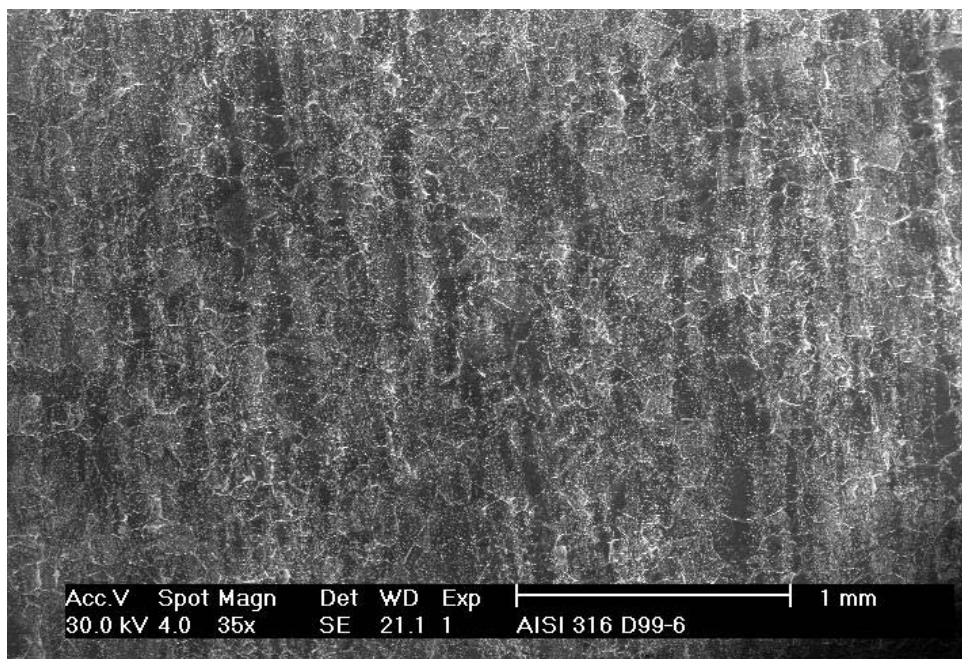


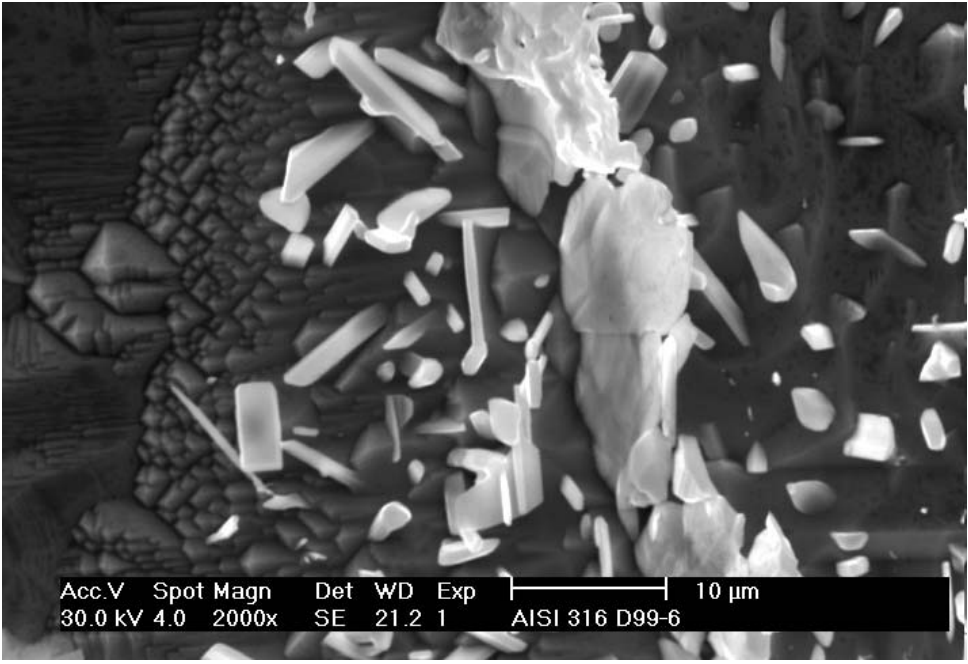
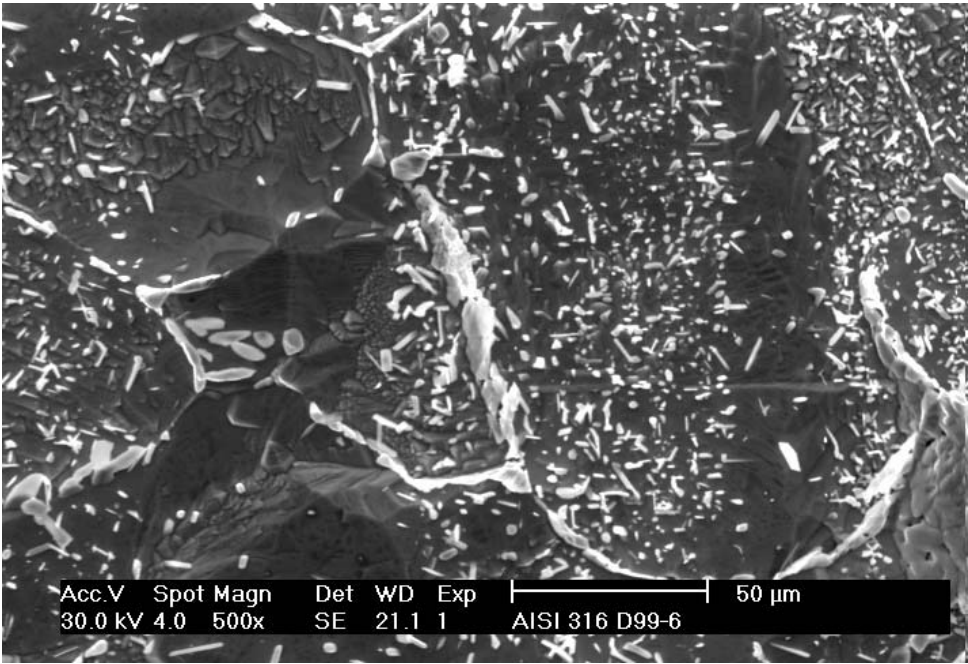


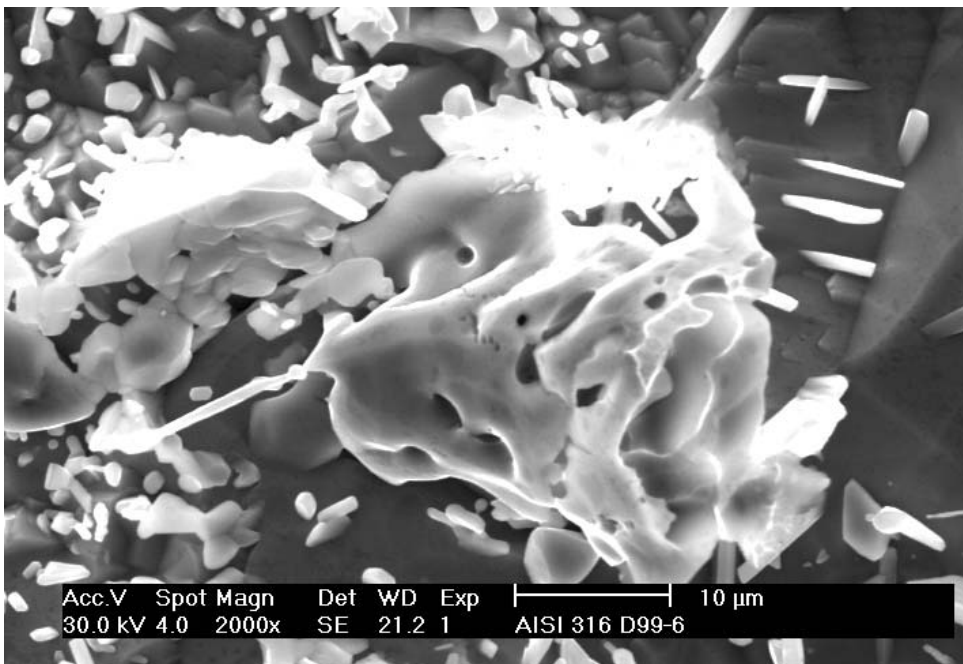
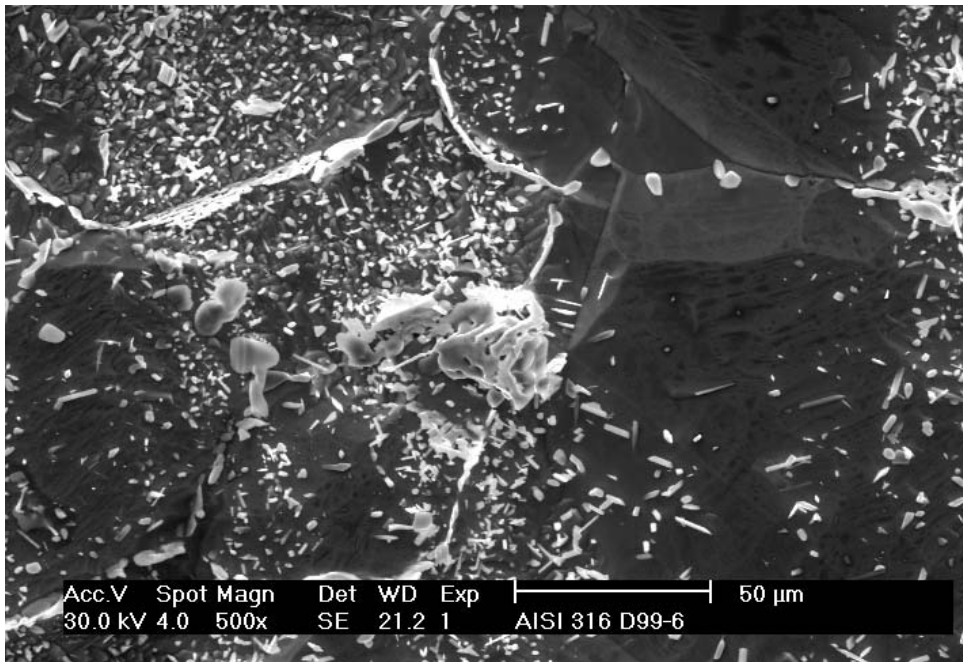


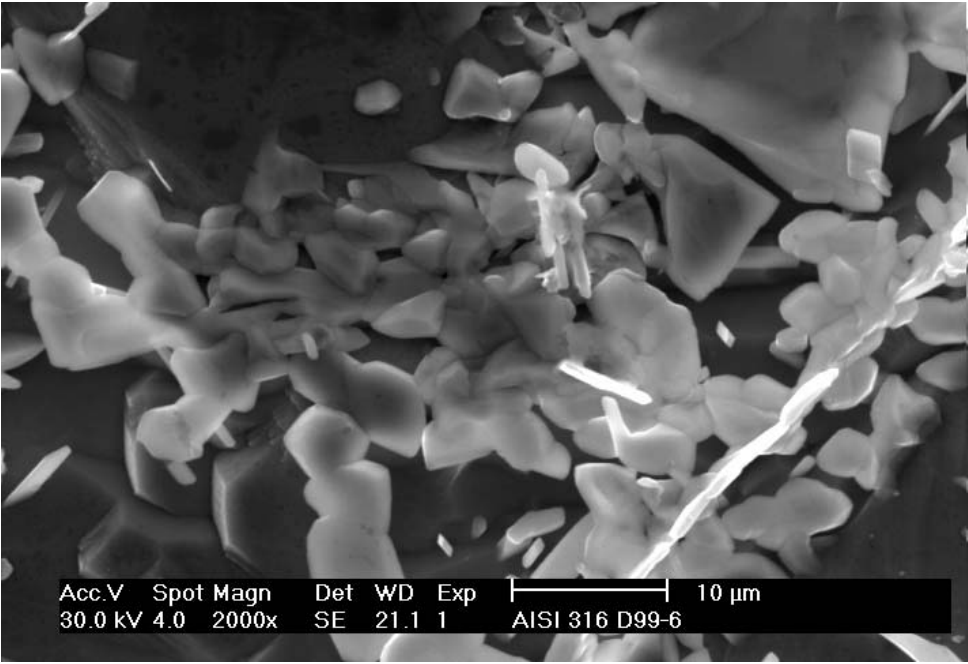
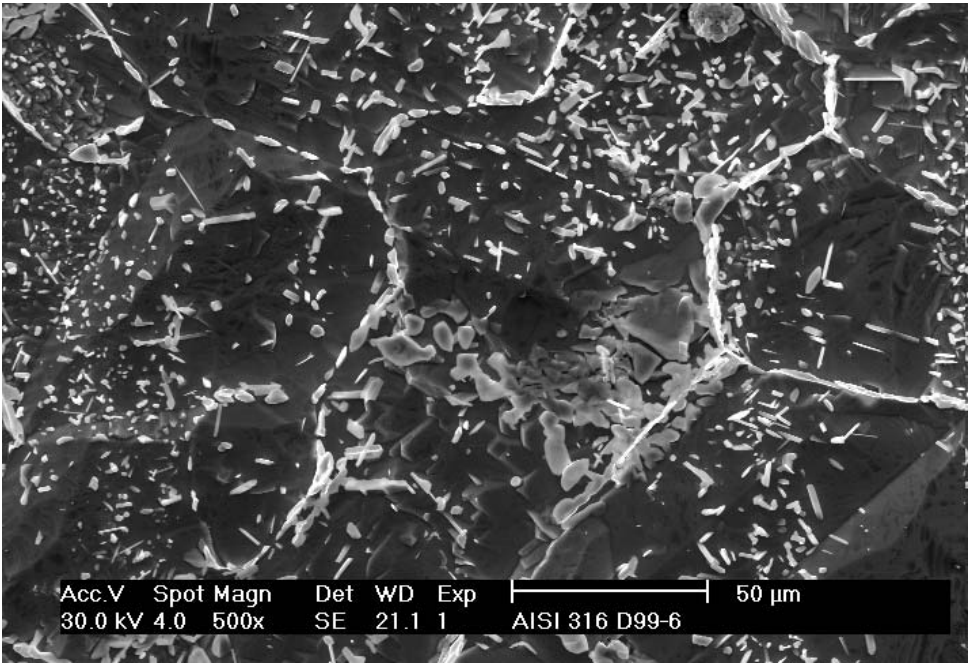


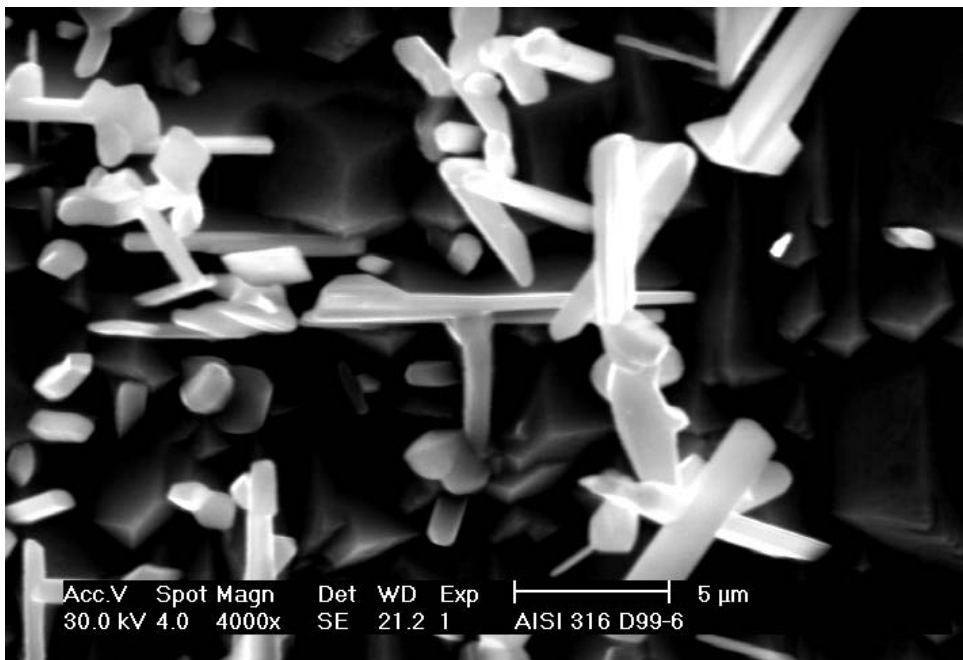
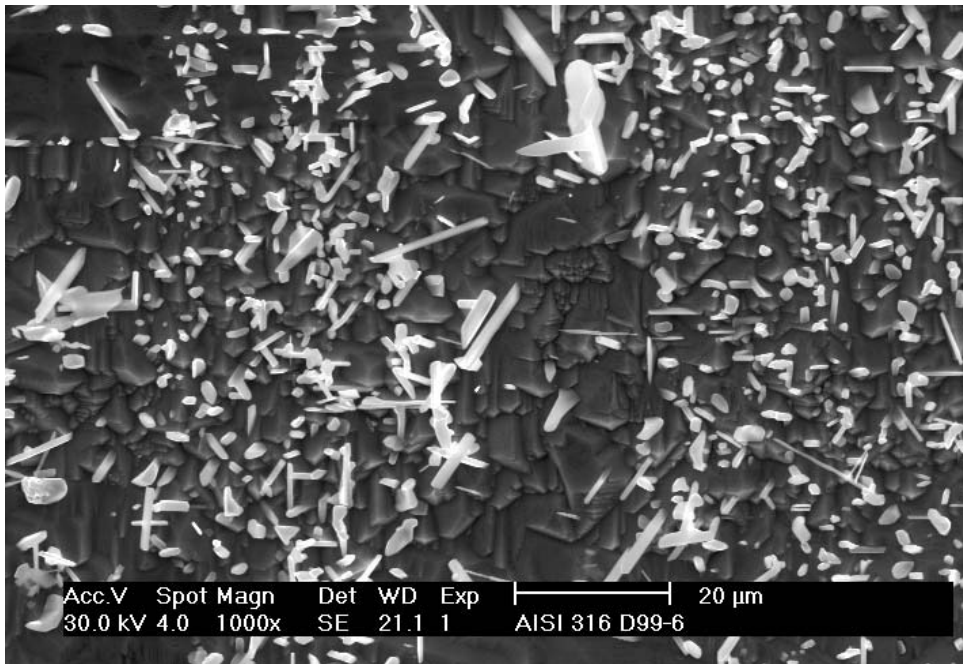
7.3.2 Test No. ZSV1913: 750 °C, 15692 h



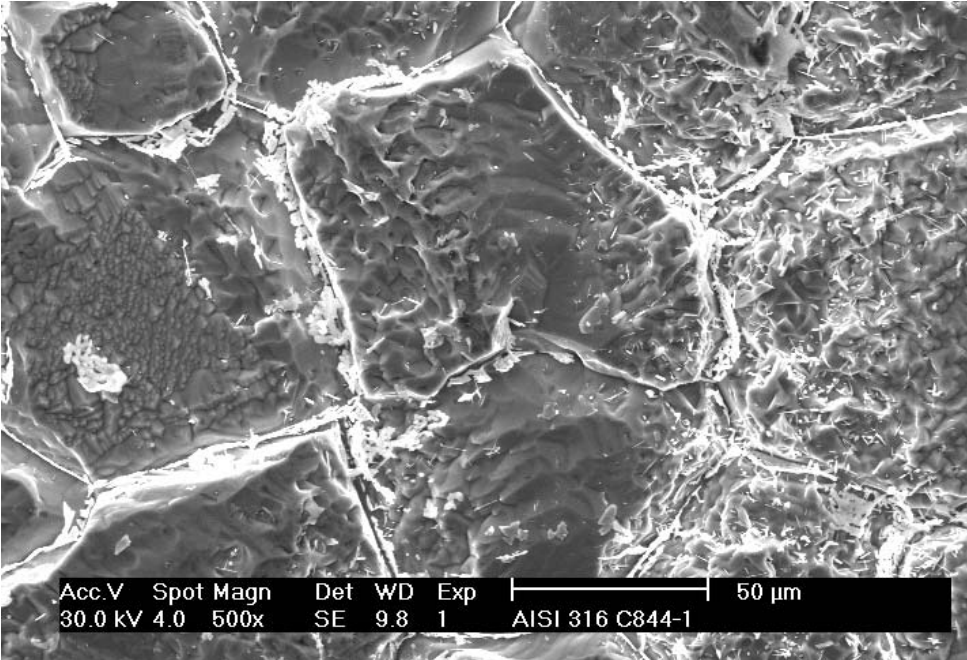
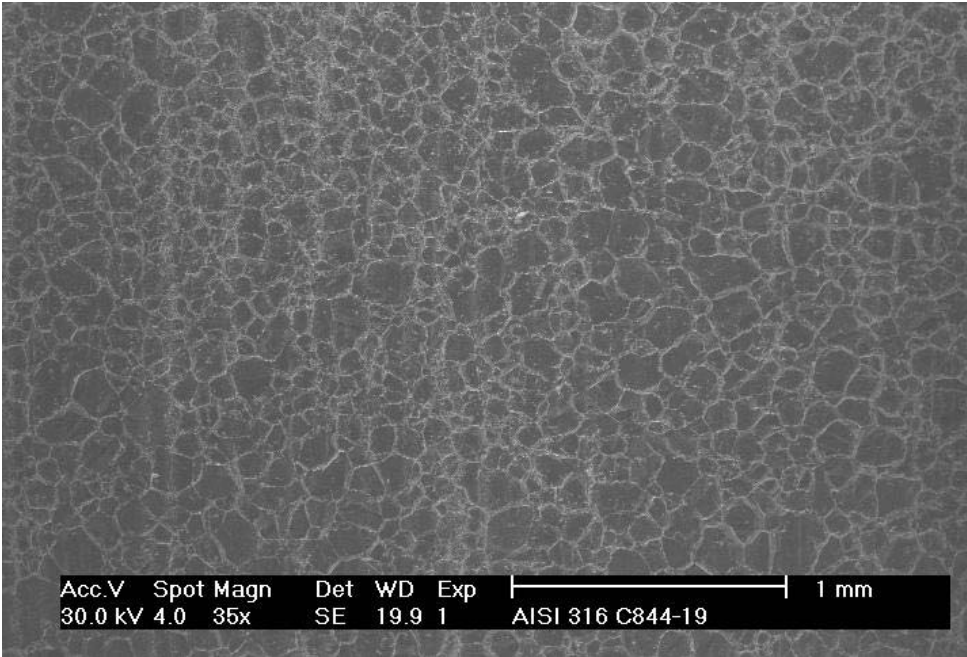


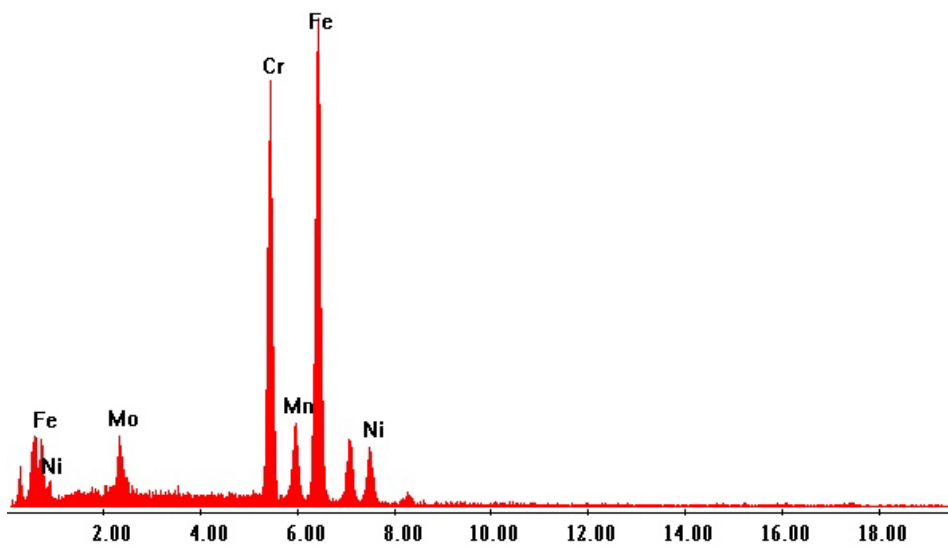
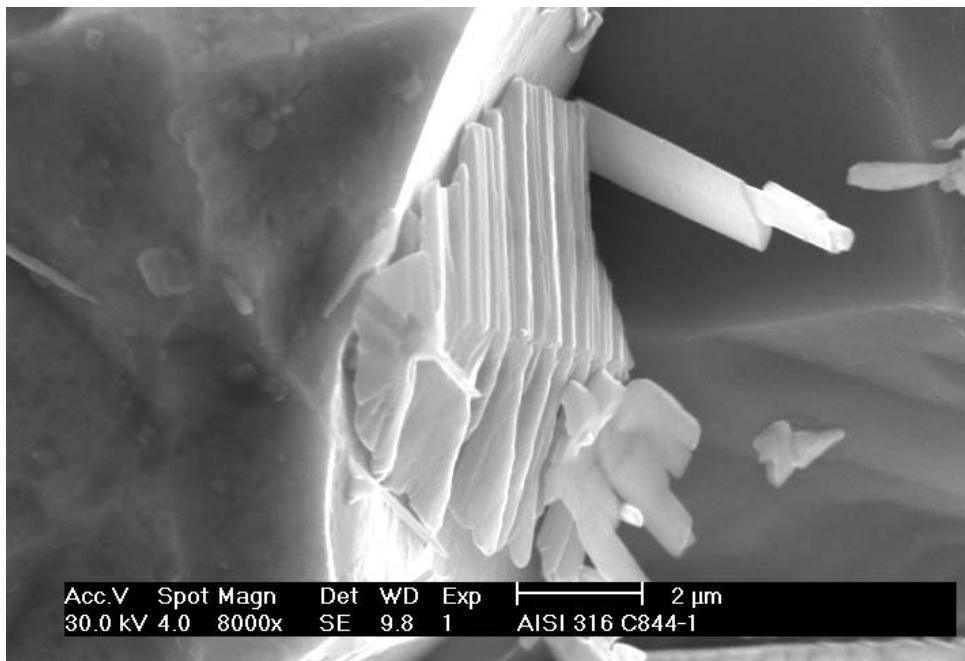


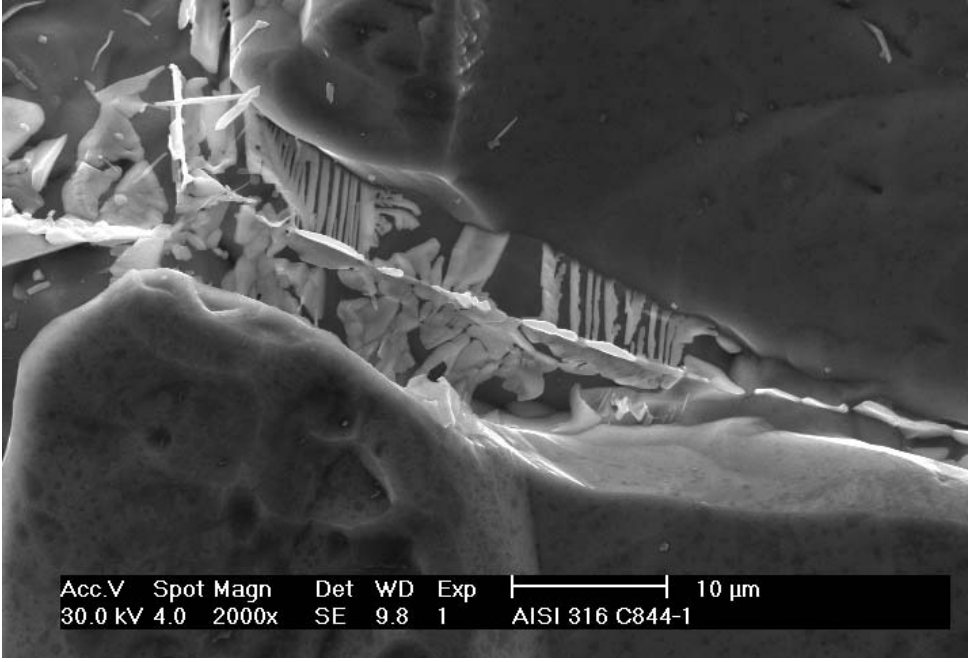
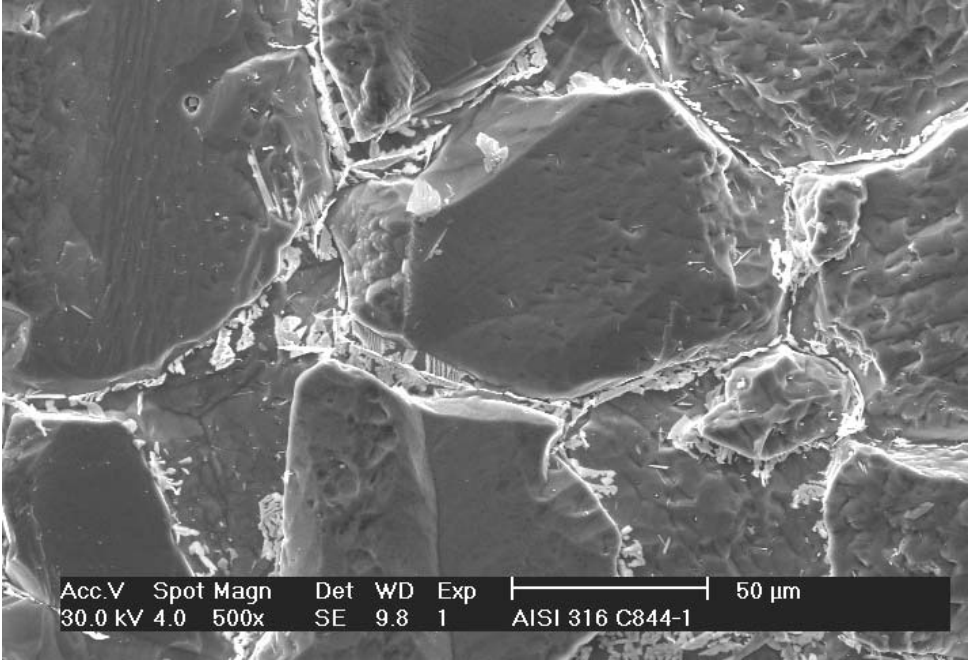


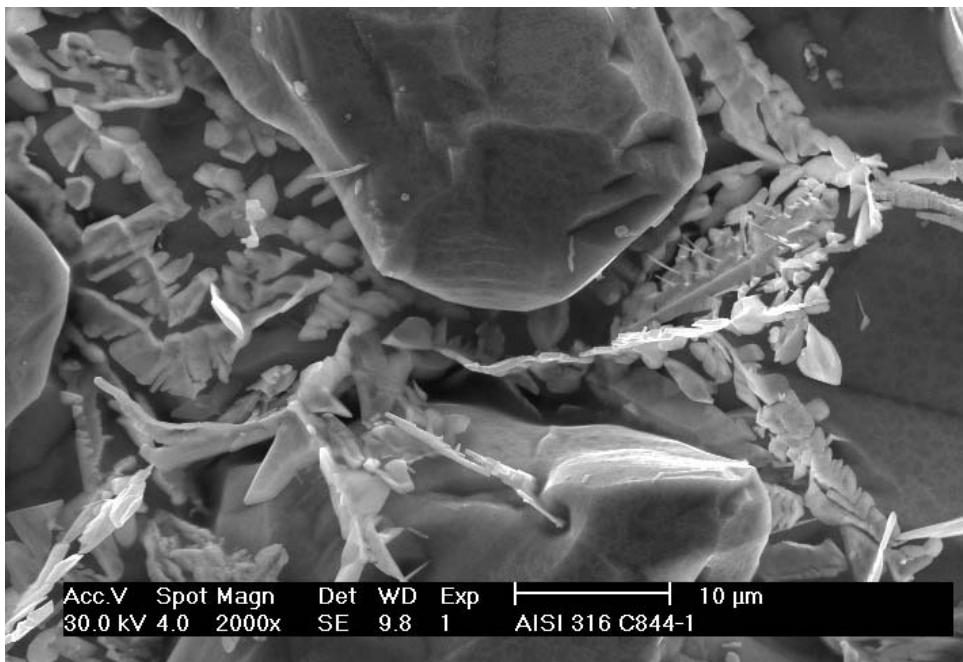
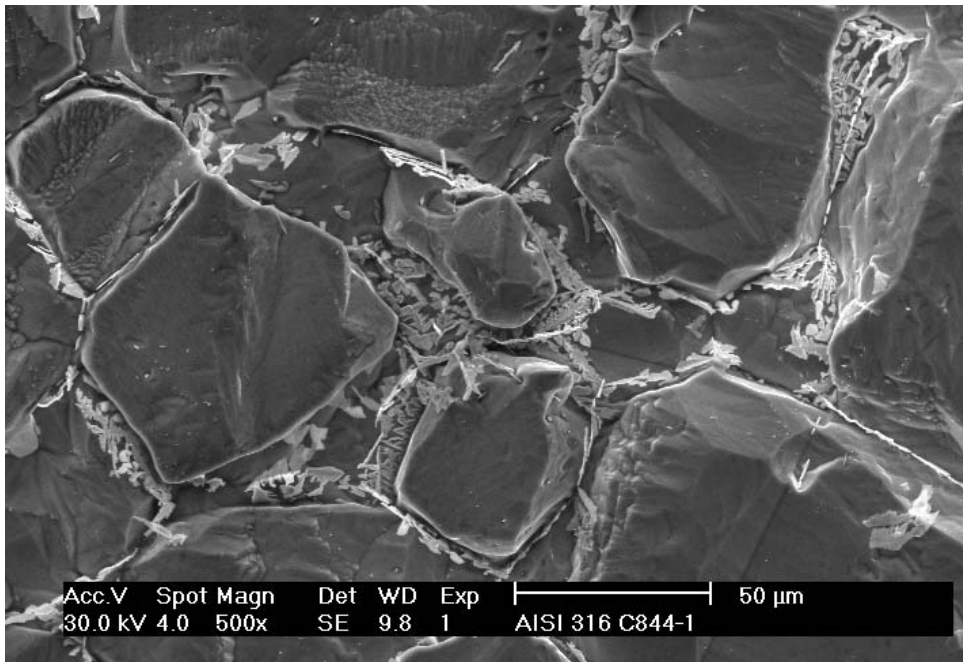


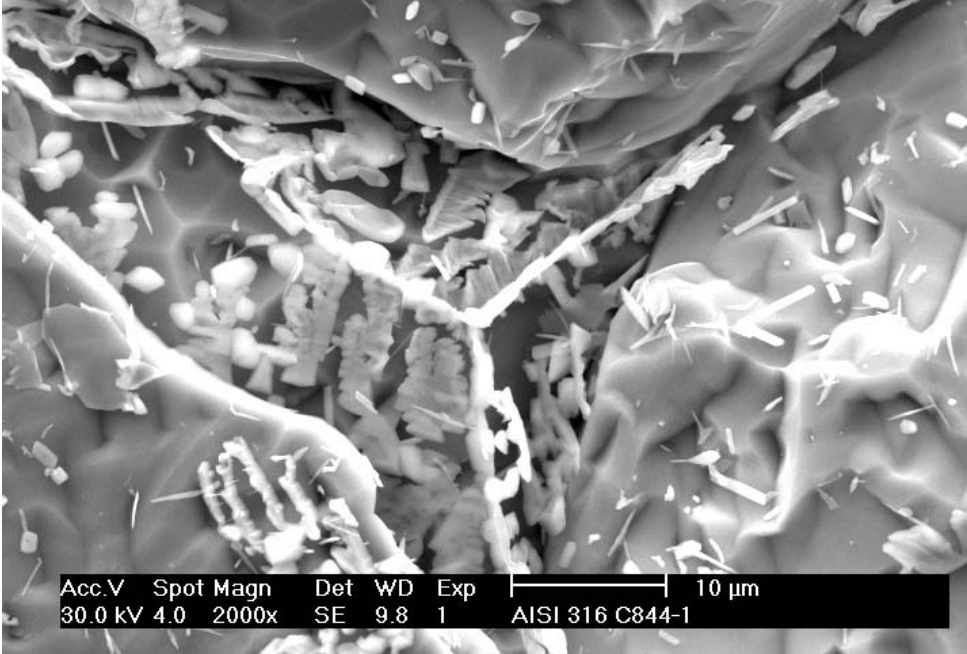
7.3.3 AISI 316 L(N) KSW heat (similar to present CRM heat): 750 °C, 1404 h

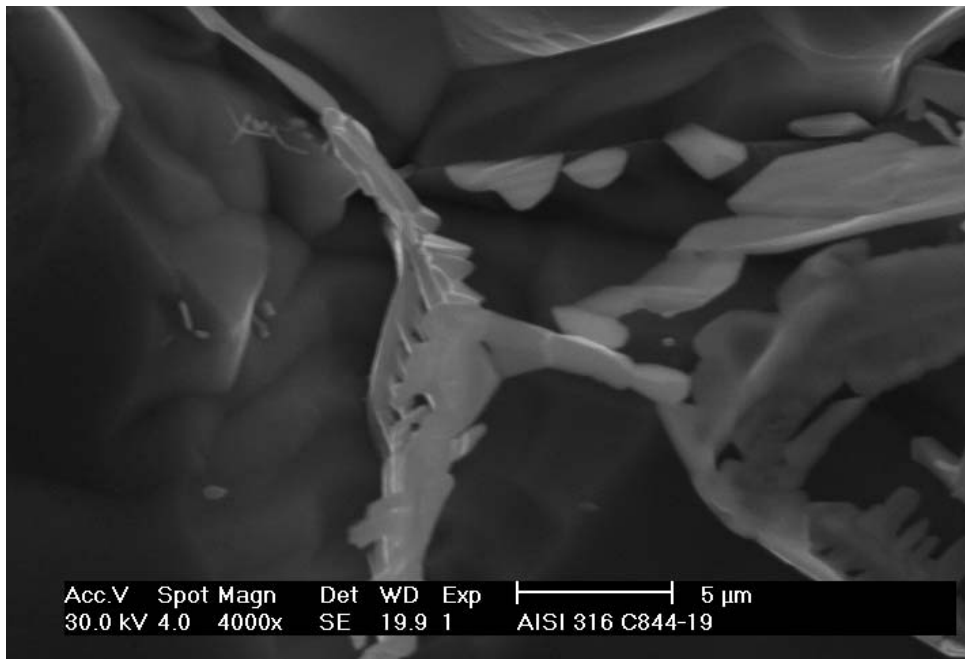
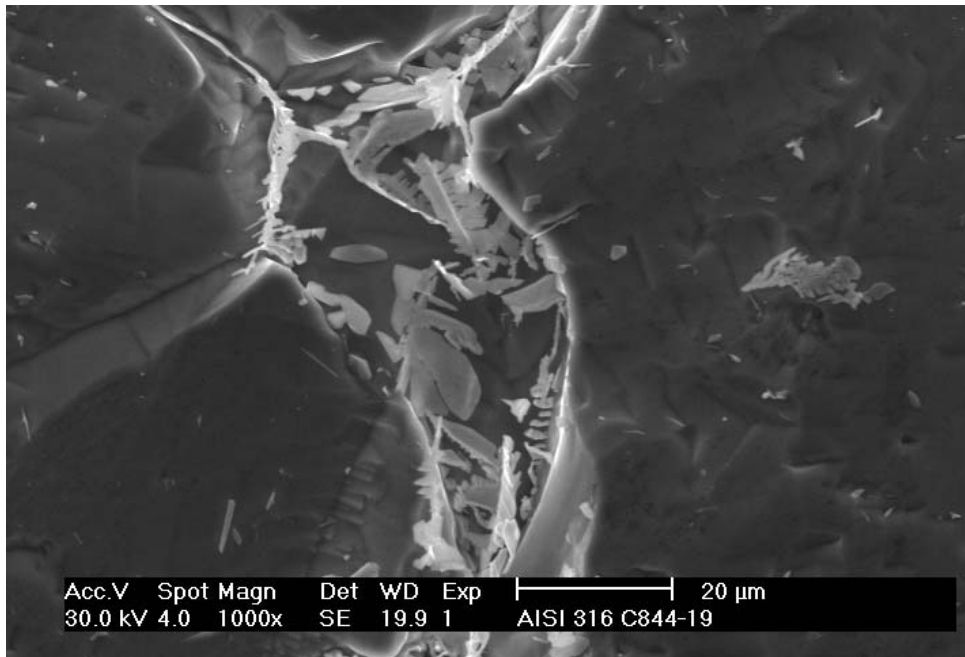












7.3.4 AISI 316 L(N) KSW heat (similar to present CRM heat): 750 °C, 13824 h

